Fabrication of functional and structured particles by inkjet printing of emulsions

WANG, YILIN

Fabrication of functional and structured particles by inkjet printing of emulsions

Yilin Wang

Supervisor: Colin Bain

Department of Chemistry

April 2021

Abstract

Emulsion solvent evaporation is a well-established method for generating microparticles from solutions of polymers in volatile organic solvents dispersed in an aqueous medium. Previous work has shown that this approach can also be used to deposit particles by inkjet printing where the particles are formed during the drying of a liquid ink on a substrate. The particle size distribution, however, was very broad. Here I demonstrate that inkjet printing of oil-in-water emulsions produced by microfluidics can generate micron-sized particles with a narrow size distribution (coefficient of variation <6%) and that these particles can self-assemble into ordered arrays with hexagonal packing. The conditions under which drops can be printed with a minimum of break up and coalescence of the oil droplets in the emulsion are explored. Factors affecting the size of the particles and the morphology of the deposit are described. This study uses polystyrene in dichloromethane as a model system, but the approach can be generalized to the production of structured and functional particles.

Besides, I explore the mechanism of formation of core-shell microcapsules by emulsion solvent evaporation, where the emulsion contains a shell-forming polymer and a core-forming poor solvent dispersed in a good solvent as the oil phase. Evaporation of the good solvent induces an internal phase separation within the oil droplets of the emulsion, triggering the formation of microcapsules. First I study the wetting conditions necessary to induce the internal phase separation within emulsions. Then I construct a ternary phase diagram to predict the formation process, either polymer-rich phase or poor solvent-rich phase can phase separate from the bulk solution, depending on the ratio of polymer to poor solvent. Then the physical parameters affecting the phase separation and hence the final morphology are explored. Finally, the conditions are optimised to minimise the effect of pseudo partial wetting to obtain a uniform morphology of core-shell microcapsules.

Last, I demonstrate the strategy of emulsion solvent evaporation can be used in the generation of hierarchical Murray materials with multi-scale interconnected pores by inkjet printing nanoparticle-containing emulsions, where silica nanoparticles are pre-dispersed in the discrete phase. A continuous monolayer of well-defined, hexagonally packed silica microspheres with hierarchical macro-meso porous structure is obtained. The porosity of the Murray material can be readily tuned by varying the size of the primary silica nanoparticles. Factors affecting the morphology of the deposit pattern have been explored. This study uses solid silica nanoparticles in discrete phase as a model system to produce

macro-meso porous material with two-scale interconnected pores, but the strategy can be generalized to the porous nanoparticles for the production of more structured Murray material with multi-scale pores, like macro-meso-micro hierarchical porous materials.

Acknowledgements

First of all, many thanks to my supervisor, Prof. Colin Bain, for his support and encouragement, and for providing discussions and feedback I received during these years in Chemistry. Thank you also to all lab members in Bain's group, especially to Dr Lisong Yang, Renhua Deng, for providing support and useful suggestions in experiments when required. Also thanks Durham University and the China Scholarship Council for studentship funding, and offering me this exciting opportunity to pursue my PhD. Moreover, particularly thanks to SEM staff Dr Diana Talia Alvarez Ruiz and Leon Bowen, who offered great help of operating SEM during lockdown. Finally, special thanks to my dear family and friends, as without you I simply could not have done this.

Thank you again from bottom of my heart.

Publications List

The following publications were made during the course of this thesis:

Wang , Y., Deng, R., Yang, L. and Bain, C.D., 2019. Fabrication of monolayers of uniform polymeric particles by inkjet printing of monodisperse emulsions produced by microfluidics. Lab on a Chip, 19(18), pp.3077-3085.

Deng, R., **Wang , Y**., Yang, L. and Bain, C.D., 2019. In situ fabrication of polymeric microcapsules by ink-jet printing of emulsions. ACS Applied Materials & Interfaces, 11(43), pp.40652-40661.

Declaration

The author declares no competing financial interest. This work used equipment funded by EPSRC under Grant EP/N025245/1. The software for particle sizing was written by Jing Shi. YW thanks the China Scholarship Council and Durham University for funding.

Copyright notice

Contents

Symbols list

In order of appearance:

d_p	particle size, μm
δ	thickness of the shell, μm
R	typical inkjet printed droplet radius, μm
r	oil droplet radius, μm
d_i	measured particle diameter, μm
d^*	mean diameter, μm
a_0	characteristic size of the finger at the junction, μm
h_0	initial height of the droplet, μm
a	gyration radius, mm
V_{oil}	oil droplet volume, ml
V_p	particle volume, ml
ρ_p	polymer density, g ml^{-1}
c_p	polymer concentration, % w/v
λ	spreading coefficient
σ_{BS}	interfacial tension between medium S and liquid B, $mN\ m^{-1}$
σ_{AS}	interfacial tension between medium S and liquid A, $mN\ m^{-1}$
χ_{S-P}	polymer-solvent interaction parameter
δ_S	solubility parameters of the solvent, $MPa^{1/2}$
δ_P	solubility parameters of the polymer, $MPa^{1/2}$
R	ideal gas constant, J K mol^{-1}
T	temperature, K

α	shrinkage factor
Ca	Capillary number
μ	viscosity of liquid phase, Pa s
G	strain rate, s^{-1}
Bo	Bond number
ρ	fluid density, kg m^{-3}
g	gravitational constant, m s^{-2}
γ_{SG}	interfacial energy between solid phase and gas phase, $\mathrm{mN\ m}^{-1}$
γ_{LG}	interfacial energy between liquid phase and gas phase, $\mathrm{mN\ m}^{-1}$
γ_{SL}	interfacial energy between solid phase and liquid phase, $\mathrm{mN\ m}^{-1}$
θ_A	advancing contact angle
θ_R	receding contact angle
θ_c	equilibrium contact angle
v_o	oil phase flow rate, $\mu\mathrm{m\ s}^{-1}$
v_a	aqueous phase flow rate, $\mu\mathrm{m\ s}^{-1}$
c	vapour concentration, mol L^{-1}
D	vapour diffusivity, $\mathrm{m}^2\mathrm{s}^{-1}$
$J(r,\theta)$	evaporation flux along the air-liquid interface, $\mathrm{kg\ m}^{-2}\ \mathrm{s}^{-1}$
$J_0(\theta)$	evaporation flux at the droplet centre, $\mathrm{kg\ m}^{-2}\ \mathrm{s}^{-1}$
CV	coefficient of variation
n	number of particles analysed
γ	shear rate, s^{-1}
v	sedimentation rate, m s^{-1}

J_{ave}	average evaporative flux, $\mathrm{kg\ m^{-2}\ s^{-1}}$
$c_s(v)$	concentration of DCM vapour, mol $\mathrm{L^{-1}}$
$c_s(l)$	concentration of DCM in the liquid phase at the surface, mol $\mathrm{L^{-1}}$
$c_0(l)$	saturation concentrations of DCM in the liquid phases, mol $\mathrm{L^{-1}}$
$c_0(v)$	saturation concentrations of DCM in the vapour phase, mol $\mathrm{L^{-1}}$
Pe	Peclet number
E	evaporation rate, $\mathrm{kg\ m^{-2}\ s^{-1}}$
K	Boltzmann constant, $\mathrm{J\ K^{-1}}$
A_H	Hamaker constant
F(d)	free energy per unit area of the water/core/shell structure, J m^{-2}
p_v	Saturated DCM vapour pressure, kPa
$p_{v(water)}$	water vapour pressure, kPa

Abbreviations

o/w	oil-in-water emulsion
w/o	water-in-oil emulsion
o/w/o	oil-in-water-in-oil emulsion
w/o/w	water-in-oil-in-water emulsion
CMC	critical micelle concentration
CV	coefficient of variation
PLGA	poly(dl-lactide-co-glycolide)
DCM	dichloromethane
PVA	poly(vinyl alcohol)
RFP	rifampicin
PMMA	poly(methylmethacrylate)
HD	hexadecane
SDS	sodium dodecyl sulfate
PVP	poly(2-vinylpyridine)
PVPK	poly(vinylphenyl ketone)
PS	polystyrene
PVP-co-PS	poly(2-vinylpyridine-costyrene) copolymers
P4VP	Poly(4-vinylpyridine)
IBA	isobornyl acrylate
PAA	poly(acrylic acid)
CIJ	continuous inkjet
DOD	drop-on-demand

TCL	three-phase contact line
CR	a constant droplet radius stage
CA	a constant contact angle stage
SEM	scanning electron microscopy
AFM	Atomic force microscope
EDX	Energy dispersive X-Ray analysis
TEM	Transmission electron microscopy
FIB	Focused ion beam
BE	backscattered electrons
SE	secondary electrons
WDS	wavelength dispersive spectrometer
NMR	nuclear magnetic resonance spectroscopy
EISA	evaporation-induced self-assembly
CDMOS	chloro(dimethyl)octylsilane
HMDS	hexamethyldisilazane
RH	relative humidities
PLLA	poly(L-lactide) 2-hydroxyethylmethacrylate-terminated
TCNQ	7,7,8,8–tetracyanoquinodimethane
EtOAc	ethyl acetate

1 Introduction

1.1 Motivation

My PhD is a part of a joint project in Colin Bain's group on Evaporative Drying of Droplets and the Formation of Microstructured and Functional Particles and Films. This project aims to produce microstructured and functional particles and films by the use of inkjet printing and spray drying. My work is related to the goals of the larger project but is independent of the work already planned. Over the past few decades, there has been growing interest in creating structured particles in microfluidic devices, where a flow-focussing junction is used to create droplets of emulsions, in which the polymer solutions are encapsulated in a non-polar continuous phase. Evaporation of the emulsion can lead to a variety of outcomes including phase separation of immiscible polymers, formation of Janus particles and creation of core-shell particles. Seminal work in this area has been conducted by Jintao Zhu at HUST and Zhenzhong Yang at ICCAS. The reverse situation of non-polar droplets in a continuous polar phase can also be engineered. Bain's group has recently shown that long-chain polymers can be inkjet-printed successfully if they are confined within small emulsion droplets where the interfacial tension of the droplets prevents the polymer chains from being stretched and the fluid from behaving elastically.

My work is built on these ideas to print more complex emulsions where the controlled evaporation of the solvents in the printed droplet leads to the formation of microstructures analogous to those created in microfluidic devices. My initial objective is to fabricate a uniform layer of core-shell particles by inkjet deposition on a clean or functionalised surface. Possible applications include sprays for controlled release of mosquito repellents or anti-microbial agents (e.g. for hard surfaces in hospitals). Subsequent challenges will be to create more complex 'smart' surface that trigger a response under changes in pH or temperature.

1.2 Emulsion solvent evaporation

Emulsion solvent evaporation is a well-established method for manufacturing polymeric microparticles. In this method, polymers and other non-volatile components are dissolved in the discrete phase of an oil-in-water emulsion. The non-polar organic solvent is chosen to be more volatile than the aqueous continuous phase, so that the preferential evaporation of oil droplets before the continuous phase leads to discrete polymeric particles rather than continuous films of polymers. Depending on the solutes used and their phase behaviour, a wide variety of complex and functional particles can be generated.

An emulsion is an opaque, heterogeneous mixture of two immiscible liquid phases in which one phase is dispersed in the other continuous phase. There are two simple categories of emulsion: oil-in-water (o/w) and water-in-oil (w/o) emulsions. More complex emulsions are oil-in-water-in-oil (o/w/o) emulsion and water-in-oil-in-water (w/o/w) emulsions. Emulsions produced by blending two pure immiscible liquid phases are usually not kinetically stable and revert to the bulk phases with time. Such instability issues can be minimised by the addition of a surface-active agent (surfactant), which protects the droplets of discrete phases from coalescence. Surfactants are usually amphiphilic organic compounds with both a hydrophobic group and a hydrophilic group. For example, figure 1.1 shows how the surfactant functions to prevent the coalescence of oil droplets in an oil-in-water emulsion, where aqueous solution with a surfactant serves as the continuous phase and oil droplets act as the discrete phase. As the hydrophobic tail interacts more strongly with the organic oil than the continuous phase, surfactants initially dispersed in the aqueous solution migrate to the oil-water interface, forming a micelle-like structure with hydrophobic tails immersed in the oil core and hydrophilic heads at the outer layer. This micelle structure is used to against oil droplets to coalesce with their neighboring oil droplets.

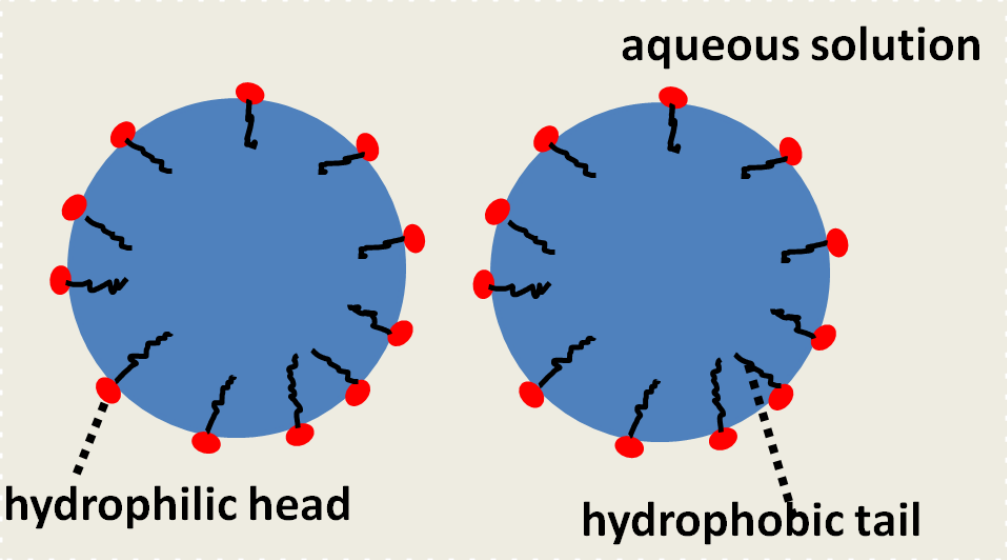

Figure 1.1. Schematic representation of an oil-in-water emulsion with oil droplets (blue color) dispersed in aqueous solution (grey color). The red head at the oil/water interface indicates hydrophobic group, the dark tail immersed in the oil droplets indicates the hydrophobic group.

Figure 1.2 schematically shows the evolution of an oil-in-water emulsion during evaporation. In Figure 1.2a, polymer was dissolved in volatile organic solvent and then emulsified into aqueous solution using a suitable surfactant. The prepared emulsion was allowed to dry freely in ambient conditions. From figure 1.2a to 1.2b, there was an emulsion-to-dispersion transition: most oil droplets had dried out and formed discrete polymer particles, while the continuous phase had not evaporated fully. In figure 1.2c, complete evaporation of aqueous solution formed a dry deposit with discrete polymeric particles.

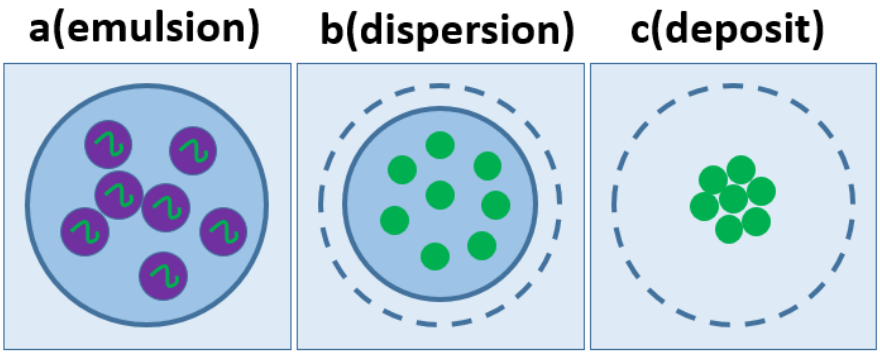

Figure 1.2. Schematic representation for the evolution of drying an oil-in-water emulsion. The dashed black line indicates the initial boundary of the continuous aqueous phase. The purple indicates the oil solvent, the green indicates the polymer dissolved inside, and the green circle indicated the solid spherical polymeric particles.

The emulsion solvent evaporation is mainly a two-stage process, the emulsification of polymer solution comprising encapsulated substance, followed by polymeric particle hardening through solvent evaporation and polymer precipitation.

For the emulsification process, two main strategies are being used for the formulation of emulsion:, oil-in-water single emulsion (o/w) and water-in-oil-in-water double emulsion (w/o/w). This study focuses on the former method using a single o/w emulsion to prepare polymeric particles. During emulsification, the polymer solution was broken up into oil droplets by high shear stress, supplied by either by a homogenizer, sonicator or microfluidics, in the presence of a dispersant. The average size of oil droplets can be tuned by adjusting the shear stress, type and amount of surfactant, interfacial tension between the aqueous phase and oil phase, and temperature. A larger shear stress, a higher concentration of surfactant (below critical micelle concentration, CMC), or a smaller interfacial tension, resulted in a lower size of average oil droplets within the emulsions. With regard to the size distribution of formed oil droplets and hence that of the final resultant particles, in general, homogenizer and sonicator provide non-uniform shear stress, producing polydisperse oil droplets and resultant particles, while microfluidics offers more uniform shear stress, leading to highly monodisperse emulsions.

During the polymer particle hardening process, the initial emulsion transforms into final polymeric particle through solvent evaporation and polymer precipitation. The solvent eliminates by diffusion through the aqueous phase and evaporates out into ambient air. This

process is vital for particle morphology and is also of significant influence on the encapsulation and release behavior of functional species.

Rosca et al. [1] investigated the mechanism of the solvent evaporation from oil-in-water emulsions. Poly(dl-lactide-co-glycolide) (PLGA) was dissolved in dichloromethane (DCM) to prepare 1 wt% polymer solutions as the oil phase, 0.1 wt% poly(vinyl alcohol) (PVA) aqueous solution served as the aqueous phase. After emulsification in a homogenizer, one drop of emulsion was placed on a microscope slide and sealed with a cover glass, thus the evaporation of DCM was confined through the interface between the emulsion and air at the edge of the glass slide. Figure 1.3a shows that oil droplets near the edge of the cover slip shrank and those in the center remained unchanged. Initially the drop of emulsion is approximately saturated with DCM, so transport of DCM is only possible near the interface of emulsion and air, leading to fast shrinkage of oil droplets at the periphery. As the emulsion dried further, the oil droplet at the center remained constant until the decreasing concentration of solvent moved from the edge towards the middle of aqueous solution. Figure 1.3b shows complete transformation of DCM droplets into polymer particles after solvent evaporation. Compared with Fig. 1.3a, there is a notable decrease in particle size, which was several times smaller than the initial oil droplet. This shrinkage can be predicted by a shrinkage factor,

$$\alpha = \frac{d_{oil}}{d_p} = \left(\frac{V_{oil}+V_p}{V_p}\right)^{1/3} = \left(1 + \frac{100\rho_p}{c_p}\right)^{1/3},$$

where d_{oil} is the diameter of initial oil droplet, d_p final particle size, V_{oil} the oil droplet volume, V_p the particle volume, ρ_p polymer density (g/ml), c_p polymer concentration (% w/v). This theoretical shrinkage factor of initial oil droplet size to final particle size was contrasted with measured ratios, a good agreement indicating the particle is free of solvent after complete drying of the emulsion.

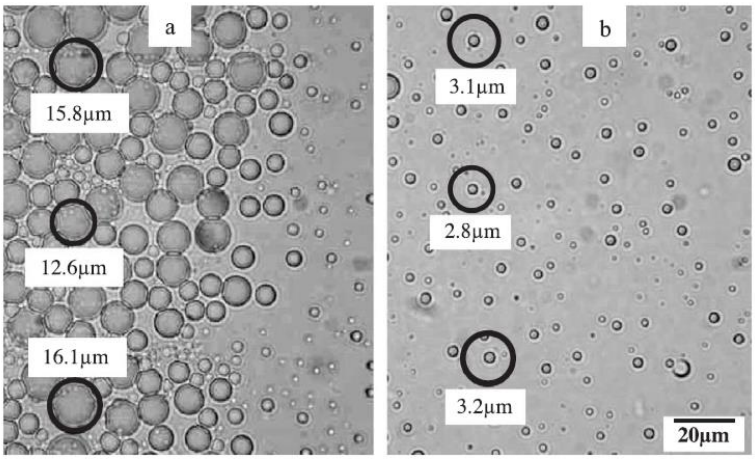

Figure 1.3. Optical micrograph showing oil-in-water emulsions at early and final stages of drying. PLGA, 1% w/v; 1% w/v PVA. (Reprinted (adapted) with permission from ref [1]. Copyright {2004} Journal of Controlled Release).

1.3 Structured and functional particles

Based on the solutes used and their phase behaviours in oil-in-water emulsion, the emulsion solvent evaporation induced assembly can create a wide variety of complex and functional particles, like solid microspheres, core-shell microcapsules, Janus, nano or microparticles. [1-16]

1.3.1 Solid microspheres

Emulsion solvent evaporation has been widely used for encapsulation of functional cargoes from simple pharmaceutical products to protein and DNA. This oil-in-water emulsion solvent evaporation is generally preferred for hydrophobic active drugs, which are soluble in water-immiscible organic solvents. In this case, polymer and active drugs are dissolved in the organic solvents as the discrete phase. The resulting oil phase is then emulsified with an aqueous solution with proper dispersant agent. Fuminori Ito et al. [2] employed this method to produce drug-containing polymeric microspheres. For the formulation of oil-in-water emulsion, poly (lactide-co-glycolide) (PLGA) was used as the matrix-forming agent, anti-tuberculosis drug, Rifampicin (RFP), was chosen as a hydrophobic model to be encapsulated into the polymeric microspheres. When chloroform was used as the solvent, RFP/PLGA microspheres with the active ingredient RFP dispersed throughout the PLGA

matrix was produced, as is shown in Figure 1.4. Spectrophotometer measurements showed the drug loading efficiency in PLGA microparticles reached 90.4%.

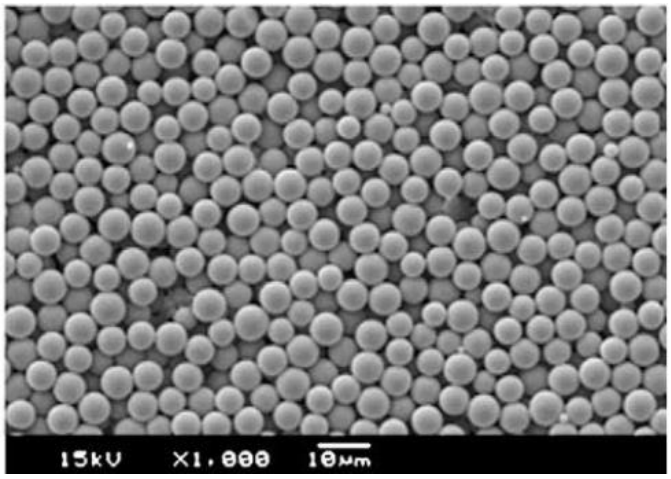

Figure 1.4. SEM images of the RFP/PLGA microspheres prepared by emulsion solvent evaporation. (Reprinted (adapted) with permission from ref [2]. Copyright {2009} European Polymer Journal).

1.3.2 Microcapsules with a polymer shell and a liquid core

Microcapsules with polymer shells and liquid cores allow a versatile approach for the encapsulation of functional cargoes. Various studies [3-11] of the fabrication of core-shell microcapsules will be discussed in detail in later chapters in this thesis.

1.3.3 Janus particles

Symmetric objects are most desired in everyday life as symmetric stimuli of any kind are easily processed by visual system. For instance, most people prefer symmetric faces. However, if we look underneath and go deeper into the human body, we will find most objects like liquids and proteins by being asymmetric are able to achieve complex energy processes. Thus this asymmetry feature of molecules has been utilized as a promising resource in fabrication of advanced functional materials, contributing to a rich functionality, like variations in mechanical strength, amphiphilicity, conductivity, optical activity, etc. Especially, Janus particles of block copolymers with different parts covalently bound are tunable in microstructures, compositions, physical and chemical properties. Figure 1.5 [12] shows a wide variety of different Janus particles that have been manufactured so far,

consisting of simple spherical, cylindrical, disc-shaped, dumbbell-shaped, and capsule Janus particles.

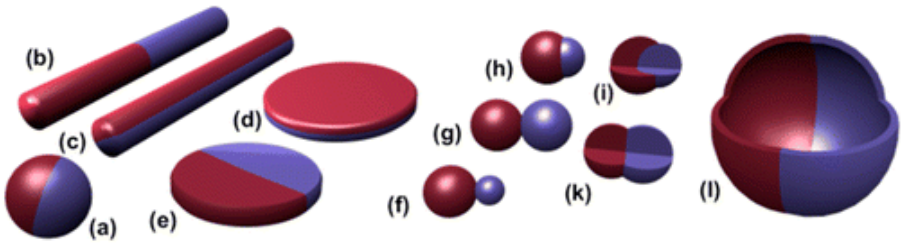

Figure 1.5. Schematic representation for Janus particles with various structures (adapted from ref [12]).: (a) spheres, (b-c) cylinder, (d-e) disc-liked particles, (f-k) dumbbell-shaped particles, (i) capsule-shaped Janus particles. The colour variation indicates different molecules. (Reprinted (adapted) with permission from ref [12]. Copyright {2013} American Chemical Society).

Deng and co-workers [13] have demonstrated a facile approach to fabricate Janus particles of block copolymers using emulsion solvent evaporation. Poly(4-vinylpyridine)-based block copolymers performed as the shell-forming materials, in particular, P4VP block should have more affinity to the aqueous solution than the other block molecules, and the other block had a better solubility in the organic solvent. Figure 1.6a schematically shows the production of the Janus particles of PS-b-P4VP by emulsion solvent evaporation. The block copolymer is completely dissolved in DCM and then emulsified with an aqueous solution. As the good solvent evaporates, the P4VP block first start to aggregate to form a cluster at the interface of oil droplets and aqueous solution, due to the relatively poor solubility of P4VP in DCM. After the good solvent dries out, the other block precipitates and forms another head at the opposite end (see figure 1.6b). We should note that, the interfacial tensions between P4VP, the other block polymer and the aqueous phase play an important role in the final particle morphology (core-shell, Janus or two individual spheres). When an ionic surfactant, like SDS, is used, core-shell capsules are formed rather than Janus particles. These Janus particles can be readily tuned by varying the block fraction.

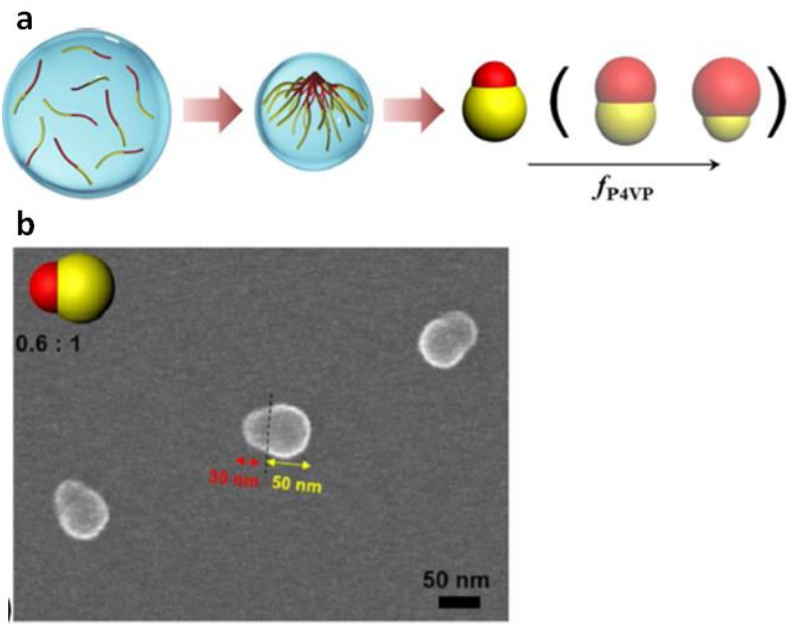

Figure 1.6. (a) Schematic illustration for production of Janus particle by emulsion solvent evaporation induced assembly of P4VP-based diblock copolymers. (b) SEM images showing PS-b-P4VP Janus particles. The scale bar is 50 nm. (Reprinted (adapted) with permission from ref [13]. Copyright {2016} American Chemical Society).

1.4 Inkjet printing

Evaporation of a bulk dispersion of colloidal dispersions can generate a 2D films of colloidal crystals. It is challenging to design desired patterns unless templates are being used. Evaporation of drops of colloidal dispersions can produce dots or spheres of colloidal particles. This drop can be deposited onto substrates to prepare desired patterns, (ordered arrays, lines and large-scale patterns), via inkjet printing. Contrasted with templated assembly, inkjet printing provides attractive advantages, including digital control over patterns, a contact free-process, efficient use of material, allows precise positioning of inks onto target surfaces, is applicable to flexible substrates and is easy to scale-up. Due to such promising features, inkjet printing has been widely used in a wide variety of applications, such as conventional graphics, conducting polymeric devices, organic light-emitting diodes and biological microarrays.[13-16]

Figure 1.7 shows two main strategies for inkjet printing, i.e., continuous inkjet (CIJ), where ink droplets are generated in a continuous stream; drop-on-demand (DOD), where ink droplets are only generated when required.

In the CIJ method, fluids are forced through a small orifice to form a jet. This jet is then treated with a perturbation, which breaks up the jet into a continuous stream of ink droplets due to Plateau-Rayleigh instability [14]. When a cylindrical stream of ink is subjected with perturbations, pinched sections with higher pressure and bulged areas with lower pressure take place. This pressure ingredient causes a fluid flow toward the lower pressure area, enhancing the bulged area and reducing the pinched area. Eventually pinch-off occurs with transformation of bulged areas into individual spherical droplets to minimise its surface energy. By adjusting the size of continuous ink droplets with tunable pressure perturbations and giving electrical charge to the formed ink droplets, the CIJ guides the continuous droplets landing onto substrates to form desired patterns. The major advantages of the CIJ method are high speed of printing (up to 10m/s) and being free from nozzle clogging as the jet is continuous. However, the CIJ method also suffers from a problem of low efficiency of ink use as only a small amount of inks are directed to the substrate under electrostatic deplection, and most inks are recycled during printing.

The DOD method is a more refined way to produce ink droplets rather than simply break-up of a jet into a continuous stream. Besides, the positioning of ink droplets is by moving the printhead or the underlying substrates rather than manipulating inks. For the DOD method, there are two major methods, i.e., thermal DOD printing and piezoelectric DOD printing. Thermal DOD printing utilizes a heating element as an actuation device. When a pulse of current is applied to the heating element rapid vaporization of the ink occurs, causing a bubble in the chamber and pushes a droplet of ink out of the orifice, due to increased pressure. In the piezoelectric DOD process, a piezoelectric material behind the nozzle changes its shape under a voltage, generating a pressure pulse in the chamber and hence forcing the ink out of chamber to form a droplet of ink. To vaporize ink and form a bubble, the thermal DOD printing requires that a volatile component must be included in the ink. The piezoelectric method allows a wider choice for ink formulations, as there is no need for volatile components.

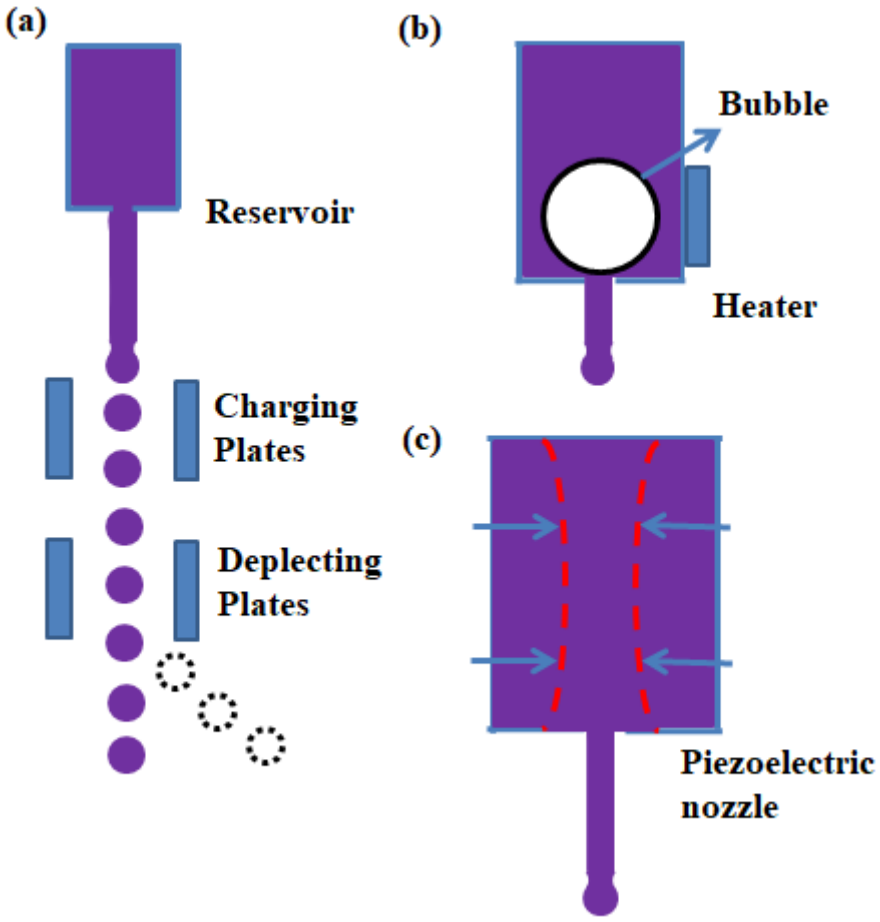

Figure 1.7. Cartoon representation of methods of inkjet printing of ink droplets activated by (a) continuous inkjet printing, (b) thermal DOD printing, (c) piezoelectric DOD printing.

A major obstacle in inkjet printing is failure of pinch-off of liquid inks into spherical droplets during ejection from the orifice, especially for printing of polymer solutions with high concentrations and high molecular weights, owing to the viscoelasticity of the polymer solutions. During jetting, the polymer chains undergo a coil-to-stretch transition, which increases the break-off time of ink droplets and hence inhibits the droplet-detachment process from the orifice. This problem can be solved by confining the high concentration of polymer in a discrete phase of an oil-in-water emulsion. As the surface tension of the oil-water interface shields the oil droplets against deformation during jetting, shear only occurs in the polymer-free continuous phase, leading to a low viscosity even at a high concentration of polymer. Johns and Bain [15] pointed out this strategy of using emulsions to print high-molecule weight polymers can allow a concentration which is an order of magnitude higher than is possible in binary solutions. In their work, polystyrene was

dissolved in methyl benzoate as the discrete phase, and then emulsified with an SDS-stabilized aqueous solution.

After emulsification, the prepared emulsions containing polystyrene at an overall concentration of 3.8 wt% was printed successfully. As a comparison, the highest concentration of polystyrene in a methyl benzoate solution that could be printed was below 0.25 wt% (see figure 1.8a and 1.8b). In their experiment, methyl benzoate is less volatile than water, thus the preferential evaporation of the continuous phase gives rise to coalescence of oil droplets, forming a continuous film of polystyrene after complete drying of the oil phase, as is shown in figure 1.8c.

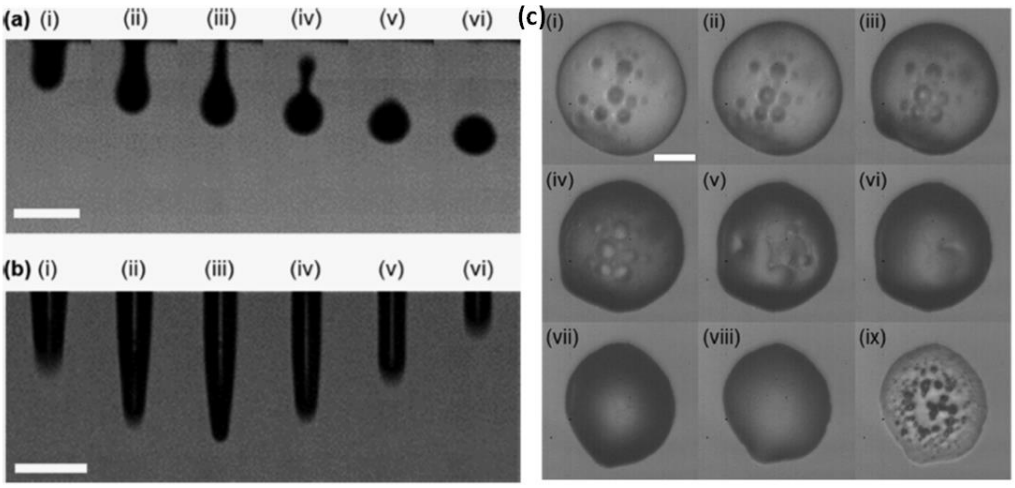

Figure 1.8. Jetting dynamics of (a) oil-in-water emulsions containing polystyrene at an overall concentration of 3.8wt%, (b) polystyrene solutions at a concentration of 4 wt%. (c) Optical images showing evolution of emulsion droplets on a glass cover slip: a continuous film of polystyrene is observed at (ix). (Reprinted (adapted) with permission from ref [15]. Copyright {2017} American Chemical Society).

Deng and Bain [16] coupled inkjet printing with emulsion solvent evaporation to produce deposits of polymeric particles. The emulsion possessed a dispersed phase containing a volatile non-polar solvent, so the organic solvent evaporated before the continuous phase to prepare polymeric particles rather than continuous films of polymer. Polymeric particles were formed in situ during the drying process of ink droplets on substrates within a few seconds, as is shown in figure 1.9. The drying process was recorded through the substrate.

Figure 1.9 also shows the evaporation and deposition process, including three stages. During stage 1, an ink droplet containing multiple oil droplets landed onto a glass coverslip and wetted the underlying surface with its maximum contact line, meanwhile oil droplets spread outward toward the footprint of the ink droplet. From stage 1 and stage 2, there was a transition from emulsion to dispersion, where most oil droplets had transformed into solid particles due to the prior evaporation of volatile solvent. During stage 3, particles near the contact line were driven inward by an inward capillary force and a uniform deposit formed after complete drying of the continuous phase.

This strategy of combining inkjet printing with emulsion solvent evaporation has been demonstrated to be applicable for a wide range of solvents, polymers, and functional species [16]. For the choice of the non-polar solvent, not only should the solvent be more volatile than water, but it should be considerably soluble in water, so the prior evaporation of oil can be achieved by diffusion through the water and evaporation into the surroundings. When DCM, chloroform or were chosen as the non-polar solvent, polymeric particles were all observed with these solvents. However, ethyl acetate-based formulation resulted in a larger average size of polymeric particles, owing to the low density of ethyl acetate than the aqueous solution. As a result, oil droplets moved upward to the top of the ink droplet and coalesced with their neighbouring droplets to some extent, thus increasing the average size of final formed particles. For the choice of polymers, polystyrene with different molecular weight dissolved in DCM are also investigated to test the sensitivity of this approach. Polystyrene with a molecular weight from 35 kg mol^{-1} to 253 kg mol^{-1} can be dissolved in the emulsion to print in a continuous and reproducible manner. Moreover, functional cargoes can be encapsulated inside the particles after printing, showing potential for functional patterning by inkjet printing.

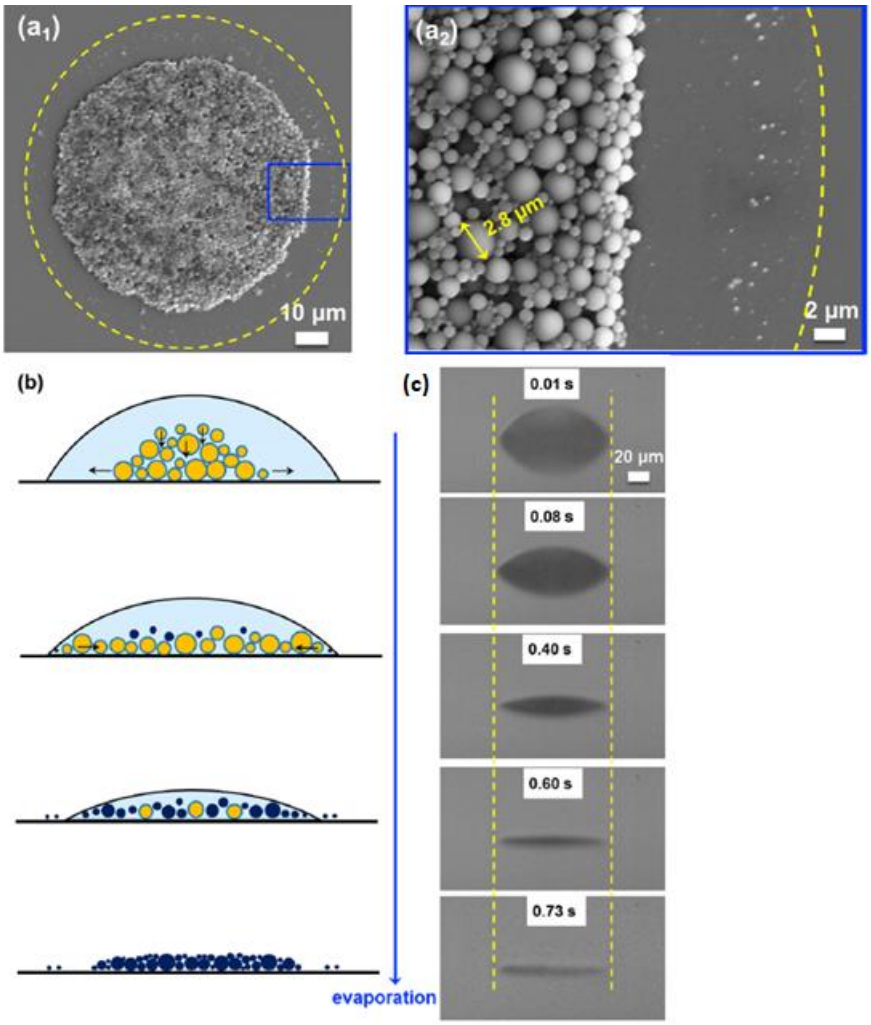

Figure 1.9. (a_1) SEM image showing a dry deposit of polymeric particles on a coverslip, (a_2) SEM image at a higher magnification displays the morphology of spherical particles near the contact line. (b) Schematic representations and (c) optical graphs indicate the evolution of a printed emulsion droplet drying on a glass coverslip from the side view. The dashed yellow line points out the location of the initial contact line of the ink droplet. (Reprinted (adapted) with permission from ref [16]. Copyright {2018} American Chemical Society).

1.5 Droplet-based microfluidics

During emulsification, polymers solution can be broken up into oil droplets by high stress supplied by homogenizers, sonicators or microfluidics in the presence of a dispersant. The emulsification process mainly determines the size distribution of oil droplets and hence the final microparticles. Emulsions prepared by homogenizer or sonicator offer polydisperse emulsions, giving rise to a broad size distribution of oil droplets and final polymeric particles,

which is undesired in most applications of inkjet printing, like graphics where a uniform deposit with minimum use of ink is favoured. In the experiments of Deng and Bain, a high-speed homogenizer was used as a tool to prepare emulsions, leading to polydisperse particles with size from submicron to 2.8 microns. These heterogeneity issues can be improved with the aid of microfluidics to prepare homogeneous emulsion droplets.

Droplet microfluidics is a system that manipulates two immiscible liquids to form periodic and monodisperse emulsion droplets under steady flows. In general, the dispersed phase and continuous phase flow into the microfluidic system via two separated channels. These channels usually meet at a junction, where deformation of the two-phase interface occurs. A typical routine of formation of emulsion droplets is as follows: first, the dispersed phase bulges and forms a finger at the junction, then two phases flow coaxially through an elongated narrow channel, at which point the dispersed phase is pinched off to form discrete oil droplets. More experimental details about the break-up process will be elaborated in section3.

1.5.1 Generation of uniform oil-in-water emulsions by microfluidics

The method for generating emulsion droplets can be either passive or active. This section concentrates on the passive method in closed microchannels by the pressure-driven flow of the dispersed and continuous phases to deform the interface and generate discrete droplets. Based on different geometry of the channel junctions, microfluidics can be mainly divided into three categories: co-flowing, cross flowing (also called T-junction), and flow-focusing microfluidic device, as is shown in figure 1.10. Microfluidics with a flow-focusing geometry can provide a larger shear force, thus favouring the production of micron-sized droplets.

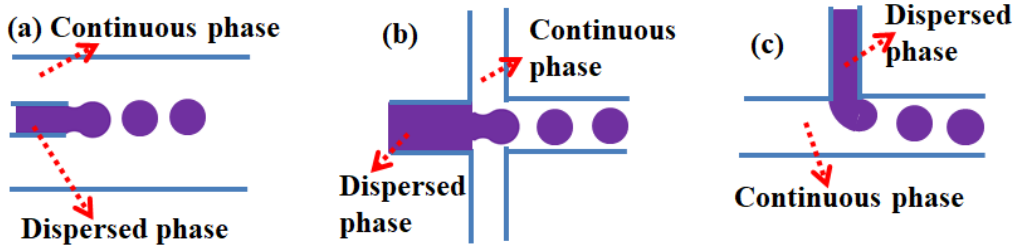

Figure 1.10. Schematic diagrams of formation of oil droplets at a junction of (a) coaxial, (b) flow-focusing, (c) T-junction microfluidic setup. The black arrows indicate the flow directions.

The flow rate of both phases, the fluid property (viscosity, capillary force, etc.) and the channel geometry of the microfluidic device determine a high shear stress that deforms the interface. Droplet formation is governed by a competition between the deformation of the o/w interface achieved by viscous shear and the resistance of the interface to deformation arising from surface tension. Thus the behaviour of droplet formation in microfluidics can be described by the Capillary number, *Ca*, which compares the relative importance of the viscous force to the interfacial force, given by $Ca = \frac{\mu G a_0}{\gamma}$, where μ is the viscosity of liquid phase, *G* is the strain rate, a_0 is the characteristic size of the finger at the junction, γ is the interfacial tension.

Anna et al. [17] experimentally observed four distinct modes of droplet formation in a microfluidic flow-focusing device as a function of capillary number. The capillary number *Ca* can be readily tuned by varying either the flow rate of continuous flow or that of dispersed flow. The four modes of droplet breakup are geometry-controlled, dripping, jetting and thread formation breakup, as can be seen in figure 1.11.

When the capillary number is low, the geometry of the flow focusing orifice determines the droplet deformation. As the two immiscible phases flow coaxially through a contraction area, the dispersed phase flowing in the inner channel forces the continuous phase in the outer channel to flow at a higher rate. A higher pressure is generated at the finger of the dispersed flow, which then breaks into discrete drops by the geometry constraint of the flow-focusing channel. The oil drops generated in this area are highly monodisperse with a diameter slightly larger than the junction width. After the breakup, the interface retracts to a position upstream of the junction.

As the capillary number increases, the finger of the dispersed phase becomes thinner as the local shear stress increases and remains at a fixed pinch-off point rather than retracting upstream. In this dripping regime, the generated drops are again uniform but smaller than the junction width. The droplet size decreases continuously with the increasing continuous phase flow rate and the increasing capillary number. The continuous increase of the capillary number leads to a transition of dripping to jetting regime, where the finger of the dispersed phase extends beyond the exit of the contraction area and forms a long jet before breakup. The finger still breaks into discrete drops due to Rayleigh capillary instability. However, the formation of micro drops in this regime is not stable, and the drop size is relatively less uniform and larger than the junction width. Besides, the finger of the dispersed phase pinch-off at random point, decreasing the controllability of the microfluidic device.

As surfactant at a moderate concentration is added, a fourth mode of breakup “thread formation” shows up between the geometry constraint and dripping regime . Thin long threads are drawn from the finger of the dispersed phase and are observed between micro drops. These threads further form into tiny satellite drops compared to the primary large micro drops.

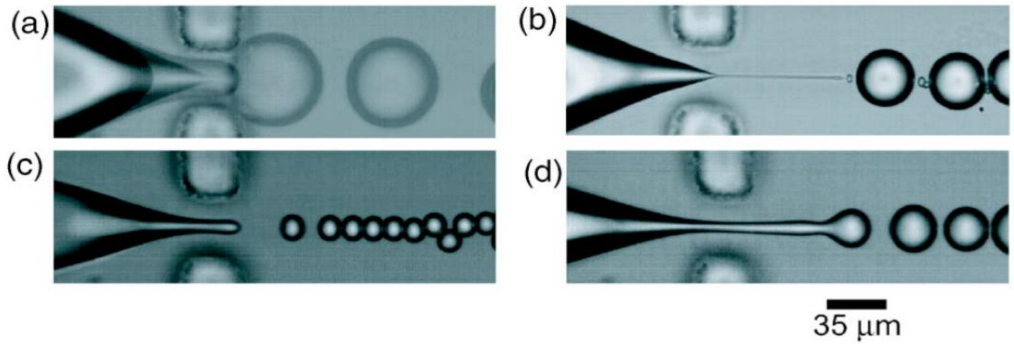

Figure 1.11. Representative images of the four main modes of droplet breakup at a flow-focusing junction, (a) geometry-controlled, (b) thread formation, (c) dripping, (d) jetting regime. (Reprinted (adapted) with permission from ref [17]. Copyright {2006} Physics of Fluids).

1.5.2 More complex emulsions by microfluidics

Microfluidics can prepare not only isotropic emulsion droplets with controllable size, but also anisotropic microspheres with complex morphologies and chemical compositions, for example Janus droplets [18] and double emulsion droplets [19].

Nisisako and co-workers [18] reported a microfluidic approach to produce monodisperse Janus emulsion droplets, in which two miscible phases are confined in different hemispheres. The microfluidic device contains a Y-shaped channel with two dispersed flows, which meets with the aqueous phase at a junction, where a bi-phase Janus droplet occurs under the right flow conditions, as is shown in figure 1.12. In their experiments, carbon black and titanium oxide are dispersed respectively in an organic solvent (isobornyl acrylate, IBA) to prepare black and white IBA monomers. These two phases are then sheared by an aqueous solution of PVA at the junction to produce two-colored Janus spheres. After polymerization, Janus particles with hemispherical parts of black and white are observed (figure 1.12b). The polymeric Janus particles are highly uniform in size, with a coefficient of variation less than 2%. Moreover, by integration of multiple channels in microfluidics, scale-up of production of emulsions can be achieved, showing a promising future in practical manufacture.

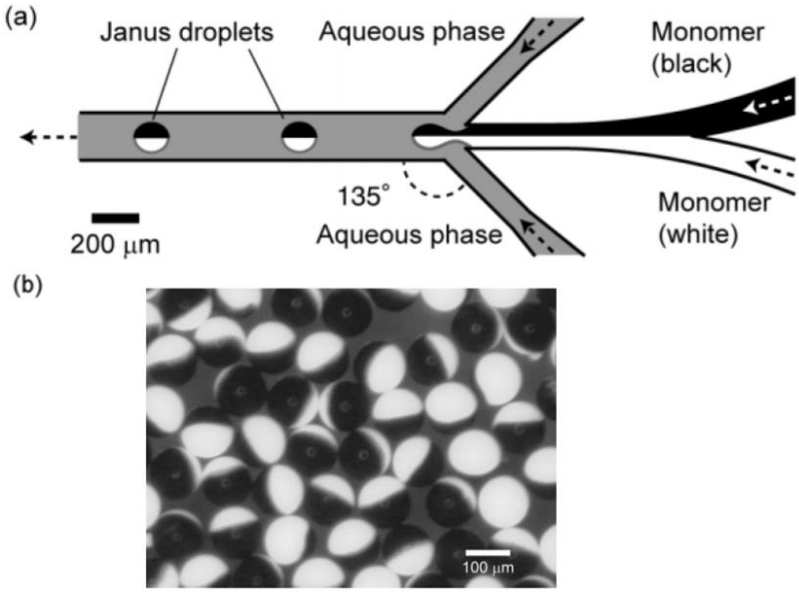

Figure 1.12. (a) Schematic diagram for production of monodisperse Janus emulsion droplets, (b) SEM images showing bicolored Janus particles after drying of emulsion. (Reprinted (adapted) with permission from ref [18]. Copyright {2006} Advanced Materials).

Okushima and co-workers [19] demonstrated a novel method to prepare monodisperse double emulsions by a two-step process using microfluidics. To prepare a water-in-oil-in-water (w/o/w) emulsion, first aqueous solutions broke up as internal droplets at an upstream hydrophobic T-junction, then the organic phase containing the internal droplets was captured as external droplets downstream at a hydrophilic T-junction, as is shown in figure 1.13. By control of the relative rupture rates at upstream and downstream junctions, monodisperse emulsions with highly controlled number of internal droplets in the double emulsions can be formed. Reversal of the wetting conditions of the two junctions can lead to monodisperse oil-in-water-in-oil (o/w/o) double emulsions.

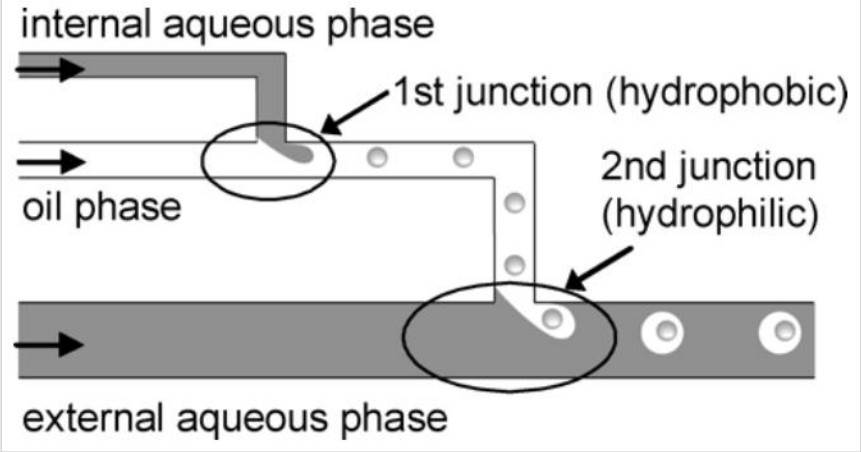

Figure 1.13. Schematic representation of preparation of monodisperse water-in-oil-in-water (w/o/w) double emulsions using T-shaped junctions of microfluidics. (Reprinted (adapted) with permission from ref [19]. Copyright {2004} American Chemical Society).

Though monodisperse double emulsions can be generated readily by the above method, one problem relating to inkjet printing is the size of the external drops, which is too large compared to the inkjet nozzle, especially when multiple drops are contained inside, and thus not be suitable for printing. Shrinking the internal droplet size is a feasible way to address this problem, which can be achieved by droplet splitting [20].

Similar to the generation of emulsion droplets in microfluidics, the droplet splitting method can either be passive or active. Anna and co-workers [20] developed two methods for

passively splitting drops into daughter drops in a microfluidic device with a simple configuration: either using a T-shaped junction (figure 1.14a), or placing an isolated obstruction in the microchannels (figure 1.14b). For the first method, a continuous phase carrying droplets flows through a central channel, and then breaks up into two side streams at a T-junction. The stagnation point of the T-junction provides sufficient extensional stress to split the drops. By investigating the breaking and non-breaking conditions with different flow rates and droplet size, they found relatively large drops always break up regardless of the flow rate. However, small droplets flow alternatively into two side channels without breakup under low flow rates. This can be explained by the Rayleigh-Plateau instability theory, where a stream of liquid will break up into small drops when its length exceeds the perimeter. A large droplet can be easily elongated to a desired length by the geometry constraint from the microchannel, while a high flow rate is required to stretch the small drops to the desired length-to-perimeter ratio. Another advantage of passive break up of droplets by T-junction is to be able to produce asymmetric size distribution of daughter droplets. Different size ratios of daughter droplets in the two side channels can be tuned by varying the length of microchannels, which determines the resistance of the corresponding side channels. Comparing with an electric-splitting device where current is inversely proportional to the resistance, the ratio of flow rates in the two side channels is inversely proportional to the ratio of channel length.

As for the second method, the location of obstacles determines the relative size of the two daughter droplets. The droplet size is nearly proportional to the distance between the obstacle and the channel sidewalls. Equal daughter droplets generate only when the obstruction is in the centre of the channel. This method is sensitive to the location of the obstacle and the upcoming droplets, thus decreasing the splitting precision. Both passive droplet splitting strategies allow a versatile manipulation of the ratio of daughter droplet volumes. However, since the volume of the droplet scales with the cube of the radius, droplet splitting is an ineffective method to achieve a large reduction in droplet radius.

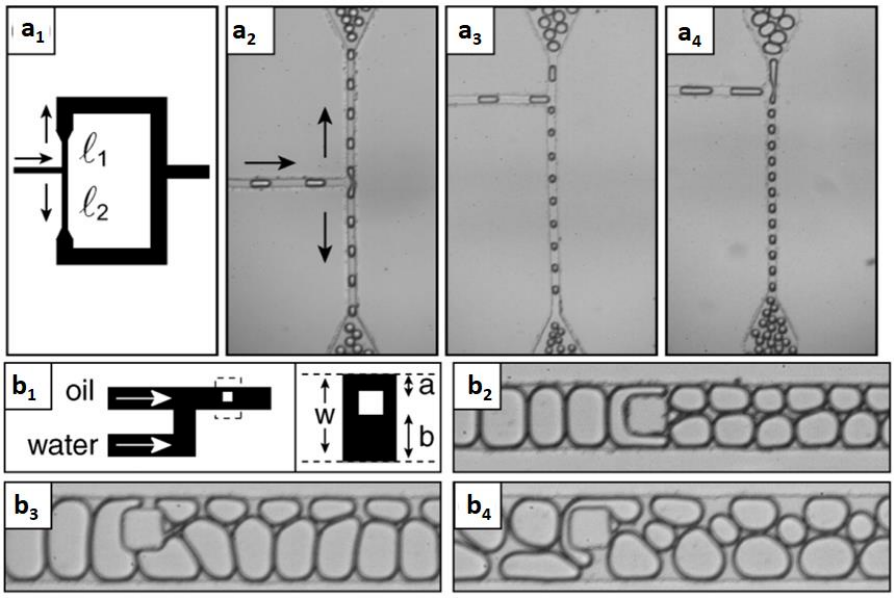

Figure 1.14. Cartoons indicating (a) passive breakup of droplets at T-shaped junction, a_2- a_4 shows the effect of side channel length on the volume of daughter droplets, the ratios of length of two side microchannels are 1:1, 1:5.2 and 1:8, and the corresponding ratios of daughter droplet volumes are 1:1, 5.2:1, and 7.5:1. (b) Passive splitting of droplets by isolated obstructions at different locations of a microfluidic channel. (Reprinted (adapted) with permission from ref [20]. Copyright {2004} PHYSICAL REVIEW LETTERS).

1.6 Droplet evaporation

When an ink droplet has been jetted from an inkjet nozzle and dries out on a surface, the particles suspended inside are left on the surface, forming different deposition patterns, for example, a ring deposit, a central deposit, or a uniform deposit. Controlling the deposition patterns is of great importance in a wide range of applications, such as inkjet printing of functional materials, photonic crystals, and automatic DNA mapping.[11] Droplet evaporation is directly related to the resulting deposition pattern, and thus has attracted interest from numerous groups in recent years.

Deegan [21] explained the well-known coffee ring phenomenon: when a spilled drop of coffee dries on the table, it leaves a ring-like stain along the perimeter of the footprint. This deposition pattern arises from an outward capillary flow inside a pinned sessile droplet, where liquid evaporating at the edge needs to be replenished from the interior due to geometrical constraints. Otherwise, the three-phase contact line (TCL) would gradually

vanish away during drying (Figure 1.15). The resulting outward capillary flow carries dispersed particles to the edge and form a ring-like stain there after the droplet dries completely.

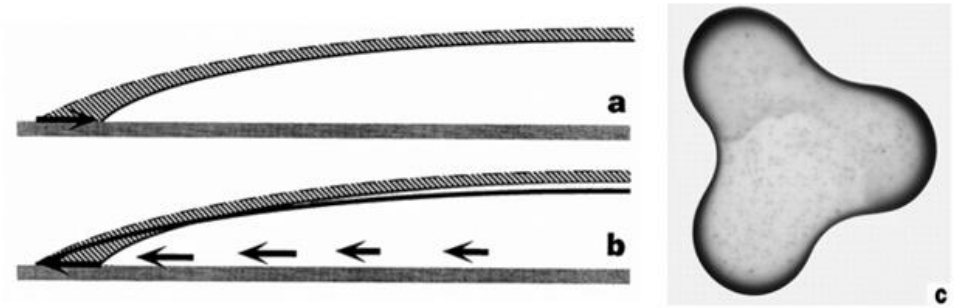

Figure 1.15. Mechanism of outward flow inside sessile droplet. (a) Without flow droplet shrinks. (b) With an outward compensating flow, the TCL remains constant. (c) A ring deposit by drying a coffee drop of two-centimetre diameter with 1 wt% polystyrene microspheres. (Reprinted (adapted) with permission from ref [21]. Copyright {1997} Nature).

In the experiment of Hu and Larson [22], the sessile droplet was assumed to maintain a shape of spherical cap and a pinned TCL. The shape of a drop resting on a surface (Figure 1.16) is controlled by the Bond number and the Capillary number. The Bond number compares the importance of gravitational force to the surface tension: $Bo = \frac{\rho g R h_0}{\sigma}$, where ρ is the fluid density, g is the gravitational acceleration, h_0 is the initial height of the droplet, R is the contact line radius and γ is the air-liquid surface tension. Gravity tends to flatten the liquid-air interface, while the surface tension acts to minimise the liquid-gas interfacial area. The viscous force tends to deform the droplet surface by the friction of the liquid flow. The Bond number and the capillary number are both close to zero for picolitre drops of printable fluids, hence the effects of gravity and viscosity are negligible compared to the surface tension. In the absence of strong Marangoni flows [22], sessile picolitre drops can be assumed to have the shape of a spherical cap.

The shape of a sessile droplet on an ideally flat and chemically homogeneous surface is determined by Young's equation (Figure 1.16), $\gamma_{SG} = \gamma_{LG} cos\theta_c + \gamma_{SL}$, where *S* is the solid phase, *L* is the liquid phase, *G* is the gas phase; γ_{SG}, γ_{LG}, γ_{SL} are the interfacial energies between these phases, respectively. Young's equation comes from a balance of forces at the three-phase contact line (TCL) parallel to the substrate surface. Stress vertical to the

substrate surface does not need to be balanced because the substrate is elastic. This equilibrium contact angle depends on the physical properties of three phases. A higher surface tension at the liquid-air surface or a more hydrophobic substrate leads to a higher contact angle. In real cases, the contact angle is also dependent on surface roughness and chemical heterogeneities.

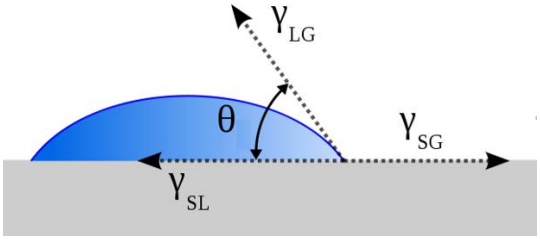

Figure 1.16. Schematic of a liquid sessile droplet showing a thermodynamic equilibrium between the three phases.

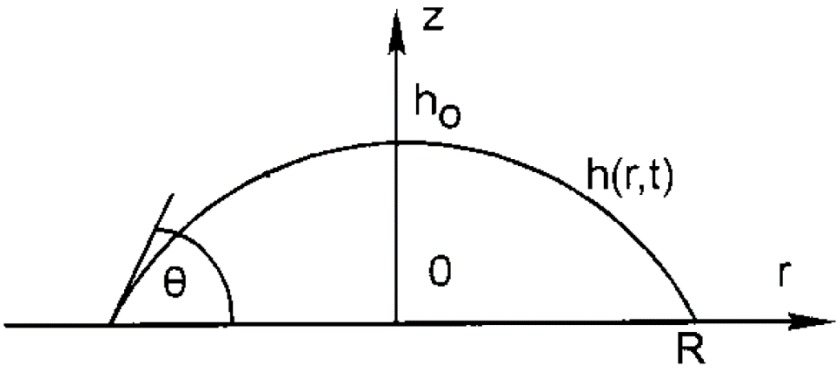

Figure 1.17. A sessile droplet in a cylindrical coordinate system with radial coordinate r and axial coordinate z. The local height is *h(r,t)*.

When we add or remove a small amount of liquid from a liquid drop, the contact line will often remain pinned with an increase or decrease of the contact angle. This phenomenon is known as contact angle hysteresis. Thus, a sessile droplet has a spectrum of contact angle from a maximum one (i.e. advancing angle) to a minimum one (i.e. receding angle). The equilibrium contact angle is somewhere between these values. The maximum advancing

angle can be measured by placing a droplet on the surface and continuously adding a small amount of liquid by a need syringe until the TCL moves, thus the contact angle just before the movement of TCL can be considered as the maximum advancing angle. The minimum receding angle is measured by the similar way by continuously removing part of the liquid until the TCL moves. These values can then be compared with the contact angle at the beginning of drying and a transition from pinned to moving contact line in an experiment. For pure liquids, a good agreement is found. The contact angle hysteresis can explain the mechanism of the contact line pinning and depinning before the completion of droplet drying.

Picknett and Bexon [23] analysed the evaporation of sessile droplets and proposed that droplet evaporation generally involves two distinct stages, a constant droplet radius stage (CR) and a constant contact angle stage (CA). In the first stage, droplet dries with a pinned contact radius and a decreasing contact angle, while during the second stage the contact radius is fixed, and the contact angle recedes. Hu and Larson [22] measured the variations of contact radius in the whole drying process by using a fluorescence microscope to track 0.75-µm-diameter fluorescent particles suspended in a water droplet with an initial radius of 0.85 mm and height of 0.329 mm. The corresponding droplet profile and radius at different times can be mapped by the locations of the florescent particles. The result shows CR takes most of the evaporation time (95%), and thus the TCL is assumed to be pinned during drying.

For a sessile pinned droplet, the residual droplet profile at different times can be calculated. The height of droplet from the centre to the surface can be described as a function of time: $h(r,t) = \left(\sqrt{\left(\frac{R}{sin\theta}\right)^2 - r^2}\right) - \frac{R}{tan\theta}$, where θ is the contact angle. The residual volume of the droplet is $V(t) = \frac{\pi h(0,t)[3R^2 + h(0,t)^2]}{6}$. Hu and Larson [22] measured the droplet height as a function of time and thus obtained the evaporation rate by calculating the residual droplet volume. They found that the evaporation rate remained nearly constant for a droplet with initial small CA (less than 40^0), which agrees well with the numerical simulations of Picknett and Bexon [23], and Hu and Larson [22]. Because the vapour diffuses relatively quickly compared to the change in the droplet shape, the diffusion-controlled evaporation was considered as a quasi-steady state process. The diffusion equation $\frac{\partial c}{\partial t} = D\Delta c$ reduces to a Laplace equation: $\Delta c = 0$, where *c* is the vapour concentration, *D* is the vapour diffusivity. Assuming that the atmosphere just above the droplet surface is saturated with vapour and that the vapour concentration is constant along the surface, Picknett and Bexon [23],

Deegan et al [21] derived an exact solution for the evaporation flux along the surface of pinned sessile droplets. They showed that the local evaporation flux along the air-liquid interface increases monotonically from the droplet centre to the droplet edge and diverges at the contact line (see Figure 1.18). The expression for evaporation flux along the air-liquid interface is $J(r,\theta) = J_0(\theta)(1-r^2)^{-\lambda(\theta)}$, where $\lambda(\theta) = 0.5 - \frac{\theta}{\pi}$ and $J_0(\theta)$ is the evaporation flux at the droplet centre, note that this equation is only applicable when θ is less than 90^0. While for the case of θ >90^0, the local evaporation flux will exhibit a non-monotonically distribution with the highest evaporation flux at its maximum radical distance.

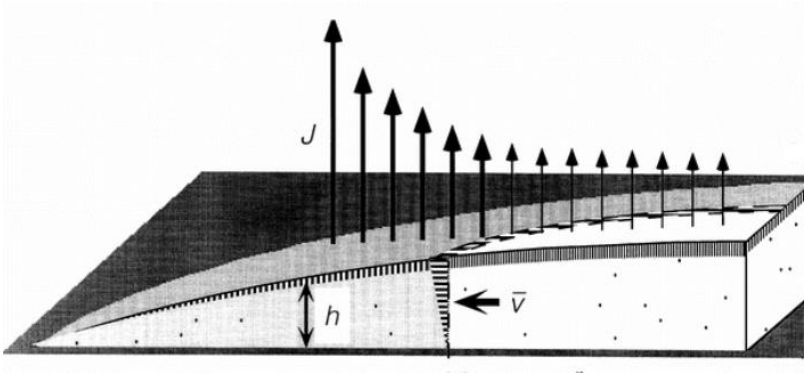

Figure 1.18. Non-uniform distribution of evaporation flux at the droplet surface. Note that this only applies for θ less than 90^0. (Reprinted (adapted) with permission from ref [22]. Copyright {2002} American Chemical Society).

Hu and Larson [24] later used the empirical expression of the evaporation flux as a boundary equation to calculate the temperature field inside drying droplets. The results show the non-uniform evaporation induces a temperature gradient along the droplet surface and hence a surface tension gradient, which leads to a circular Marangoni flow in which fluid flows along the surface from a low surface tension area to a high surface tension area. This circular Marangoni flow tends to redistribute the particle to the centre of the droplet and form a uniform deposit or centre deposit. Thus, the coffee ring phenomenon is dependent not only on a pinned CR, but also on suppression of the circular Marangoni flow. A dimensionless Marangoni number describes the strength of the Marangoni flow, given by $M = \frac{\Delta\gamma L}{\eta D}$, where $\Delta\gamma$ is the surface tension difference between the edge and the bulk of the droplet, L is the length of the contact radius, η is the solvent viscosity, and D is the diffusion coefficient. This expression shows the magnitude of Marangoni flow is proportion

to the surface tension difference and reversely proportional to the solvent viscosity and the diffusion rate.

1.7 Manipulation of deposit pattern

The ring stain is detrimental in many applications, like in inkjet printing, where uniform deposits are desired. Thus, there has been an increasing interest in understanding the drying process and controlling the deposit pattern of inkjet droplets to form uniform deposits or films. Many strategies have been studied to control the deposit pattern, such as the use of interactions among particles or between particles and solvents, manipulating the three-phase contact line (TCL) and refining substrates.

1.7.1 Interactions among particles or between particles and solvents

Weon and Je [25] demonstrated an inward radial capillary force between particles and air–liquid interface near the droplet edge can contribute to a uniform layer of particles. They investigated the drying process of 1.5-millimeter-diameter water droplets with 2- and 20-micron-diameter polystyrene particles. For larger particles with 20 μm diameter, the particles first move outward and then reverse toward the centre until the motion is limited by a closed packing near the centre. The reversal is faster for particles near the edge. However, most particles with 2-micron-diameter constantly move outward and form a coffee ring after drying. This indicates the reversed motion of polystyrene particles is easier for large particles than the small particles. Figure 1.19 shows real-time micrographs of the profile evolution of a water droplet. The result indicates the geometry constraint plays an important role in the particle motion, the pinned contact line and descending air-liquid interface contributes to both outward motion in the first stage and reversed motion later. There is a competition between the outward force caused by the outward capillary flow (coffee ring effect) and the inward force due to the interactions between particles and air-liquid interface. When the inward force dominates the outward force, the reversal takes place. The distance of reversed particle motion increased with evaporation time and the contact angle evolution. This conclusion is useful to explain a deposition pattern from our recent work [16], where most particles locate in a circular deposit with size slightly smaller than the initial contact line, while a few small particles are left near the edge (figure 1.20), consistent with the idea that the inward capillary forces acting on the small particles is less able to overcome the coffee ring effect.

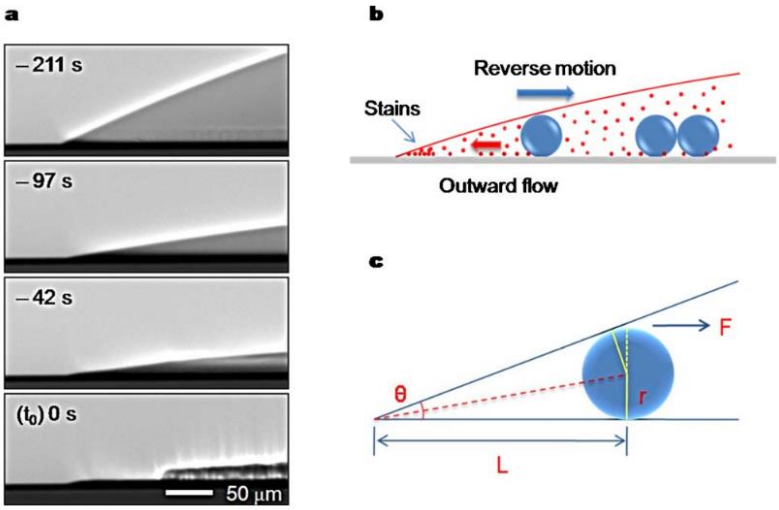

Figure 1.19. (a) X ray graphs showing the evolution of a droplet profile. (b, c) A schematic diagram showing the mechanism of reverse motion. (Reprinted (adapted) with permission from ref [25]. Copyright {2010} Physical Review E).

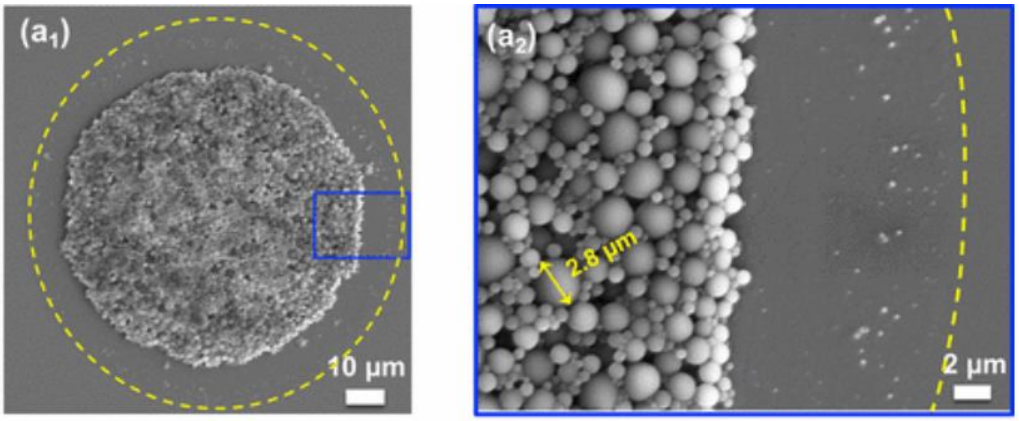

Figure 1.20. (a) SEM images of a deposit from a printed emulsion drop. (b) An enlargement of (a) showing the distributions of polystyrene particles near the contact line. (Reprinted (adapted) with permission from ref [16]. Copyright {2018} American Chemical Society).

Yunker and co-workers [26] found the strong capillary forces among anisotropic particles can suppress the coffee ring effect efficiently. Ellipsoid particles can deform the air-liquid interface more than spherical particles and generate a strong inter-particle interaction due to the immersion capillary force. When particles initially dispersed inside the droplet are

trapped at the air-liquid interface during drying, the strong inter-particle interactions cause a loosely packed structure at the interface, which prevents the particles moving toward the contact line and contributes to a uniform pattern. They used water droplets containing micrometre-sized polystyrene particles with same volume fraction of 0.5% but with different shapes, i.e. spherical and ellipsoid particles. Figure 1.21 compares the distribution of spherical particle and ellipsoid particles at four representative evaporation times. During the drying process, the contact line of the water droplets remained pinned, which caused an outward capillary flow that carries spherical particles to the edge of the droplet efficiently. A loosely packed structure between ellipsoid particles reduced the mobility and led to a uniform deposit on the interface of water-air. Mixing a small fraction of ellipsoidal particles with spherical particles also eliminated the outward particle movements.

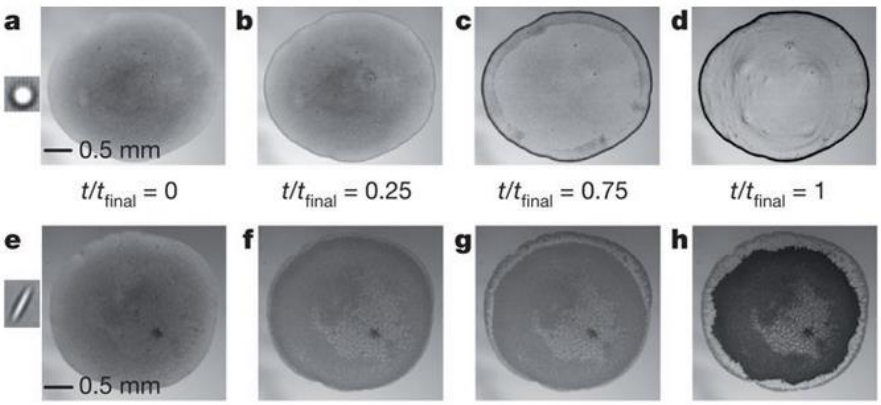

Figure 1.21. Images showing particle transport over time during evaporation of water-based droplet with spherical particles (a-d) and ellipsoid particles (e-h). A ring-like stain (d) is formed with sphere particles, a uniform deposit (h) is formed with ellipsoidal particles. (Reprinted (adapted) with permission from ref [26]. Copyright {2011} Nature).

Jaeger et al. [27] reported that a strong particle-liquid surface interaction can be used to suppress the coffee ring effect. They used a suspension of dodecanethiol-ligated 6-nm gold nanoparticles in a toluene droplet to form a highly ordered monolayer after drying. Two factors are essential in the self-assembly process (figure 1.22): the dodecanethiol ligand molecules generate a strong particle-air-liquid interface interaction that fix particles in the surface, thus inhibiting particles moving to the droplet edge; a rapid evaporation ensures particles transfer to the droplet interface otherwise they cannot form a continuous monolayer across the whole interface before the contact line shrinks. Therefore, there is a

competition between convection and diffusion, which means the rate of droplet surface descending must be larger than the diffusive rate of particles, in order to trap the gold particles at the air-liquid interface. The monolayer structure eventually deposits at the substrate surface. Without the ligand molecules or large Peclet number, less uniform deposits forms, for example, a ring-like deposit.

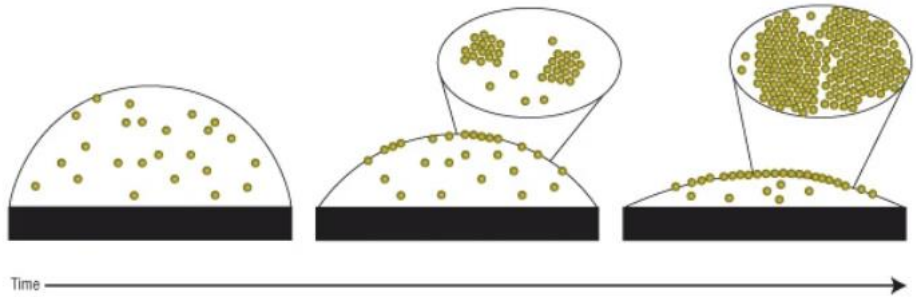

Figure 1.22. Schematic representations of the self-assembly of nanoparticles at the receding interface of liquid-air. (Reprinted (adapted) with permission from ref [27]. Copyright {2006} Nature Materials).

Song and co-workers [28] presented a strategy to reinforce the interactions between particles to weaken the coffee ring effect. They prepared latex spheres with a core-shell structure, which consists of a hydrophobic polystyrene core and a hydrophilic poly(methyl methacrylate) (PMMA)/ poly(acrylic acid) (PAA) shell. In aqueous dispersions, these shells stretch and stick with adjacent shells by a brush-like structures, thus providing a strong assembly force due to hydrogen bonds. This special assembly force can suppress the particles from moving outward to the three-phase contact line.

1.7.2 Moving contact line and refining substrates

For sessile droplets on a substrate with a high receding angle, the TCL moves inward early in the drying process, compared to sessile droplets with a low receding angle.

Orejon et al [29] studied the dynamics of the three-phase contact line of droplets of water, and TiO_2 nanofluids on substrates with various hydrophobicity. A layer of 1-μm thickness of parylene, Cytop, and PTFE were coated respectively onto a silicon wafer surface to increase its hydrophobicity, and the corresponding contact angle of water droplet was 104°, 108° and

114°, respectively. For pure water droplets, two distinct types of the contact line behaviour were observed, depending on the hydrophobicity of the substrates. The contact line receded steadily on hydrophobic surface (coated with Cytop, and PTFE) until the evaporation was complete. The contact line remained pinned for most of the evaporation time on less hydrophobic substrate (silicon or coated with parylene).

Figure 1.23 compares the evolution of contact radius between a pure water droplet and a water droplet with a small amount of TiO_2 nanoparticles, from the work of Orejon et al. [29]. For water droplets with 0.001 wt% TiO_2 nanoparticles, the presence of particles promoted the pinning of the contact line on hydrophilic surfaces, increased the pinning time from 40% (without particles) to 70% of the whole evaporation time. The addition of nanoparticles reinforces the energy barrier the contact line needs to overcome in order to slide on the surface. The origin of the energy barrier is not clear in their study, but may be related to the interactions between particles, substrate surface and the air-liquid interface. The experimental results show a direct correlation between the particle concentration and the depinning distance of the contact line from the slide point to the re-pin point. The higher concentration of particles increases the number of particles aggregating at the contact line, thus increasing the energy barrier for depinning. Besides, the addition of nanoparticles alters the surface roughness and chemical heterogeneities once they are adhered to the substrate surface, thus attributing to the pinning of the contact line. The pinning and depinning behaviour of contact line can be characterized by a competing force between the surface energies and an intrinsic energy barrier. For a simplest case of pure liquid water on a surface, the triple contact line is in balance before droplet evaporates, given by Young's equation. A slight decrease in contact angle increases an inward force which tends to slide the contact line. The energy barrier therefore acts to restrain the potential slide. When the contact angle decreases to a receding value, the depinning force is large enough to overcome the intrinsic energy barriers, leading a sliding contact line until the droplet dries out. For a droplet with a small initial contact angle, the depinning force is not large enough to resist the energy barrier. In this case, the contact line appears to fix on the surface for most of the evaporation time.

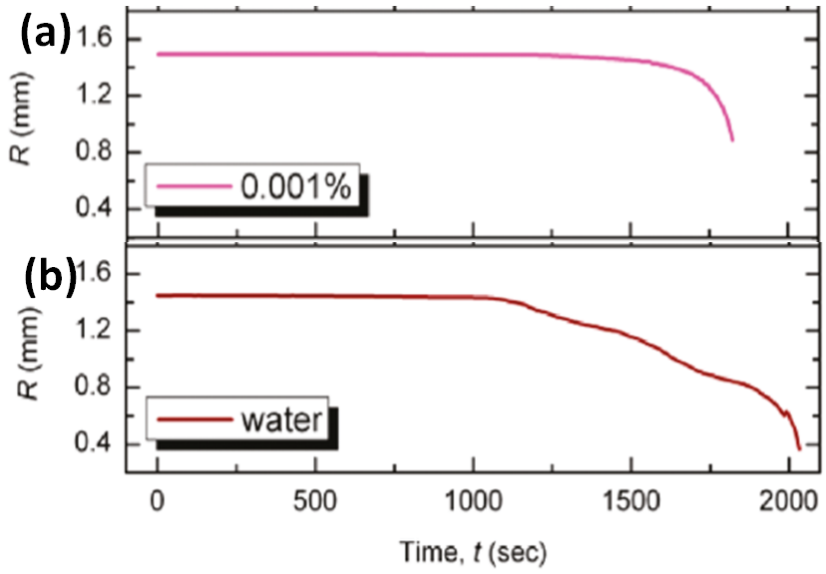

Figure 1.23. Diagrams showing the evolution of contact radius during dying of water droplet with (a) 0.001 wt% and (b) 0 wt% TiO_2 nanoparticles. (Reprinted (adapted) with permission from ref [29]. Copyright {2011} Langmuir).

In addition to the methods listed above, there are other strategies to obtain a uniform deposit pattern. For example, our group [30] recently used an evaporation-driven sol-gel transition in laponite suspensions to control the convective flow during evaporation. A sol is a dispersion of particles in a fluid. A gel is a complex fluid/soft solid consisting of a three-dimensional cross-linked system, which exhibits no flow at low stresses. The enhancing elasticity and yield stress within the gel dominate radial capillary force and resist outward particulate motion. The gelation occurs rapidly compared to the overall evaporation time, which is a crucial factor for suppressing the radial capillary force. Due to a non-uniformity of evaporation rate, gelation takes place from the edge, gradually extending to the centre. The experimental results show that the gelation time (i.e. the extent of outward flow) determines the final deposition profile: a sensible gelation time results in a uniform deposit profile in the most desirable case, otherwise it forms a dome-like shape with an inadequate outward flow or a coffee ring with too much.

Adding surfactant to droplets is also an efficient way to control the deposition morphology. When solvent evaporates out from the air-liquid surface, the surfactant contained inside is left locally. The enhanced evaporation at the edge increases the surfactant concentration there, which causes a surface tension gradient along the droplet surface and hence a

Marangoni flow. Tadashi et al.[31] demonstrated that with a small amount of surfactant (about 0.05 wt%) added to the droplet, the final polymer profile is able to change dramatically from a ring-like shape to a flat one. The reason might be the surface tension of the solvent decreases sharply at a low concentration of surfactant (less than 0.5%). Thus a slightly gradient of surfactant concentration could result in a high difference of surface tension among the droplet surface. They observed when the initial surfactant concentration is less than 0.002%, the outward capillary force is still prevail over the Marangoni force, thus leading to a ring-like deposit. As the initial surfactant concentration increases, more particles aggregate at the centre as the Marangoni force prevails over the capillary force. When the number increases to 0.05%, a desirable uniform particle distribution pattern occurs. Above this value, no more particles will move to the central area. Besides, they investigated the effect of surfactant on droplets of different solvents (DPMA, ACE) with varied polymer concentration (5%, 10%, 20% by weight) and initial droplet volume (350, 500, 750pl). In all cases, flat profiles of depositions are observed. This demonstrates the addition of surfactant is an effective method for controlling the deposition pattern and has a wide applicability, regardless of the type of solvent and surfactant, polymer concentration and droplet scale.

1.8 Structure of the thesis

Chapter 2 describes the main experimental methods and set-ups used in this thesis.

The work in chapter 3 has been published and the chapter draws on the published paper with additional experimental detail. Most of the work in this paper is contributed from myself as the first author, except one part in chapter 3.3.4 explaining why small (non-Brownian) particles should be less mobile than large particles, which was added by my supervisor Colin Bain. In Chapter 3, I first show that o/w emulsions containing PS/DCM droplets produced in a flow-focussing junction evaporate in a cast film and form monodisperse particles that self-assemble into an ordered hexagonal array. I then show that these same emulsions can be printed successfully to produce dry deposits with a narrow particle size distribution. I discuss how the physics of drying influences this process. The conditions are optimised to minimise the amount of break up and coalescence of droplets during the jetting process and hence to produce particles with a narrow size distribution. Variation in the droplet size and polymer concentration can be used to control the final particle size. I explore the conditions necessary to obtain dense monolayer deposits of both small (~1 μm diameter) and larger (2–3 μm diameter) particles. Finally, I discuss the

prospects for manufacturing more complex functional particles by inkjet printing of emulsions and the limitations of the approach.

In chapter 4, I explore the mechanism of formation of core-shell microcapsules by emulsion solvent evaporation, where the emulsion contains a shell-forming polymer, a core-forming poor solvent dispersed in a good solvent as the oil phase. Evaporation of the good solvent induces an internal phase separation within the oil droplets of the emulsion, triggering the formation of microcapsules. First, I study the wetting conditions necessary to induce the internal phase separation within emulsions. Then I construct a ternary phase diagram to predict the formation process, either polymer-rich phase or poor solvent-rich phase can phase separate from the bulk solution, depending on the ratio of polymer to poor solvent. Then the physical parameters affecting the phase separation and hence the final morphology are explored. Finally, the conditions are optimised to minimise the effect of pseudo partial wetting to obtain a uniform morphology of core-shell microcapsules.

In chapter 5, I demonstrate a strategy to prepare self-assembly hierarchically macro-mesoporous material with tuneable pores by inkjet printing monodisperse emulsions containing silica nanoparticles dispersed in the discrete phase. I first show that emulsions

containing silica nanoparticles dispersed in the discrete phase evaporate in a cast film and form monodisperse silica microporous particles that self-assemble into hexagonal arrays with macro-pore structures. I then show these emulsions can be inkjet printed to form a monolayer closely packed porous networks with interconnected macropores and mesopores. Depending on the surface functionalities of the silica nano-particles, both oil-in-water and water-in-oil emulsions are applicable for this strategy. These M-M Patterns are repeatable from silica nanoparticles of a wide range of sizes. Finally, I discuss the prospects for manufacturing more complex hierarchically porous materials, like Macro-Meso-Micro structures by introducing porous nanoparticles as the primary building blocks.

Chapter 6 describes concluding remarks and suggestions for future developments.

As for the appendices, appendix 8.1 is from a published paper of a collaboration work between my colleague Renhua Deng and myself, who are the first author and second author, respectively. In this paper, my contribution includes using microfluidics to prepare uniform oil-in-water emulsions and using inkjet printing to fabricate monolayer of monodisperse patterns on the modified substrates. Moreover, all the SEM images in appendix 8.1 are

measured by me. Appendix 8.2 is a Matlab program code used for analysing the experimental data in this thesis.

2 Experimental Method

Materials. Polystyrene (PS, M_W = 35 kg mol^{-1}), Poly(methylmethacrylate) (PMMA, M_w = 35 kg mol^{-1}), poly(vinyl alcohol) (PVA, M_w = 31−50 kg mol^{-1}, 87−89% hydrolysed) were purchased from from Acros Organics; sodium dodecyl sulfate (SDS, > 99%), chloro(dimethyl)octylsilane (CDMOS, 97%) and hexamethyldisilazane (HMDS, 98%) were obtained from Sigma-Aldrich; Silica nanoparticles (unmodified surface, dispersed in water, 30 nm nominal diameter; acrylate surface, dispersed in ethanol, 30 nm and 200 nm nominal diameter) were purchased from Micromod; dichloromethane (DCM, >99%) was obtained from Fisher Scientific, chloroform-d ($CDCl_3$) from Fisher Scientific UK; hexadecane (>98%) from TCI; 2-pentanol (>98%) were obtained from Fisher Scientific. All chemicals were used as received.

2.1 Development of experimental setup

Experiments were conducted in a lab with ambient relative humidity R_H (30-50%) and temperature (about 295 K). Besides, R_H in the vicinity of the printing rig can be controlled from 20% to 90% using a humidity chamber, where the glass coverslips are placed inside an enclosed chamber with a supply of a combination of saturated and dry air.

Figure 2.1 shows my experimental setup for sequential generation of an o/w emulsion by microfluidics and inkjet printing of emulsion droplets. This experimental setup allows production of formulations using microfluidics, and at the same time delivers the formulations through a tubing to a nozzle for inkjet printing. Polymer particles with the same size are obtained after drying of ink drops. A major benefit of integrating formulation production with inkjet printing is to generate unstable or reactive formulations without shelf life or instability problem. The first step of my research aims to produce a uniform monolayer of deposits with monodisperse particles. Recently our group proposed a method to produce deposits of polymeric particles by inkjet printing an oil-in-water emulsion, where the discrete phase evaporates faster relative to the continuous phase. The preferential evaporation of the discrete phase contributes to the formation of polymeric particles in the drying drops. A circular deposit with compact polymeric particles over the entire footprint of the droplet was generated after complete drying of the ink drop. However, the particles formed in this way were not uniform, ranging from submicron to 2.8 microns, which resulted

in a deposit with non-uniform thickness. One primary reason is the emulsion with polydisperse internal oil drops. To overcome this problem, microfluidics is introduced to improve the monodispersity of the oil drops. Then the emulsions are used for inkjet printing to produce uniform deposit. The process of my research is set out below.

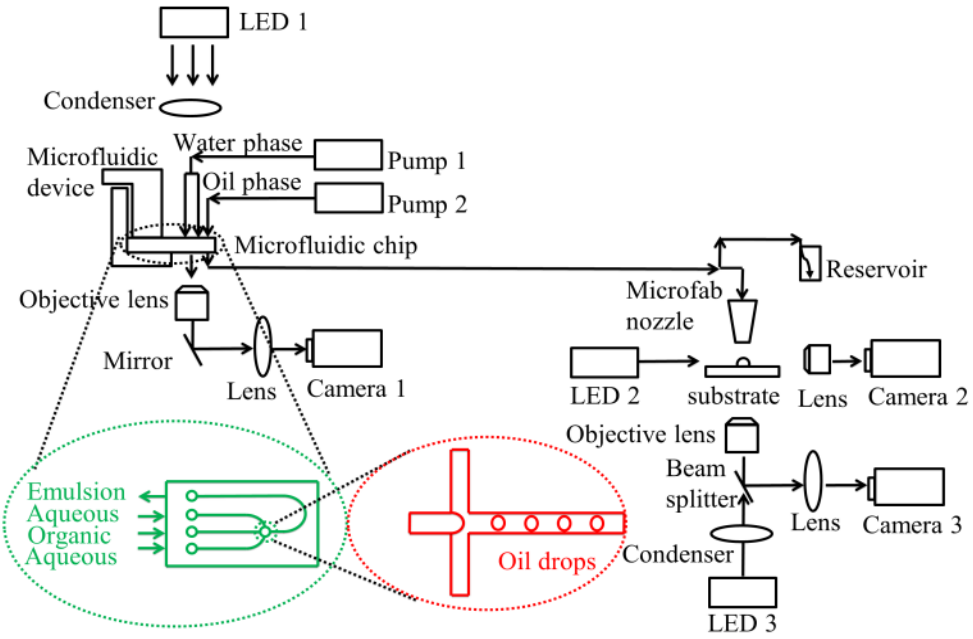

Figure 2.1. Schematic of experimental setup for sequential generation of an o/w emulsion by microfluidics and inkjet printing of emulsion droplets.

2.2 Preparation of o/w emulsion by microfluidics

In this paragraph I take polystyrene in dichloromethane as a model system to produce highly monodisperse oil-in-water emulsions by microfluidics.

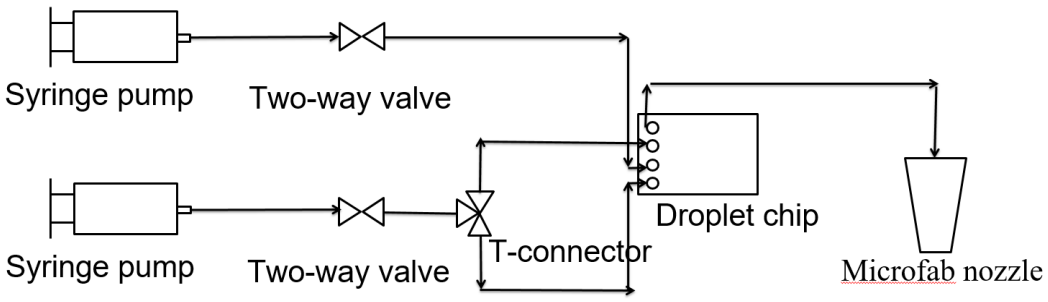

Figure 2.2. (a) Sketch of the microfluidic system. Fluids are supplied via two syringe pumps, tubing, connectors, and microfluidic chip with a flow-focusing junction. Aqueous and organic solutions flow into the channel from the three inlets, and meet at the flow-focusing junction, where the emulsion formation takes place. The corresponding emulsion flows out from the outlet.

2.2.1 Fabrication of uniform oil-in-water emulsion by microfluidics

Polystyrene was dissolved in DCM to prepare polystyrene solutions with concentrations of 0.5–5.0 wt%. SDS was dissolved in deionized water to produce aqueous solutions with concentrations of 0.05–1.0 wt%. The solutions were filtered through a 0.2-µm PTFE filter and loaded into two gastight borosilicate syringes with PTFE-tipped plungers and Luer-lock connectors (1 mL, KR Analyticals). The oil phase and aqueous phase were injected into a microfluidic chip (small quartz droplet chip, 5 µm etch depth and 500 µm channel width, Dolomite) with a flow-focusing junction (5 µm etch depth and 8 µm junction width) via two syringe pumps (AL1000, World Precision Instruments), FEP tubing (1/16" o.d. × 0.25 mm i.d., Dolomite) and connectors (Top Interface 4-way, Linear Connector 4-way, Dolomite). The oil phase was injected into the central channel of the microfluidic chip, and the water phase was divided into two flows via a Y-connector (Y Assembly PEEK, IDEX) before entry into the two side channels of the microfluidic chip. The flow rate of the aqueous phase remained constant at 2 µL min^{-1} and the flow rate of the oil phase was varied from 0.2–1 µL min^{-1}. The oil phase and water phase met at the flow-focusing junction of the microfluidic chip, where the generation of oil drops took place. The production process was monitored by high-speed camera (Optronis) at 1000 frames per second (fps) for a resolution of 800 × 600.

SDS is added as a surfactant to stabilize the oil drops. However, surfactant will increase the viscosity of liquid droplet in the latter stages of drying and hence decreases the mobility of

particles, which is a disadvantage factor for uniform deposit. The surfactant will also be left behind in the deposit. A minimum amount of surfactant is desired in the formulation of the emulsion. The effect of surfactant concentration will be investigated later in this thesis. The ratio of the continuous phase (i.e. aqueous solution) to the discrete phase (i.e. oil solution) is dependent on the rate of the corresponding syringe pumps. Our group previously used a mixture of oil solution (1 ml) and water solution (3 ml), which were emulsified in a vial at a high rotor speed (26k rpm) for 30 s by a homogeniser (T10 Ultra Turrax, IKA). However, homogenization of the mixture in this way broke up the oil phase into small oil drops with different sizes ranging from submicron to about 15 microns. In order to increase the monodispersity of the oil drops, a droplet-based microfluidic system is used in the emulsion generation. To reduce the likelihood of particulate obstruction in these channels, solutions are filtered using a 0.2μm-filter before entering the microfluidic system. Then the liquids are driven into corresponding channels separately at a constant rate using syringe pumps (AL1000-220, Aladdin Programmable Syringe Pump). This flow rate is proportional to the corresponding pressure inside the microchannel.

To ensure a stable generation of oil drops, the ratio of oil phase flow rate (v_o) to aqueous phase flow rate (v_a) must be kept in a suitable range. Outside the range, backward flow or chaotic flow will be observed. In the stable stage of drop generation, highly uniform organic drops containing polystyrene are generated. The whole process is as follows (Figure 2.3): first, the front of the organic phase extrudes at the junction of the microfluidic chip and forms a finger, then a part of the finger is pinched off in the contraction channel by a high shear force, after that the rest of the finger recoils back and waits for the next pinch off. As a result, the aqueous liquid carrying the discrete organic drops flows through the exit of the junction and forms into oil-in-water emulsions in the outlet channel of the microfluidic system. The presence of the surfactant stabilises the discrete organic drops, otherwise the oil drops tend to merge with the adjacent drops in the wide channel. The microfluidic drop formation is controlled by a competition between the deformation by the shear force and the resistance of deformation by the capillary force. For a given organic phase flow rate, increasing the aqueous phase flow rate will reduce the organic drop size, as the shear force is more pronounced against the resistance of interfacial deformation. Our experiment generates stable organic drops when the ratio of the organic flow rate to the aqueous phase flow rate is between 1 and 10. Within this range, drops with high monodispersity are achieved. There are two ways to estimate the monodispersity of the organic drops. One way is to image the generated drops in the wide channels just after the flow-focusing junction

and compare the drop to a reference length which in the image is the junction width (8 μm). Once the discrete drop sizes are obtained, the monodispersity between drops can be calculated. It should be noted that the drop size measured in this way may be larger than the diameter of a spherical droplet of equal volume, because the drop is compressed when its diameter is larger than the etch depth of the microfluidic chip channel (5 μm). The other way is to measure the size of the corresponding particles after drying the emulsion. During drying, the more volatile DCM drops containing polystyrene dry preferentially compared to the surrounding aqueous solvent. As a result, each single drop forms into a spherical polystyrene particle before the aqueous phase dried out. The oil drop sizes can be determined by the equation $\frac{4}{3}\pi d^3 = \frac{4}{3}\pi r^3 \times \%V$, where d is the polystyrene particle radius, r is the organic drop radius, and $\%V$ is the volume fraction of the polystyrene in the DCM solution. In my experiments, the solutions are prepared by weight. To convert % by weight to % by volume, the values need to be multiplied by the ratio of densities of DCM to PS, which is a factor of 1.27. For accurate calculations, one needs to allow for the solubility of DCM in the aqueous phase: for a 2% solubility and the highest flow-rate ratio of 10:1, around 20% of the DCM would dissolve in the aqueous phase within the microfluidic device. In my experiment, when the organic drop size is nearly 6.1 ± 0.5 μm by the first method, the corresponding particle size is about 2.2 ± 0.05 μm and the real organic drop size is about 5.94 ± 0.14 μm by the second method, given the result is slightly larger than the real case in the first method, there is a good agreement between these two methods.

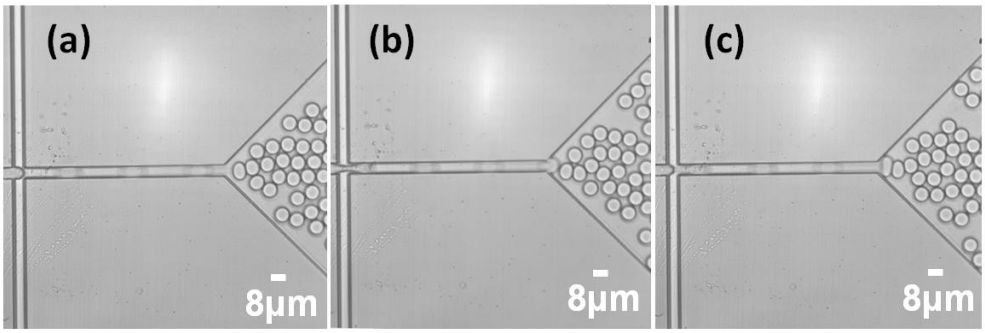

Figure 2.3. Micrographs of the evolution of oil drops at the junction of a microfluidic channel. (a) Organic phase bulges at the junction, (b) interface deforms by the local shear stress, (c) a single drop detaches from the finger and the rest of the finger coils back. The depth of the flow-focusing junction is 7 μm.

Outside this range of flow rates, chaotic flow or back flow happens. For a given organic liquid flow rate, a low aqueous phase flow rate fails to break up the organic phase, the aqueous flow surrounds the organic flow and flows coaxially through the contraction channel. A continued decrease of the aqueous flow rate can even cause a backward flow which pushes the aqueous phase flow backward. Similarly, increasing the aqueous flow rate beyond the stable flow rate will force the organic phase to flow backward. All these cases are undesirable for formulating stable microfluidic drops.

Beside the flow-rate ratio of the two phases, the geometry of the channels is an essential factor for drop formulation (Figure 2.4). In the stable drop stage (i.e. a reasonable flow ratio of the organic phase to aqueous phase), the organic drop size is strongly dependent on the junction width and is nearly proportional to the junction size when the flow rates remain constant. In our experiment, the drop size varies between 3 µm and 10 µm in a microfluidic chip with an 8-µm width junction; and the drop size is between 10 µm and 25 µm when the chip junction width is 17 µm. This phenomenon can be explained by two factors. First the junction width determines the initial width of the organic flow, and the corresponding pinch off point at which the finger of the organic flow will break up into drops if the wavelength of the dispersed phase is longer than its circumference. Second the junction area affects the local shear stress, as a smaller junction area results in a higher shear stress. As a result, the junction area of the microfluidic channel, together with the flow rate ratio, control the size of the droplets.

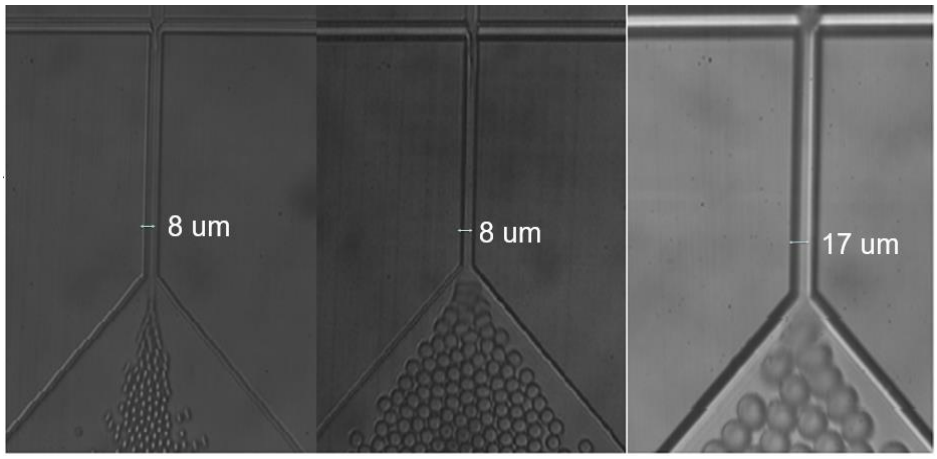

Figure 2.4. Micrographs showing the oil drops with different sizes: (a) about 5 µm (b) about 10 µm (c) about 20 µm.

2.2.2 Efforts to maintain a normal working conditions of the microfluidic system

First, pressure should be maintained at a reasonable range. Too high a pressure will burst the fittings between tubing and the syringe pumps or the microfluidic chip, or cause a leakage of liquid there. A low flow rate is also unwanted, as syringe pumps cannot precisely control such a low flow rate, for example, my syringe pump cannot handle a 5-ml syringe with a 10-mm inner diameter at a flow rate less than 0.06 µl/min. Besides, a low production of emulsion from the low flow rates is undesirable for research.

Second, blockage at the junction of the microfluidic channel must be avoided. Blockage prevents fluids running smoothly inside the channel, resulting in a random distribution of the drop size during formation process. A microfluidic chip with a junction in the micron scale can be easily blocked. Prevention is always better than cure. Both the liquids needed to be filtered by a 0.2-µm filter before flowing through the microfluidic system. However, even when large aggregates have been removed from the liquids after filtering, blockage is still prone to happen due to several reasons. One reason is back flow, which can occur either at the beginning or the end of the run of the syringe pumps. A dramatic pressure decrease at the inlet of the microfluidic channel makes a negative pressure difference inside the channel, which drives impurities from outside of the chip outlet to flow back and contaminate the whole channel, especially the junction region. This back flow can be eliminated by adding an in-line two-way valve in the tubing before the chip. It is always required to switch these off before starting or stopping the relevant syringe pumps. Another form of back flow is either a small portion of organic fluid entering the side channels or aqueous phase flow back to the central channel. I have observed when the non-aqueous solution of polystyrene enters the side channels and interacts with the aqueous phase, polystyrene tends to precipitate from the DCM solution and form into particles at the interface of these two phases, which generates large polystyrene particles blocking the side channels after the organic phase has been pushed back. Precipitation occurs because the DCM dissolves completely in the relatively large volume of aqueous phase in the side channels. However, when the aqueous phase passes through the non-aqueous phase and then flows back, the precipitation of polystyrene does not happen. Any polystyrene deposits forming at the oil/water interface redissolve in the following DCM solvent when normal flow in the central channel is established. Thus, any blockage is eliminated automatically in this case. Therefore, during the running of the fluids, it is required to ensure the aqueous phase

starts first before the organic phase, in order to avoid introducing the organic liquid into the side channels.

Third, a smooth continuous flow is required in the microfluidic system. The syringe pumps sometimes fail to provide a smooth flow as the stepper motor of the syringe pumps generates small fluctuations in the flow, which cause the flow regime to shift between the stable flow, back flow, and chaotic flow. These fluctuations are inevitable when using a syringe pump driven by a stepper motor and can be noticeable when using a small flow rate (less than 1 µl/min). Using a syringe with smaller diameters or increasing the flow rate can minimise this problem. An alternative way is to use microfluidic pressure pumps, which enable accurate control of pressure into microfluidic chips and provides pulseless liquid flow with controlled pressure and flow rates.

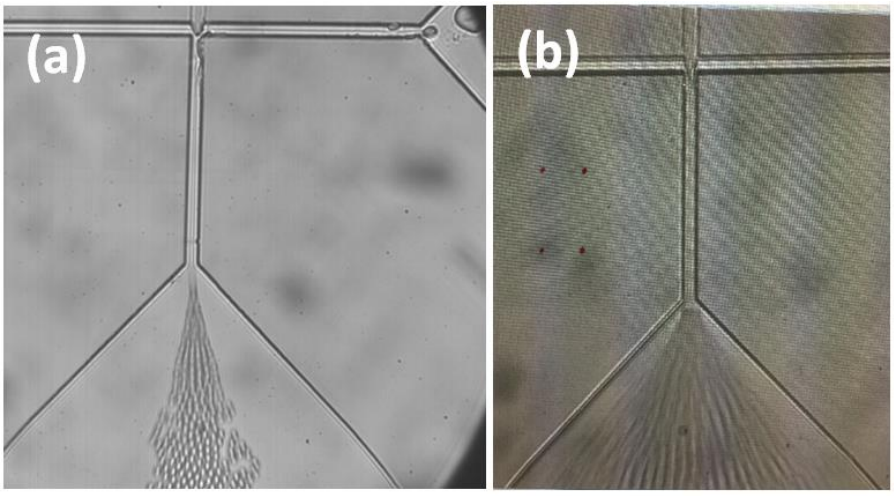

Figure 2.5. Micrographs showing (a) the blockage at the junction and right side channel, (b) generation of oil droplets at the junction at normal working conditions.

2.2.3 Methods to clean clogged microfluidic chips

The clogging of microchannels dramatically influences the production of emulsion droplets inside the microfluidic chip, thus decreasing the efficiency and lifetime of the microfluidic system. Though both the continuous phase and discrete phase have been independently filtered through 0.2-µm filters before entry into the microchannels, a certain amount of surfactant or polymer has been pre-dissolved in the corresponding solution, and may

precipitate at the interface of the oil and water phase, blocking the junction of the microchannels. Further aggregation of polymer or surfactant leads to a particulate larger than the junction size, preventing the flow of both phases and thus inducing a rapid increase of pressure inside the microfluidic system (see figure 2.5). Potential hazards are blasting the whole microfluidic system, damaging the syringe pumps, connection parts or microfluidic chips.

Once the microfluidic chips were blocked, it was very difficult to un-block them. The best way to address this problem is to avoid blockage in first place by periodically cleaning the entire channels. This can be done by flowing a mixture of pre-filtered acetone and DCM through the channels overnight after each experiment. In order to determine whether a cleaning procedure was required, the junction area of the device and its surroundings were visually inspected by the microscope. We should note that this cleaning method is not applicable to corrosive solvents, like sodium hydroxide, as these solvents will damage the special coating of the microfluidic device, like hydrophobic coatings.

However, when the clogging issues occur, the worst solution is to pump the liquid in the reverse direction as it may pull the polymer or surfactant from the outlet channel to the junction, reinforcing the blockage issues. The second thing to be avoided is pumping the liquid at a higher rate, as increasing the pressure is less likely to push the solid particulate out through the junction. Additionally, taking off the connections or stopping the syringe pump immediately is not correct, as may also induce the reverse flow from the outlet channel. To deal with the clogging issues effectively, there are three solutions. The first solution is to stop the oil phase and run the aqueous phase until all oil droplets containing polymers and surfactants flow out from the outlet port. Once there are no oil droplets inside the microfluidic chip, replace the aqueous phase with pure water to clear all surfactants from the microchannels, especially at the junction. Then pump pure organic solvent from the main channel in the forward direction to dissolve the polymers. As there is only pure organic solvent running inside the microchannels at this point, the clogging issues are solved. However, if the aqueous phase fails to run through the junction at the first step of the first solution, an alternative solution is to draw the liquids and particulates initially in the outlet channel out from the outlet port by a vacuum pump. Then pump pure water from the outlet port to the microfluidic chip and then replace the pure water with organic solvent to dissolve the aggregation at the junction. If the second solution also fails, a third solution is to draw the liquids from the inlet port and outlet port independently by the vacuum pump and

leave the microfluidic chip in an oven at 40^0C overnight. Then take turns to pump a mixture of acetone and DCM into each port at a constant rate of ~1 ml/h until the aggregate is removed. Moreover, to reduce the likelihood of blockage of the microfluidic chip during the cleaning process, all cleaning solutions including the pure water, organic solvent, and solvent mixtures should be filtered through 0.2-μm filters. After the cleaning process inside the microfluidic chip, take off the connectors and rinse the whole microfluidic system including the syringes, tubing, connectors, seals and microfluidic chips with pure water and DCM several times to ensure no particulate clogging in the microfluidics. Finally, store the microfluidics in a dust-free environment for next use.

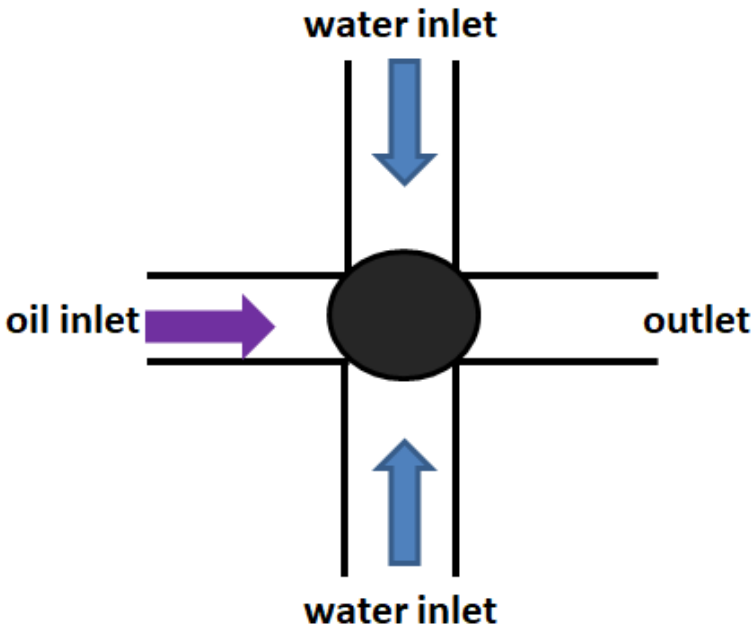

Figure 2.6. A schematic diagram showing the clogging of an aggregate of polymer and surfactant at the junction of the microfluidic chip.

To prepare the emulsions used in chapter 4, the experimental methods is illustrated as follows. Polymer (e.g., 1.0 wt% PMMA) and an involatile poor solvent (e.g. 1.0 wt% hexadecane) were dissolved in a volatile good solvent (e.g., DCM) to prepare the oil phase. PVA (e.g. 0.1-0.5 wt%) was dissolved in deionized water (Milli-Q) to produce the aqueous phase. The oil-in-water emulsions were either prepared by a homogenizer or microfluidics, giving rise to a polydisperse emulsion and a monodisperse emulsion respectively. For the former method, the aqueous phase (2 ml) and oil phase (1 ml) were mixed in a vial and emulsified by a homogenizer (T10 Ultra Turrax, IKA) with high-speed shearing (2–25.9k rpm)

for 1–30 sec using a homogenizer. The obtained emulsions were used as prepared. Depending on the shear force and shear time, the average size of generated oil droplets varied from 10 to 200 μm.

To produce the o/w emulsions in chapter 5, an aqueous solution of SDS (0.3 wt%) served as the continuous phase. Silica nanoparticles with acrylate surface (0.25 wt% or 1 wt%, 30 nm or 200 nm diameter) were well dispersed in DCM as the oil phase. The detailed information for generation monodisperse o/w emulsions by microfluidics is shown above. For the poly-disperse w/o emulsions used in chapter 5, the generation method is described as follows. SDS (0.3 wt%) was dissolved in deionized water (Milli-Q) to produce aqueous solutions, silica nanoparticles with plain surface (1 wt%) were dispersed in the aqueous solutions to produce a silica dispersion as the aqueous phase; 2-pentanol served as the continuous phase. 1 ml of aqueous solution and 3 ml of the 2-pentanol were mixed in a 10-ml vial and emulsified by a high-speed homogenizer (T10 ULTRA TURRAX, IKA; 25.9k rpm) for 30 s.

2.3 Modification of substrates

Glass cover slips (22×22 mm, thickness 0.13 mm, Academy Scientific) were loaded into a Teflon rack, soaked in 2 wt% alkaline detergent solution (Decon 90, Decon Laboratories) and sonicated for 15 minutes. Cover slips were individually rinsed with hot water and then ultra-high purity water for two minutes, dried in an oven at 100 ^{o}C for one hour and cleaned in an air plasma cleaner for half an hour. The cover slips were either used in this state as a hydrophilic substrate or they were coated with a hydrophobic layer by vapour deposition of a silane or silazane (e.g. CDMOS or HMDS) in a vacuum desiccator for two hours, thus forming a covalent -Si-O-Si- bond, rendering the substrate surface as water repelling (see figure 2.7). The treated coverslips were rinsed with acetone and then ultra-high purity water for two minutes and dried in an oven overnight. The typical contact angle is 20^{0} ($\pm 2^{0}$) and 64^{0} ($\pm 2^{0}$) for plasma-treated and HMDS-treated glass coverslips, respectively, which will be further investigated in section 2.5.

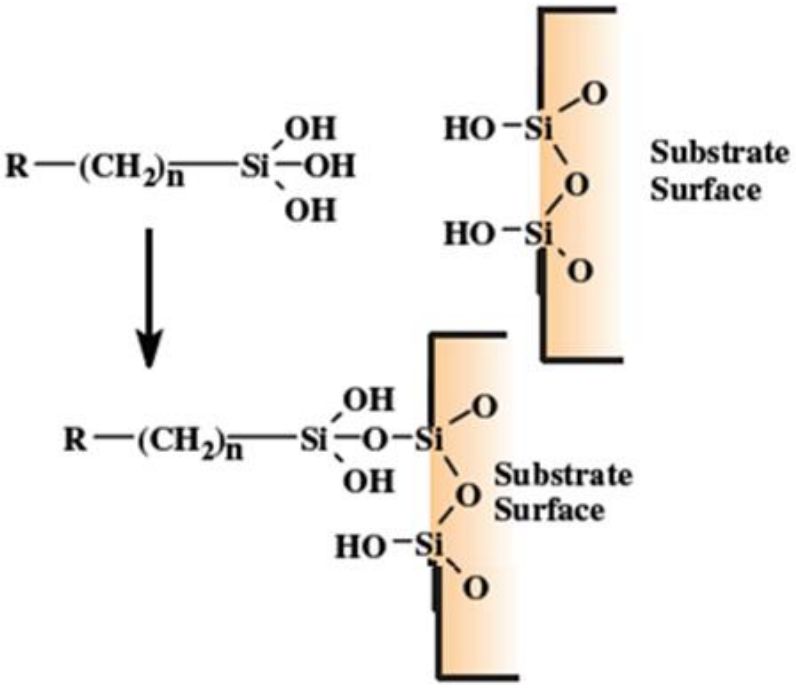

Figure 2.7. Schematic diagram of silanization of glass substrate to modify surface wettability, R is organic radical with functionality.

2.4 Ink-jet printing

The o/w emulsion was transferred from the microfluidic chip to the printing nozzle through FEP tubing (1/16" o.d. × 0.25 mm, Dolomite). The FEP tubing was divided into two sub-tubing (i.e. printing tube and waste tube) before entry into the printing nozzle, as the rate of generation of the emulsion is generally larger than that of printing of the emulsion. The length of the tubing for printing is approximately 20 cm in total. The residency time of the emulsion in the printing tube depends on the parameter of the printing tube (i.e. length and diameter) as well as the generation rate of the emulsion in the microfluidics. The ratio of the DCM droplets to the continuous phase is not well-defined due to issues with sedimentation of the DCM droplets in vertical parts of the tube. DCM is denser than water (density, ρ_{DCM} = 1.3266 g cm^{-3}) so the DCM droplets sink. The sedimentation rate, *v*, can be roughly estimated from Stokes' law (though this neglects interactions between droplets and the proximity of the tubing walls): $v = (\rho_{DCM} - \rho_{water})gd^2/18\mu_c$, where *g* is the acceleration due to gravity. For a 6-μm diameter droplet, $v \sim 6\ \mu m\ s^{-1}$. This is sufficiently fast that sedimentation occurs in the pipework connecting the microfluidic chip to the nozzle, so the volume fraction of oil in the emulsion is not well-controlled, but is generally

higher than that expected from the flow-rate ratios. Close coupling between the microfluidic chips, the connecting tubes and the inkjet printing nozzle could eliminate these issues. Moreover, using an organic solvent with a density similar to that of the continuous phase can also reduce the sedimentation issues.

The nozzle for inkjet printing was mounted to a Microfab drop-on-demand device (MJ-ABP-01, Microfab Technologies; 50 or 80- μm diameter orifice) controlled by a Microfab driver unit (Microfab JetDrive III controller CT-M3-02). Emulsion drops (typical volume 150 - 250 pL) were generated with a bipolar waveform of ± 40 - 50 V and were ejected from the nozzle orifice at a velocity of ~1 m s^{-1} onto the substrate. The printed drops dried freely under ambient conditions at 21–23 °C and relative humidity of 30– 35 %. For experiments at high humidity (85–90%), a humidity chamber was used. The evaporation process on the substrate was recorded from below by a high-speed camera (Photron APX RS) at 250 fps with an exposure time of 4 ms. The side profile of the drying drops was captured by a high-speed camera (Optronis) at 250 fps with an exposure time of 4 ms. For all the experiments performed in this thesis, an array of more than 100 printed droplets were produced continuously and formed structural patterns on the pre-treated substrates under certain conditions (i.e. surrounding humidity and temperature), and typical patterns of the deposits were then picked out and analyzed.

During the emulsion generation process, the DCM solution of polystyrene is captured into discrete monodisperse drops inside the aqueous phase. This oil-in-water emulsion is then transferred to a DOD Microfab nozzle and is used as ink for the following ink-jet printing process. Ink drops are generated by a pressure pulse through a voltage waveform. The waveform is adjusted to eject stable drops with a velocity of about 1 m s^{-1} without satellite drops. Similar to the formation of discrete organic drops inside the microfluidic system, the formation of ink drops is also controlled by two competing effects, the elongation and deformation of ink liquid by shear stress, and the resistance to deformation by the capillary pressure. The capillary pressure is the pressure difference at the interface between the aqueous solution and the air below the nozzle orifice. As for the shear stress, when the emulsion liquid is forced to pass through the nozzle, the fluid moves more quickly near the axis of the nozzle and moves more slowly near its wall. Therefore the approximate shear rate near the nozzle orifice is $\dot{\gamma} = \frac{v}{R_n} \sim \frac{1m/s}{40um} \sim 2500\mathrm{s}^{-1}$, where R_n represents the radius of the nozzle orifice. The corresponding shear stress can be estimated as $\tau \sim \mu\dot{\gamma} \sim 8.9 \times 10^{-4}\ \mathrm{Pa\ s} \times 2500\ \mathrm{s}^{-1} \sim 2\ \mathrm{Pa}$, where μ is the viscosity of water.

As the capillary pressure is fixed in our experiment, the shear stress should be adjusted at a reasonable range. Below the range, a low shear stress fails to deform the interface, and results in no ink drops. Beyond the range, a relatively high shear stress not only enables deformation of ink drops, but also generates coalescence or breakup of internal oil drops due to high shear force applied on single internal drops. In the coalescence process, two or more internal oil drops merge to form single large oil drops. In the breakup process, a single internal drop breaks into two or more new daughter drops. Both processes are unwanted, as these polydisperse oil drops will result in an uneven distribution of polystyrene particles after drying. Therefore, the shear stress should be adjusted in a stable range to pinch off the ink drops without excessive deformation of the internal oil drops. Droplet deformation is a competition between the shear stress and the Laplace pressure, $2\gamma_{\mathrm{ow}}/R$. So a low interfacial tension, which may be good for stabilizing the emulsion, is bad for droplet breakup – another reason for minimizing the concentration of surfactant.

In order to eliminate this problem, there are two ways to stabilize the internal drops during inkjet printing. One way is to use a nozzle with a relatively larger diameter. Assuming the impact velocity of the jetted drops is fixed, increasing the nozzle diameter reduces the shear rate as well as the corresponding shear stress. Figure 2.8 compares the behaviour of internal oil drops using nozzles with two different diameters (50 µm, 80 µm). Polystyrene particles with uniform size are observed after jetted from an 80 µm-nozzle, while particles with a wide distribution of sizes are observed in a 50-µm nozzle. This comparison shows the magnitude of shear force affects the stability of the internal drops significantly.

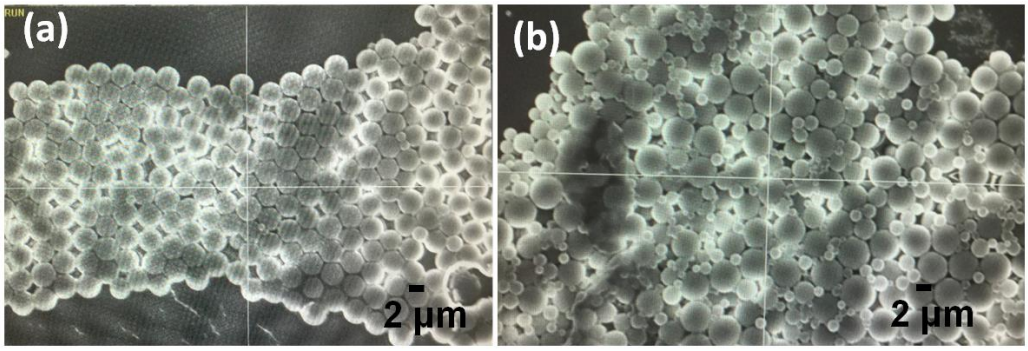

Figure 2.8. SEM images of the deposit from emulsions printed by an 80-µm nozzle (a) and a 50-µm nozzle (b). The size of the particles in (a) is 2.1 $\pm$ 0.1 µm, and that in (b) is in the range of 0.2-3.5 µm.

The other way is to reduce the size of the internal oil drops. Although the shear force near the nozzle orifice does not change, the total shear force applied on a single oil drop reduces due to a smaller surface area. Figure 2.9 shows a comparison of the behaviour of the internal oil drops with two different sizes (18 μm, 8 μm). Figure 2.9a shows nearly a half of the polystyrene particles have a diameter less than 1 μm, which is much smaller than the normal diameter (3 μm) indicating that the emulsion droplets have broken up during the jetting process. In Figure 2.9b, all the particles have a uniform size (1 μm). This demonstrates that decreasing the initial oil drop size is an efficient way to stabilize the drops.

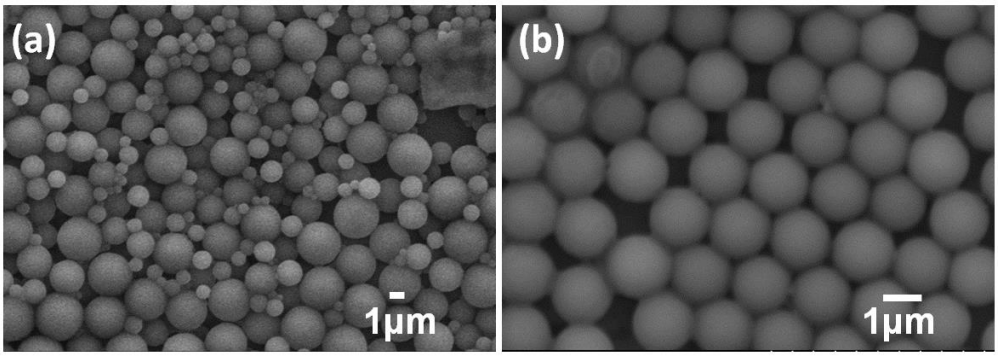

Figure 2.9. SEM images of the deposit from ink droplets with large oil drops (18 μm) and small oil drops (8 μm). (a) Particles are less uniform with diameters from submicron to 2.5 μm. (b) Particles are more uniform with diameter of 1 (± 0.05) μm.

2.5 Analysis of fluid properties

The contact angle of emulsion drops and the interfacial tension between the oil and water phase were measured by the sessile drop and pendant drop methods, respectively (FTÅ200, First Ten Ångstroms); each reported value was an average of at least five independent measurements. Figure 2.10 [16] shows the contact angles of different solvents: (a) water, (b) 0.3 wt.% SDS aqueous solution, and (c) emulsion on substrates on substrates treated by (1) OTS, (2) CDMOS, (3) HMDS and (4) plasma treatment alone. The contact angles of individual droplets are obtained by analysing the profiles of the sessile droplets from a side-view high-speed camera.

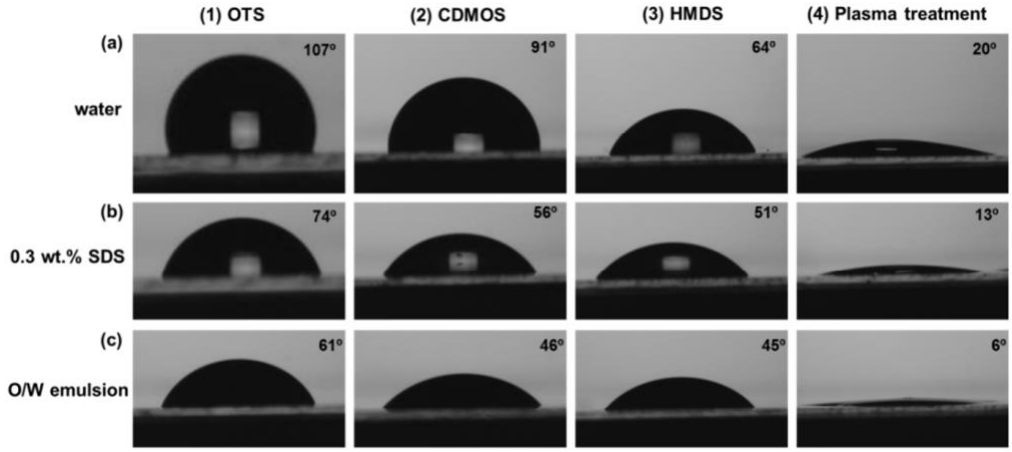

Figure 2.10. Images of the contact angles of different solvents: (a) water, (b) 0.3 wt.% SDS aqueous solution, and (c) emulsion on substrates on substrates treated by (1) OTS, (2) CDMOS, (3) HMDS and (4) plasma treatment alone. (Reprinted (adapted) with permission from ref [16]. Copyright {2018} American Chemical Society).

2.6 Post-deposition analysis methods (SEM, EDX)

Coverslips with dried deposits of microparticles were investigated by a scanning electron microscope (Hitachi SU70 FEG SEM) to determine the morphology of the deposits and the microparticles. The coverslips with samples were sputtered with a conductive film of gold (10–30 nm) to ensure conduction through the sample and then imaged by SEM at an acceleration voltage of 5–10 KV.

The scanning electron microscope (SEM) is a useful tool to investigate the surface topography and composition of the microparticles. It can achieve a lateral resolution less than 1 nm, and a wide range of magnification ranging from about 10× to 500,000×, which is two orders of magnitude higher than the light microscope (see figure 2.11). The principle of SEM is to utilise a focused electron beam scanning over the surface of the sample, where the electrons interact with the atoms of the sample and produce various signals about the morphology of the samples and elemental composition.

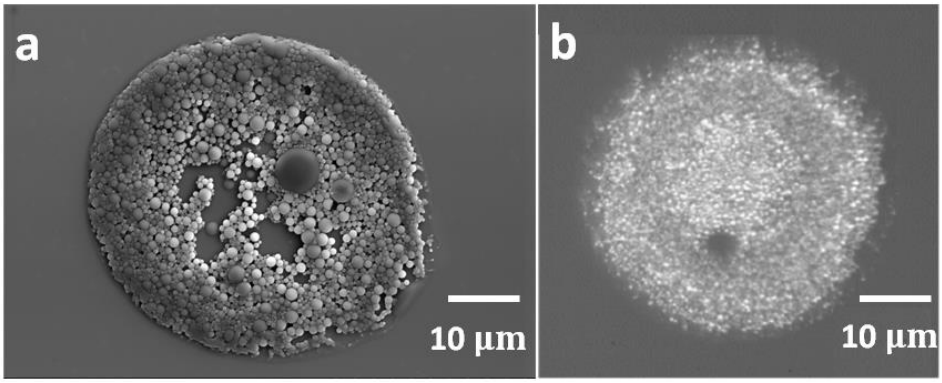

Figure 2.11. A comparison between SEM image (a) and light microscope image (b) of a circular deposit with micron-sized particles on a glass coverslip.

There are several primary operational processes in the SEM, including vacuum, beam generation and manipulation, beam interaction and detection, signal processing and record, as is shown in figure 2.12.

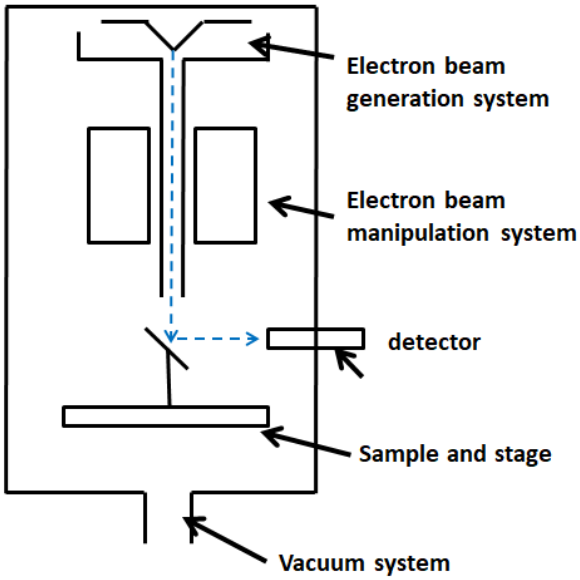

Figure 2.12. Diagrams showing the major operation systems in the SEM column and chamber. The blue lines indicate the primary beam electrons and scattering events.

The vacuum is required for operating electron beams as electrons will scatter due to collisions with other molecules in the column of the SEM. A vacuum environment in the

column of the SEM can be obtained by extracting as many molecules as possible. The background gas pressure needs to below $10^{-4} - 10^{-6}$ Torr to operate. If there are any molecules existing in the operational chamber, the shelf life of the filament will be reduced dramatically. Thus when loading specimens to the SEM, the filament and the entire operation chamber must be isolated from atmospheric pressure by valves.

The beam generation and manipulation system is mounted at the top of the SEM column, where the electron beam is generated and manipulated to scan over the surface of the sample. The electron gun can generate illuminating electron beams (also named primary electron beams) at a wide range of voltages from 0.1 to 40 kilovolts (kV). In general, increasing the voltage will result in a higher resolution and greater amount of heat on the surface of the sample. A lower voltage below 10 kV is suitable for delicate samples, like biological samples. After the generation of the electron beams, the electrons pass through the manipulation system consisting of electromagnetic lens and coils. The magnetic field deflects the electrons and allows scanning over sample surface in both X and Y directions (i.e. a raster fashion). In principle, lowering the dimension of the scanning area contributes to a higher magnification.

For the beam interaction system, when the primary beam electron hits the particles within the sample, it will travel with a different trajectory, called scattering. Based on different scattering events, there are backscattered electrons (BE), secondary electrons (SE), X-rays, etc. Backscattered electrons originate from some primary beam electrons that escape back from the specimen but do not go through the sample surface. As the backscattered electrons are from the primary beam electrons, they contain a high level of energy, which is of the same order of the primary beam electrons. Secondary electrons are the most commonly used scattering event in the SEM, and generate when the primary electrons displace the electron of the sample surface. As the secondary electrons have a very low energy level with a few electron volts, the detection of secondary electrons can only occur at a shallow depth from the specimen surface. X-rays are generated when the primary beam electrons remove an inner shell electron of an atom of the sample. Valence electrons then drop down into the vacancy releasing their energy as an X-ray or as an Auger electron. Typically, light elements emit Auger electrons and heavy elements emit X-rays. As the X-rays contain a characteristic wavelength and energy level of the atom from which the scattering occurred, X-rays can be used to identify elemental composition and distribution among samples. Based on the categories of detectors, there are two main spectrometers:

wavelength dispersive spectrometer (WDS) and energy dispersive spectrometer (EDS). This thesis utilizes EDS to investigate the chemical composition and distribution of micron-sized particles.

To explore the internal structures of the microcapsule, focused ion beam (FIB) milling of the samples was performed in a FIB/scanning electron microscope dual beam system (FEI Helios NanoLab 600). Dry deposit was embedded in a platinum protection layer with a film thickness of 3 µm. Larger beam currents quickly milled away sections of material from the sample surface, while lower currents were used for polishing the milled surface.

2.7 MATLAB Image Processing

Individual polymer particles were detected in the SEM images using the built-in Matlab function for the circle Hough transform, from which I calculated the size distribution and the coefficient of variation (defined as $CV = \frac{1}{d^*} \times \left[\frac{1}{n-1}\sum_{i=1}^{n}(d_i - d^*)^2\right]^{1/2} \times 100\%$, where d_i is the measured particle diameter, d^* is the mean diameter, and *n* is the number of particles analysed). By adjusting the contrast between the polymeric particles and the surrounding backgrounds, an optimum capture of the particle peripheries using circles are achieved. First the size of each pixel is obtained by contrasting with a reference length which in the SEM image is the scale bar, then the particle size is obtained by calculating the pixel numbers of each captured circle in the image. Chapter 3 will show how the Matlab program works to detect the spherical particles and calculate the size distribution.

2.8 Construction of ternary phase diagram (by nuclear magnetic resonance spectroscopy)

The ternary phase diagram for DCM/PMMA/HD system was constructed by mixing a pre-weighed amount of each material in a NMR sampling tube with a 4.2-mm inner diameter. The amount of PMMA was fixed at 0.05 g, HD remained at either 0.1 g or 0.15 g, while DCM varied in a range of 0.1–0.5 g to obtain different compositions within the phase diagram. PMMA was first dissolved in DCM and treated with 40^0C water bath for 1 hour to ensure a complete dissolution of polymer. HD was subsequently added, the sample was shaken by hand for at least 50 times to homogenize the mixture. The cloudy mixture of DCM/PMMA/HD was allowed to phase separate at ambient conditions for 1 hour until two

distinct separated layers (i.e. a PMMA-rich phase and a HD-rich phase) with a fixed boundary line was formed. Each layer was transferred to a different NMR tube with sufficient $CDCl_3$ by a gas-tight syringe. The prepared samples were immediately sent for NMR measurements. During sample preparation process, the NMR tube remained sealed by a cap, except for the adding of material or transferring of solutions, to avoid the loss of low-boiling solvent.

1H-NMR spectra were collected using a Varian VNMRS-600 spectrometer with operating frequencies of 599.42 MHz for 1H. Vibration problems during NMR measurements were optimised to minimise the fluctuations in the NMR spectrum. Integration of proton NMR spectra corresponding to DCM, PMMA or hexadecane was calculated respectively and compared to each other to determine their relative ratios in the different phases, as will be shown in figure 4.7. The compositions of PMMA-rich phase and HD-rich phase on the binodal of the ternary phase diagram were established and a binodal curve was obtained by fitting the experimental data.

As the composition approaches the critical point, it is challenging for phase separation as the composition difference of the two phases is less obvious. The decreasing interfacial tension slows down the phase separation process. Hence the critical point obtained in the ternary phase diagram is just an estimation of the extremum point on the fitted binodal curves. The solution viscosity depends predominantly on the polymer concentration. I experimentally observed that when the DCM concentration is below 50 wt%, a solution-to-gel transition occurs in the NMR tube due to the increased viscosity, which freezes the motion of molecules and thus suppresses the phase separation. The ternary phase diagram only provides information for DCM above 50 wt%.

2.9 Reproducibility of the experimental data

To ensure the reproducibility of my experimental results between different experiments, processing parameters are maintained as constant as possible. For the generation of the oil-in-water emulsions, the size of the oil droplets are recorded by a high speed camera at the flow-focusing junction of the microfluidic chip. To ensure the monodispersity of the emulsions, the ratio of the oil to aqueous phase are fixed at 1:10, except for the case of studying the effect of variations of the oil droplet size. The oil droplet size and resultant polymeric size are monitored during each experiment, the uniformity are the key factors to guarantee reproducible experimental data. For the inkjet printing process, the nozzle orifice remained constant at 80 microns and the bipolar wave were kept constant to jet continuous

arrays of droplets without satellites. The reproducibility during inkjet printing process can be verified by measuring the initial diameters of the printed droplets on the underlying substrates. If a significant variations of the initial diameter occurs, either satellites or nozzle clogging occurs, indicating the reproducibility of the experimental data is not ideal. For the underlying substrates, the plasma-treated glass coverslips were used just after modification, to avoid the degradation of the hydrophilicity with time; the hydrophobic glass coverslips were treated by vapour deposition with same amount of time to achieve a constant surface energy. The reproducibility of underlying glass coverslip can be estimated by measuring the contact angle of pure water before each experiments. The small fluctuations of humidity (±10%) and temperatures ($\pm 5^0$) played minor effects on the experimental data, which will be shown in later chapters.

3 Fabrication of monolayers of uniform polymeric particles by inkjet printing of monodisperse emulsions produced by microfluidics

Abstract

Emulsion solvent evaporation is a well-established method for generating microparticles from solutions of polymers in volatile organic solvents dispersed in an aqueous medium. Previous work has shown that this approach can also be used to deposit particles by inkjet printing where the particles are formed during the drying of a liquid ink on a substrate. The particle size distribution, however, was very broad. Here I demonstrate that inkjet printing of oil-in-water emulsions produced by microfluidics can generate micron-sized particles with a narrow size distribution (coefficient of variation <6%) and that these particles can self-assemble into ordered arrays with hexagonal packing. The conditions under which drops can be printed with a minimum of break up and coalescence of the oil droplets in the emulsion are explored. Factors affecting the size of the particles and the morphology of the deposit are described. This study uses polystyrene in dichloromethane as a model system, but the approach can be generalized to the production of structured and functional particles.

3.1 Introduction

Emulsion solvent evaporation is a well-established method for producing microparticles [32-35]. In this approach, polymers and other non-volatile components are dissolved in the discrete phase of an oil-in-water (o/w) emulsion. The non-polar solvent is chosen to be more volatile than the continuous aqueous phase so that the droplets evaporate before the continuous phase to produce discrete particles. Depending on the solutes employed and

their phase behaviour, a wide variety of different morphologies can result.

In a previous paper [16], we have shown that emulsion solvent evaporation can be coupled with inkjet printing to fabricate microparticles of polymers on a surface. The emulsion 'ink' is in the liquid phase and the particles are only generated during the drying process. This approach avoids problems of jetting of inks with micron-sized particles, including blocking of nozzles and variability in the direction of jetting. It also avoids formulation stability issues, such as aggregation and settling of particles. Our previous work used emulsions produced in a homogenizer, which generated a wide range of oil droplet sizes and hence a wide range of particle sizes from sub-micron up to a few microns. The purpose of this chapter is to show that the same approach can be used with monodisperse emulsions produced in a microfluidic chip and that these emulsions can be printed with only a small amount of degradation in the size distribution of the oil droplets, thus yielding particles with a narrow distribution of sizes. Coupling of the microfluidic chip to the inkjet nozzle can reduce the time between generation and printing of the emulsion and thus minimise stability issues with the emulsion, such as Ostwald ripening or coalescence.

Our model system comprises polystyrene (PS) dissolved in dichloromethane (DCM) as the oil phase and aqueous solutions of sodium dodecyl sulfate (SDS) as the continuous phase. The SDS stabilises the emulsion before printing. Inkjet printing has previously been used to fabricate patterns of colloidal particles via evaporation-induced self-assembly (EISA) of particulate inks drying on a substrate [36-42]. If the particles size is right (hundreds of nm), these patterns can exhibit structural colour, so-called colloidal photonic crystals, which can be used for applications in sensors and displays [43-48]. We can therefore compare the patterns formed by emulsion solvent evaporation of liquids with those from the printing of particulate inks.

Evaporation of a bulk dispersion of colloidal particles on a substrate can generate a 2D film of colloidal crystals [49-51]. It is a challenge to design desired patterns unless templates are used [36, 52]. Evaporation of drops of a colloidal dispersion can form spheres/dots of colloidal crystals [34, 53-56]. The drops can be deposited onto substrates to form desired patterns (arrays of dots, lines and large-scale patterns) via inkjet printing [57-60]. Compared to templated assembly, inkjet printing offers the advantages of digital control over patterns, uses less material, allows precise positioning of deposits, is applicable to flexible substrates and is easier to scale-up.

In this chapter, I first show that o/w emulsions containing PS/DCM droplets produced in a flow-focussing junction evaporate in a cast film and form monodisperse particles that self-assemble into an ordered hexagonal array. I then show that these same emulsions can be printed successfully to produce dry deposits with a narrow particle size distribution. I discuss how the physics of drying influences this process. The conditions are optimised to minimise the amount of break up and coalescence of droplets during the jetting process and hence to produce particles with a narrow size distribution. Variation in the droplet size and polymer concentration can be used to control the final particle size. I explore the conditions necessary to obtain dense monolayer deposits of both small (~1 μm diameter) and larger (2–3 μm diameter) particles. Finally, I discuss the prospects for manufacturing more complex functional particles by inkjet printing of emulsions and the limitations of the approach.

3.2 Results and Discussion

3.2.1. Preparation of monodisperse emulsion droplets by microfluidics

Droplet microfluidics is an efficient method for preparation of monodisperse emulsion droplets [61-63]. Figure 3.1a shows a set of images recording the formation of oil drops in the flow-focussing junction, as discussed in chapter 2, the oil flow enters through the channel at the left and the water through the channels at the top and the bottom. Droplet formation is governed by a competition between the deformation of the o/w interface achieved by viscous shear and the resistance of the interface to deformation arising from surface tension. The transition from the dripping to the jetting regime is determined by the capillary numbers of both the continuous and disperse phases [64], and within the dripping regime, the flow-rate ratio Q_o/Q_w determines the size of the drop. Stable monodisperse oil droplets were observed for varying flow rate ratios and polymer concentrations. I fixed the aqueous flow rate, Q_w at 2 μl /min and varied the oil flow rate, Q_o. When Q_o/Q_w increased from 0.1 to 0.5, the diameter of oil droplets increased from around 6 to 12 μm (Figure 3.1b$_1$ and 3.1b$_2$). When Q_o/Q_w was > 0.5 or < 0.1, backflow of the water or oil phase took place and no oil droplets formed. The polymer concentration had only a small influence on droplet size in the range of concentrations 0.5–5 wt% because drop size depends weakly on viscosity of oil phase.

The emulsions were cast onto clean substrates and allowed to dry slowly, forming a continuous monolayer of well-ordered, hexagonally packed polystyrene particles (Figure 3.1c), as has been observed previously in EISA of pre-formed colloidal suspensions. The

particle size depends on both the oil droplet size and the PS concentration: the polystyrene particles were spherical and of uniform size with diameters of 1.04±0.02 µm, 2.2±0.05 µm, and 2.02±0.05 µm for the samples in Figures 3.1c_1, 3.1c_2 and 3.1c_3, respectively. The particle size distributions are shown in Figure 3.2. The coefficient of variation in the particle size distribution was less than 2.5%.

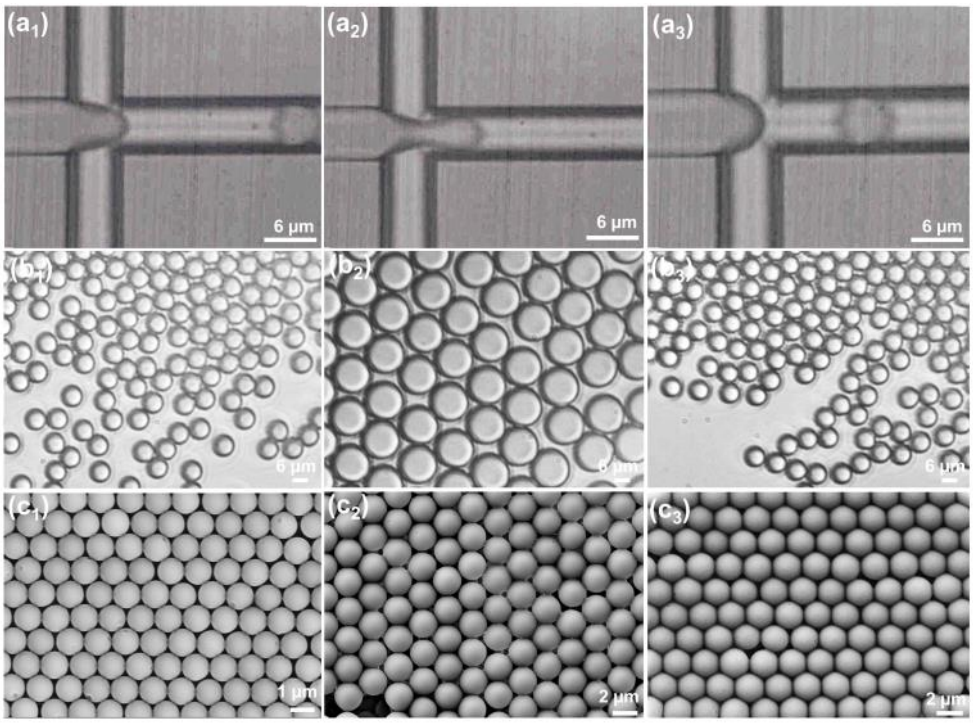

Figure 3.1. (a) Images showing o/w droplet production in the flow-focusing junction of the microfluidic chip; (b) Images of monodisperse emulsions produced from a continuous phase of 0.5 wt% SDS in water and a discrete phase comprising (b_1) 0.5 wt%, (b_2) 0.5 wt%, and (b_3) 5 wt% polystyrene in DCM. The flow rate of water phase was constant at 2 µL/min, the flow rate of oil phase was (b_1) 0.4 µL/min, (b_2) 1 µL/min, and (b_3) 0.4 µL/min. (c) SEM images of deposits with polystyrene particles from corresponding emulsions after free drying of a film cast on a clean glass coverslip.

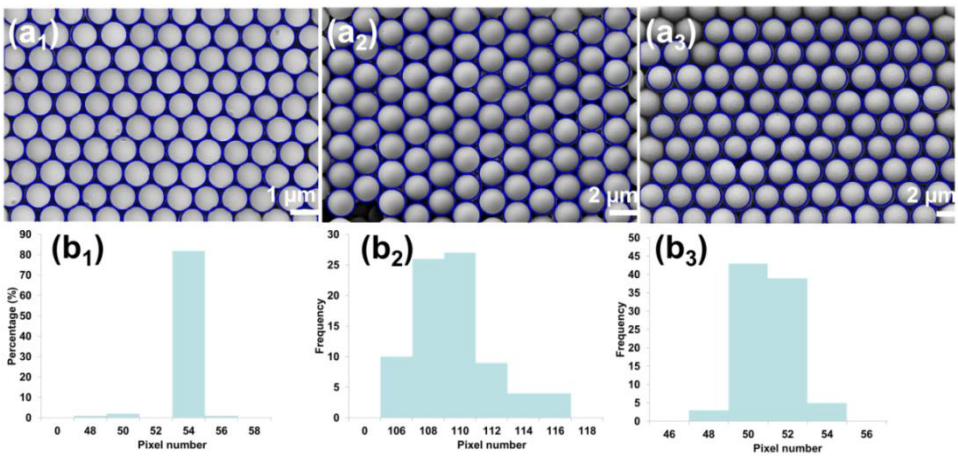

Figure 3.2. (a) Detected circles of individual particles from the samples in Figures 3.1c$_1$, 3.1c$_2$ and 3.1c$_3$, (b) histograms of pixel number from corresponding images, the particle diameter equals to 2×pixel number×resolution. As the function " imfindcircles" in Matlab is limited to integer-level precision, the detected radius is discontinuous.

3.2.2. Inkjet printing of monodisperse emulsions

Emulsion drops were printed continuously at 1 Hz through an 80-µm nozzle onto a plasma-treated glass coverslip with $\theta_{H_2O} = 20^0$. A nozzle with a large orifice was chosen to minimise the shear stress on the oil droplets. The deformation of an oil droplet in a shear flow is, to a good approximation, equal to the capillary number, $Ca = \frac{\mu_c \dot{\gamma} d}{\sigma}$, where μ_c is the viscosity of the continuous phase, $\dot{\gamma}$ the shear rate, *d* the droplet diameter and σ the interfacial tension [66]. Reducing the droplet deformation decreases the likelihood of break-up of the droplets during jetting.

Figure 3.3 shows images extracted from videos (see video links in chapter 8.3) that illustrate three distinct stages of the evaporation process. To understand what we see in these images we need to consider two factors. First, the oil is denser than water (density, ρ_{DCM} = 1.3266 g cm^{-3}) [67] so the droplets sink. The sedimentation rate, *v*, can be roughly estimated from Stokes' law (though this neglects interactions between droplets and the proximity of the substrate): $v = (\rho_{DCM} - \rho_{water})gd^2/18\mu_c$, where g is the acceleration due to gravity. For a 6-µm diameter droplet, $v \sim 6\ \mu m\ s^{-1}$. This is sufficiently fast that sedimentation occurs in the pipework connecting the microfluidic chip to the nozzle, so the volume fraction of oil in the emulsion is not well-controlled, but is generally higher than that expected from the flow-rate ratios. The typical drying time of the DCM droplets is ~1 s and the typical height

of a droplet at the apex is ~15-20 μm. Consequently, while some sedimentation does occur during drying, there is insufficient time for 6-μm droplets to settle to the bottom of the printed drop under gravity. The Peclet number is also large so Brownian diffusion does not homogenise the oil droplet distribution vertically or horizontally, though it may play a role in annealing of local defects in the deposit.

Second, although DCM is much more volatile than water (vapour pressure at 293 K, p_v = 46 kPa for DCM and 2.34 kPa for water, see Table 3.1), which solvent evaporates faster depends on the rate-limiting step in the mass transport of the DCM: diffusion in the aqueous phase or diffusion in the gas phase. To get a better understanding of the evaporation process I consider a simple mass transport model for DCM escaping from a layer of DCM droplets a distance δ below the air–water interface in a sessile emulsion drop of radius R and a contact angle θ. The average evaporative flux, $J_{ave,}$ in the vapour phase is given approximately by [68]

$$J_{ave} = \frac{D_{vap}}{R} c_s(v)(0.27\theta^2 + 1.30), \tag{3.1}$$

where $c_s(v)$ is the concentration of DCM vapour at the surface of the printed droplet, and D_{vap} = 1.08 × 10^{-5} m^2 s^{-1} is the diffusion coefficient of DCM in air [67]. For small θ, we can ignore the first term in brackets and

$$J_{ave} = \frac{1.3 D_{vap}}{R} c_s(v). \tag{3.2}$$

Assuming that Henry's Law is valid,

$$\frac{c_s(v)}{c_0(v)} = \frac{c_s(l)}{c_0(l)}, \tag{3.3}$$

where $c_s(l)$ is the concentration of DCM in the liquid (aqueous) phase at the surface and c_0(l) and $c_0(v)$ are the saturation concentrations of DCM in the liquid (~2% by weight) and vapour phases. It is reasonable to assume that the water right next to the DCM droplets is saturated in DCM, i.e. the DCM concentration is $c_0(l)$. The DCM from the emulsion droplets has to diffuse through a thickness δ of water between the emulsion droplet and the air/water interface of the drop. From Fick's first law, the flux of DCM in the liquid is

$$J = \frac{D_{liq}(c_0(l) - c_s(l))}{\delta}, \tag{3.4}$$

where D_{liq} = 1.17 × 10^{-9} m^2 s^{-1} is the diffusion coefficient of DCM in water [67]. If we neglect the motion of the interface, the flux of DCM into the interface from the liquid side has to balance the flux of DCM out of the interface from the vapour side, so

$$\frac{D_{liq}(c_0(l)-c_s(l))}{\delta} = \frac{1.3D_{vap}}{R} c_s(v), \quad (3.5)$$

Using Henry's Law, we can eliminate $c_s(v)$ to obtain

$$\frac{D_{liq}(c_0(l)-c_s(l))}{\delta} = \frac{1.3D_{vap}}{R} \frac{c_s(l)c_0(v)}{c_0(l)} \quad (3.6)$$

Substituting, $D_{vap}/D_{lip} = 9.23 \times 10^3$ and $c_0(v)/c_0(l) = 0.080$ into eq.(3.6) and rearranging gives

$$\frac{(c_0(l)-c_s(l))}{c_s(l)} \approx 10^3 \frac{\delta}{R} \quad (3.7)$$

As an example, if we take the radius of the sessile drop to be R = 100 μm, and the contact angle to be θ = 20°, the height of the drop would be 17 μm. If we then had a 6-μm droplet sitting at the bottom of the ink drop, it would be about δ = 10 μm from the surface. With $\delta/R = 0.1$, we have $(c_0(l) - c_s(l))/c_s(l) = 10^2$, so the concentration of DCM just below the free liquid–vapour interface would be only 1% of its saturated value. Here the evaporation rate is dominated by mass transport in the aqueous phase. The consequence, however, is that the vapour pressure is only 1% of the saturated vapour pressure (~0.5 kPa) which is less than the vapour pressure of water. So the water will evaporate faster than the DCM except at very high relative humidities (RH). Near the edge of the drop, however, the thickness of the water film between the DCM droplets and the drop surface is much less – say 1 μm. Now, $(c_0(l) - c_s(l))/c_s(l) = 10$. Mass transport is still limited by diffusion through the bulk phase, but now the vapour pressure is about 10% of the saturated vapour pressure of DCM (4.6 kPa). The evaporation rate depends on the product of the vapour pressure and the vapour diffusivity (which is 2.3 times higher for water vapour than DCM), so in this example DCM would evaporate faster than water at ambient relative humidity. As the aqueous phase evaporates, the height of the droplet decreases and hence so does δ. Thus even in the centre of the drop, there will come a time when the DCM evaporates faster than the aqueous phase so the prerequisite for the emulsion solvent evaporation method to work – namely that the discrete phase evaporates before the continuous phase – is still

satisfied. For completeness, I note that near the end of the evaporation of the oil droplets, the DCM concentration in the droplets falls quickly and so does its chemical potential. This reduces $c_0(l)$ and hence slows down mass transport. 'Sticky' particles containing residual DCM are undesirable since they will tend to adhere and deform rather than form mobile arrays in which defects can anneal during drying.

Turning back to Figure 3.3(a_1), I observe emulsion droplets throughout the droplet just after printing (see video link in chapter 8.3). The droplets near the edges are in focus (i.e. near the substrate) while those in the centre are out of focus indicating that they are distributed through the volume of the drop. Even at a very early stage, the droplets near the contact line are smaller than those nearer the centre due to the fact that the evaporation rate is much faster near the contact line (J diverges as $(1-(r/R)^2)^{-1/2}$; eq. (1) is just the average evaporation rate over the droplet. In Figure 3.3(a_2), a layer of particles has formed near to the contact line while oil droplets are still observed near the centre, due to the height-dependence of the mass transport described above. Note that the particles are excluded from a region very near the contact line, where the height of the droplet (which is still a spherical cap) is less than the particle diameter. Particles in this region deform the liquid-vapour interface, which is energetically unfavourable. Since the particles are mobile this capillary force pushes the particles towards the apex of the drop. In Figure 3.3a_3, the oil droplets have all formed solid particles, but the number density is such that the inward capillary force is opposed by inter-particle repulsions: a uniform densely packed layer of particles is formed which defines the height of the drop. Finally, Figure 3.3a_4, show the particle distribution after the last of the aqueous phase has dried. In general, I observe that the size of the circular deposit is smaller than that of the initial contact line due to the inward capillary forces on the particles during drying (from 116 µm to 88 µm in diameter in this example).

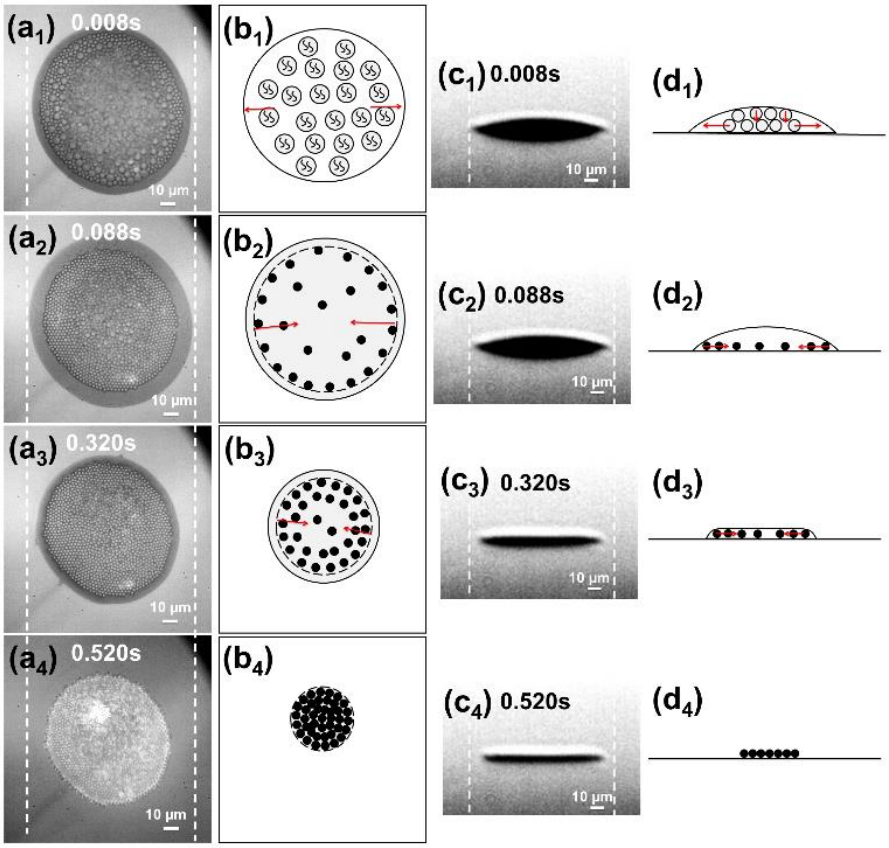

Figure 3.3. (a) Bottom-view optical microscopy images and (b) corresponding schematic graphs showing the evolution of a printed emulsion droplet (66.5 mg mL^{-1} PS/DCM dispersed in 1.0 mg mL^{-1} SDS/water) with 6-μm oil drops on a plasma-treated glass cover slip. The objective is focussed near the substrate. (c) Side-view images and (d) schematic diagrams of the variations of the droplet profile. The white dashed lines in (a) and (c) indicate the maximum extent of the contact line after spreading of the emulsion droplet. The red arrows in (b) and (d) show the direction of motion of the oil drops or particles during the evaporation process.

Table 3.1. Properties of DCM and water at 20 °C.

DCM solubility in water	$c_0(l)$ = 0.235 M
Saturated DCM vapour pressure	p_v = 46 kPa
Water vapour pressure	$p_{v(water)}$ = 2.34 kPa
Saturated DCM concentration in air	$c_0(v) = p_v/RT$ = 0.0189 M
DCM density	ρ_{DCM}= 1.3266 g cm^{-3}
0.1wt% SDS aqueous phase viscosity	η = 0.001 Pa s
Diffusion coefficient of DCM vapour in air	$D_{vap(DCM)}$ = 1.037 $\times$ 10^{-5} m^2 s^{-1}
Diffusion coefficient of water in air	$D_{vap(water)}$ = 2.42 $\times$ 10^{-5} m^2 s^{-1}

The dry deposits were analysed by scanning electron microscopy (SEM). Figure 3.4 shows a typical SEM image for a particle deposit from a 5 wt% PS/DCM oil phase. The range of particle diameters in this deposit is 2.212–2.686 μm, with a few much smaller particles (< 1 μm) which probably originate from satellites formed during the break-up of the primary emulsion droplets. The particles have a mean diameter of 2.48 μm and CV of 5.65%. Comparison of Figure 3.5 and Figure 3.2 shows that the polydispersity is worse than in a cast film indicating that some coalescence or fission of emulsion droplets has occurred during printing due to the high shear stress in the nozzle or during droplet formation. Nevertheless, the size distribution of the particles in the printed droplet is much narrower than in our previous study on homogenized emulsions [35], and sufficiently narrow that domains of hexagonally packed spheres are observed.

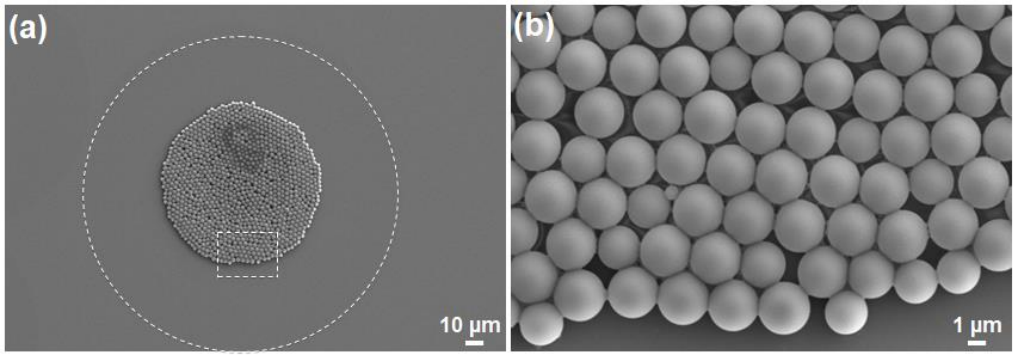

Figure 3.4. SEM image showing the morphology of the deposit with a monolayer of polystyrene particles from emulsions (O, 66.5 mg ml^{-1} PS/DCM; W, 1.0 mg ml^{-1} SDS/water) with 6-µm oil drops on a plasma-treated glass cover slip.

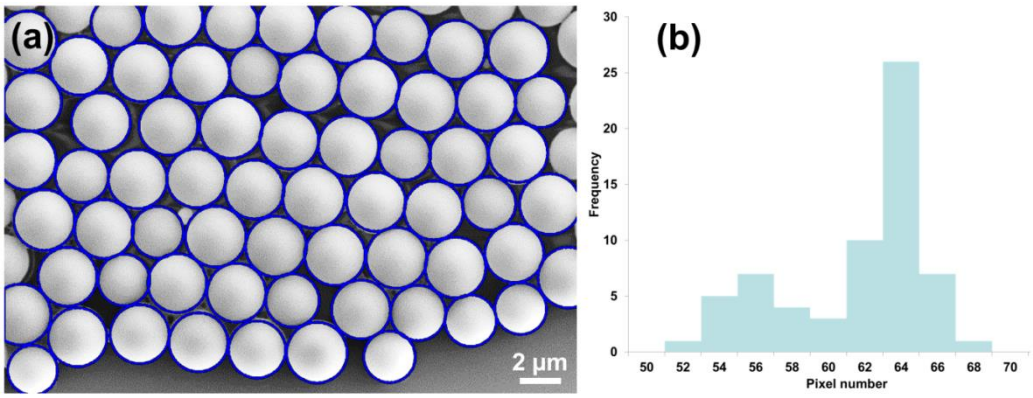

Figure 3.5. Particle size distribution of the sample in Figure 3.4a_2 from inkjet-printed emulsion drops dried on a plasma-treated glass coverslip.

3.2.3. Effect of process parameters on polydispersity

Uniformity of particle size is an important attribute not only for the formation of ordered arrays but for any functional ink in which the morphology of the particles controls the function of the surface. For example, the wall thickness of microcapsules controls the rupture strength of the capsule and the rate of release of its contents. It is thus desirable to control the particle size within as narrow a range as possible. If the polydispersity in the particle size arises from breakup of the oil droplets during printing, then the polydispersity can be improved by reducing the capillary number in one of three ways: decreasing the shear rate, decreasing the droplet size, or increasing the interfacial tension between the

water and oil phase. In this study, I used an 80-µm nozzle instead of the 50-µm nozzle used in our previous work to decrease the shear rate and used the smallest DCM drops that could reproducibly be generated in the flow-focussing device (6-µm diameter). Figure 3.6 shows the consequences of using a smaller nozzle (50 µm; figure 3.6a) or larger initial oil drops (around 9 µm; figure 3.6b), both of which increase the deformation of the emulsion drops. In both cases the particle size distribution is broader than with the 80-µm nozzle and 6-µm DCM drops (Figure 3.5).

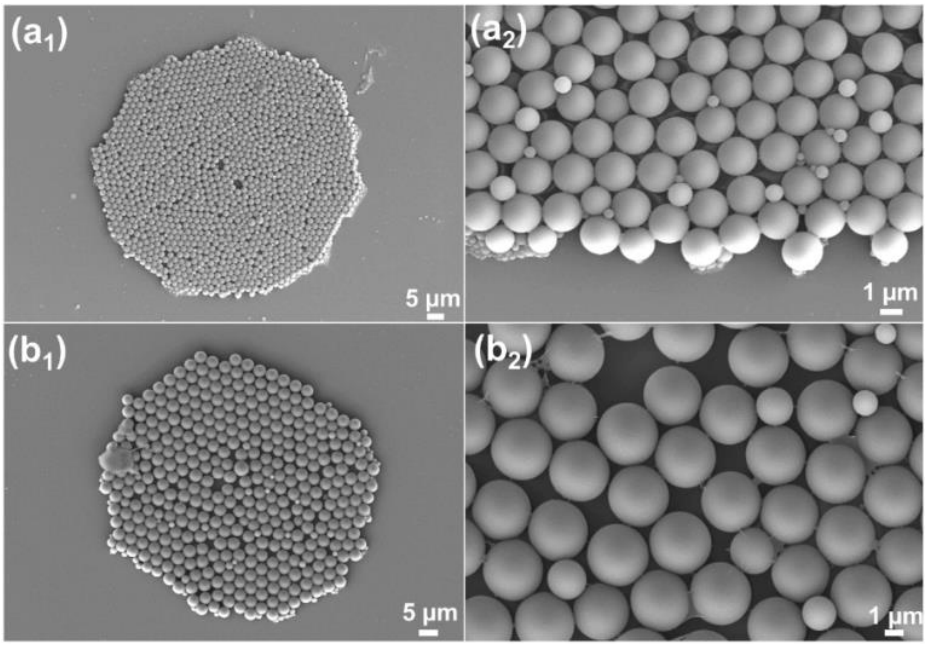

Figure 3.6. SEM images of drying deposits from emulsions (66.5 mg ml^{-1} PS/DCM in1.0 mg ml^{-1} SDS/water) with (a) 6-µm oil drops printed through a 50-µm nozzle, (b) 9-µm oil drops printed through an 80-µm nozzle on plasma-treated glass cover slips.

The interfacial tension depends on the concentration of the emulsifier, SDS, in the aqueous phase. Table 3.2 reports the DCM–water interfacial tension for various concentrations of SDS both above and below the critical micelle concentration (8.2 mM, 0.236 wt%). Above the cmc, the interfacial tension is approximately constant, while it increases rapidly as the surfactant concentration is reduced below the cmc.

Table 3.2. Interfacial tension between DCM containing 5 wt% polystyrene and water containing SDS.

SDS concentration (±0.01 wt%)	Interfacial tension (mN m^{-1})
0	27.5±0.5
0.05	12.4±0.5
0.1	6.5±0.3
0.2	4.9±0.1
0.3	4.7±0.1
0.5	4.5±0.1

To explore the effect of SDS concentration on the printing of emulsions, I prepared emulsions aqueous solutions with 0.05, 0.1 and 0.5 wt% of SDS. Micrographs of oil droplets inside the microfluidic chip show that emulsions were stable with SDS concentrations above 0.1 wt%, but coalescence of droplets occurred at 0.05% SDS. Figure 3.7 compares dry deposits of emulsions printed from 0.1 and 0.5 wt% solutions of SDS. More breakup was observed in the emulsion with the lower surface tension (0.5 wt%) leading to an increased polydispersity of the particles. A surfactant concentration of 0.1 wt% provided the optimal balance of emulsion stability and resistance to droplet deformation during printing.

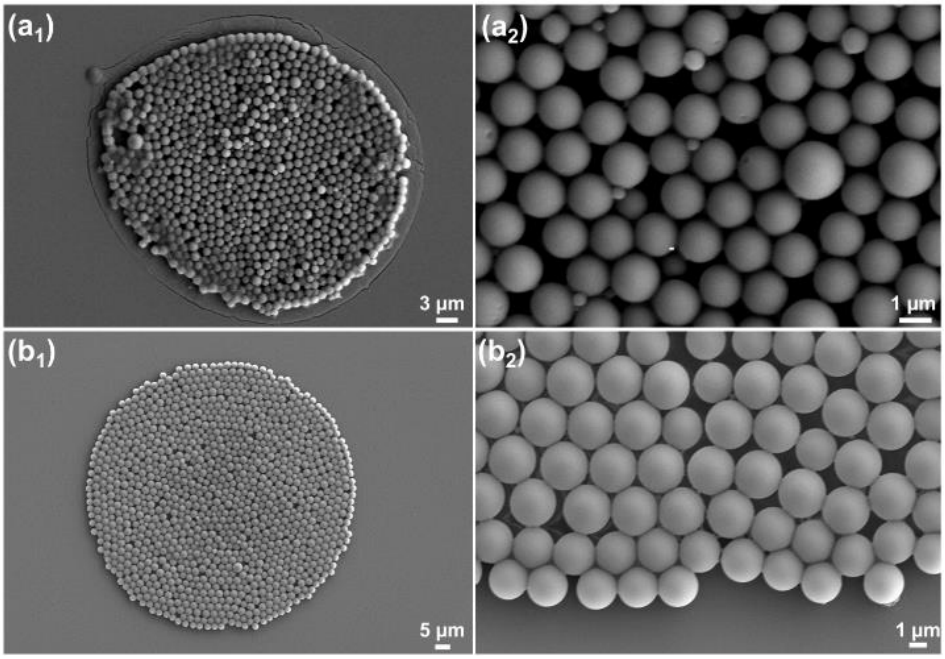

Figure 3.7. SEM images of drying deposits from emulsions comparing 6-µm oil drops (O, 66.5 mg m^{-1} PS/DCM) with (a) 0.5 wt% and (b) 0.1 wt% SDS in the aqueous phase on plasma-treated glass cover slips.

The relative humidity affects the relative evaporation rates of the discrete and continuous phases. Figure 3.8 compares the morphology of deposits from emulsion droplets drying at an RH of (a) 85% and (b) 35%. Close-packed monolayers of particles were obtained at both humidities (a_1 and b_1), but the particles formed at high humidity were more spherical. As high humidity slows down the evaporation of aqueous phase, soft DCM drops have more time to transform into solid polystyrene particles (figure 3.8a_2) before they are compressed together under capillary forces in the latter stages of drying. In Figure 3.8b2, showing a deposit formed at low RH, some of the particles have facetted sides suggesting that they were still soft when they interacted with their nearest neighbours. These images show that despite the much higher volatility of DCM than water, care needs to be taken to ensure that the particles are sufficiently solvent-free before the final stages of evaporation of the continuous phase.

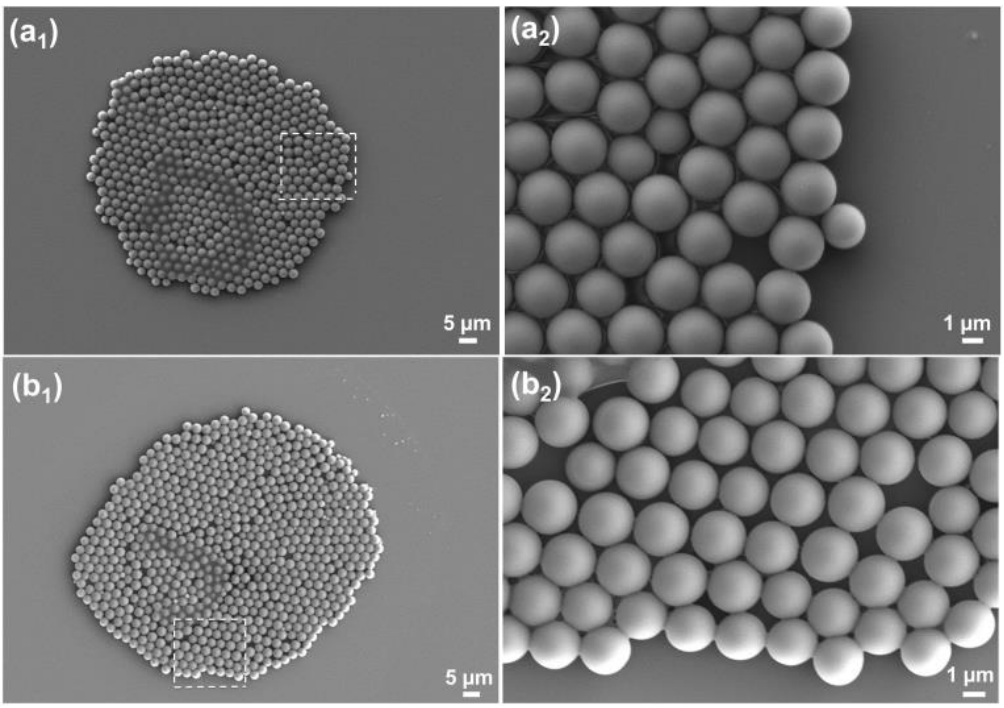

Figure 3.8. SEM images of deposited from emulsions (O, 66.5 mg ml^{-1} PS/DCM; W, 1.0 mg ml^{-1} SDS/water) with 6-µm oil drops dried in air at a relative humidity of (a) 85% and (b) 35% on glass cover slips treated with plasma.

3.2.4. Morphology of dry deposits

Particle size can be readily tuned through variation of the initial DCM droplet size or polymer concentration. To enable a higher monodispersity of particles and a more efficient use of DCM solvent, I use the latter method to obtain a larger particle. Emulsions containing 6-µm diameter oil droplets with two different polystyrene concentrations (0.5 wt% and 5 wt%) were printed onto plasma-treated glass coverslips. In SEM images, deposits of polystyrene particles with a mean diameter of 1.1 µm (Figure 3.9a) and 2.48 µm (Figure 3.9b) were observed. Figure 3.9a shows a typical pattern formed from small particles, although each deposit is different. Characteristic features are a ring-like deposit with a diameter much less than that of the initial contact line of the droplet (60 µm and 295 µm, respectively, in this example) and an irregular hole near the centre of the deposit due to pinning of the contact line in the latter stages of drying. The larger particles (Figure 3.9b) showed a circular deposit with a well-ordered monolayer of particles at the centre (see also Figure 3.8 and 3.7b). As reported above, the diameter of the deposit is smaller than the initial footprint (92 µm and 184 µm, respectively, in this drop). I rationalise the different behaviour in terms of the

capillary force acting on the particles when they deform the interface near the contact line [69]. For the larger particles, the capillary force is sufficient to overcome the friction between the particles and the substrate until a closely packed deposit is formed. For the smaller particles, the capillary force is weaker and the contact line pins before a continuous layer of particles is formed, leading to a ring-like deposit. The hole in the centre arises from outward capillary flows consequent on evaporation with a pinned contact line (the coffee-ring effect). In our previous study [65], with a polydisperse mixture of particles I observed that on a hydrophilic substrate ($\theta_{H_2O} = 20^{o}$) there was size segregation with larger particles concentrated in the central deposit with some small particles deposited at larger radial distances, consistent with the idea that the capillary forces on small particles are less able to overcome the friction with the substrate.

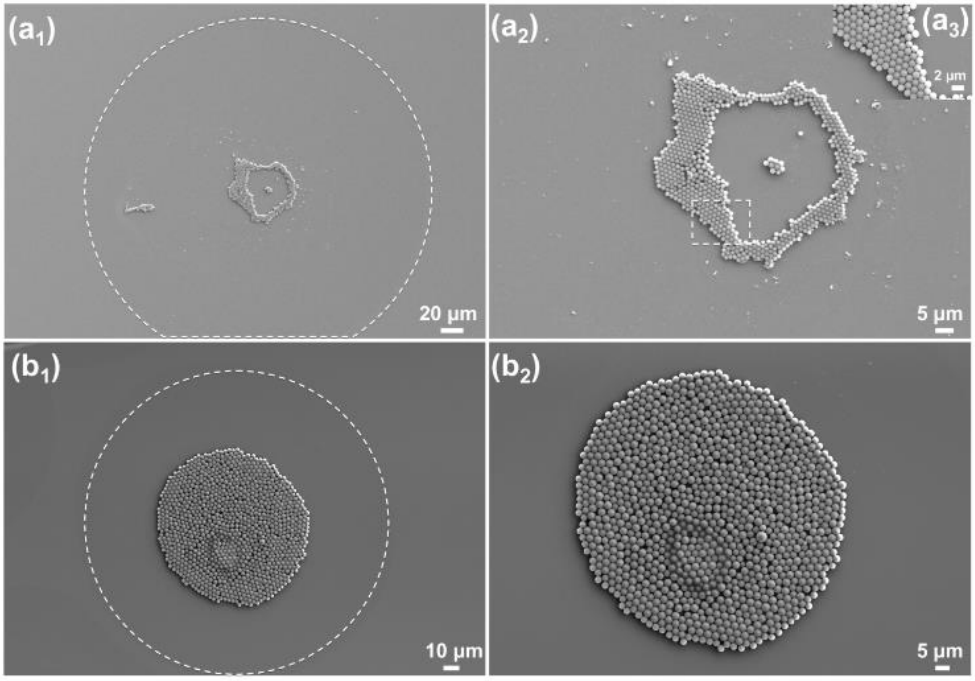

Figure 3.9. SEM images of deposits from emulsions comprising (a) 0.5 wt% and (b) 5 wt% PS/DCM in 0.1 wt% SDS/water with 6-µm oil drops on plasma-treated glass cover slips.

Why small (non-Brownian) particles should be less mobile than large particles can be rationalised in simple physical terms. The increase in surface area of the air–water interface due to deformation by a rigid particle scales with the surface area of the particle i.e as d^2, where d is the particle radius. If the interaction between the particle and the solid surface arises primarily from dispersion interactions (both particle and surface are negatively

charged, so the short-range double-layer forces are repulsive), then the interaction energy between the particle and the surface scales linearly with R [70]. From Hertzian mechanics, the radius, a, of the contact between a spherical particle and planar surface scale as $(LR)^{1/3}$, where L is the load [71]. Thus the contact area scales as $R^{4/3}$. If the friction with the surface depends on the contact area, then the friction decreases more slowly with R than does the capillary force; hence smaller particles are more likely to pin the contact line. Furthermore, the pressure scales as $R^{-1/3}$, so from DLVO theory the thickness of the aqueous film increases with increasing R, which will also reduce the friction due to viscous drag in the thin film between the particle and the substrate [70]. An alternative explanation is that the smaller particles cover a smaller surface area and thus would form a dense deposit later in the drying cycle, when the concentration of the dispersant is much higher. If the dispersant (in this case, SDS) were to form a viscous solution or mesophase at high concentrations (which are only achieved in the last stages of drying), then this increase in viscosity might also hinder the mobility of particles near the contact line.

Formation of sub-micron particles is possible by reducing the polymer concentration in the DCM, but the number of particles is limited by the number of DCM droplets, so a rather sparse deposit is likely to occur unless the number of droplets is increased. This entails reducing the size of the emulsion droplets, which is challenging in microfluidics. Production of particles larger than $\sim 3\ \mu m$ requires larger emulsion droplets and/or higher polymer concentrations. The upper limit on particle size is limited by break-up of large droplets during printing and by the viscosity range that yields droplet formation in the flow-focussing junction. The emulsion solvent evaporation method in inkjet printing is thus best for micron-sized particles rather than nanoparticles or larger particles.

Compared to the cast-drying emulsion, the inkjet-printed emulsion drop and EISA of colloidal suspension form deposits with a lower degree of crystalline order, due to the grain boundaries with defects or cracks in the circular deposits. During drying, the inward capillary force pushed particles to the droplet centre from all directions, hindering the formation of close-packed hexagonal arrays.

3.2.5 Influence of the underlying glass slip

Previous studies have demonstrated that the wetting properties of the substrate influence the deposit pattern [35, 36, 43, 58, 72]. Figure 3.10 compares deposits formed from

emulsions with 0.5 wt% and 5 wt% polystyrene in the oil phase on substrates with two different wettabilities: plasma-treated glass coverslips ($\theta_{H_2O} = 20^{o}$) and HDMS-treated coverslips ($\theta_{H_2O} = 64^{o}$). The 1.1-µm particles formed a ring-like deposit on the hydrophilic substrate and a close-packed monolayer on the more hydrophobic substrate. The 2.48-µm particles formed a close-packed monolayer on the hydrophilic substrate and a multilayer on the more hydrophobic substrate. The maximum diameter of the contact line on the hydrophilic substrate (Figure 3.9a_1 and 3.9b_1) is $\sim$2 times that on the hydrophobic substrate (Figure 3.9a_2 and 3.9b_2) due to the stronger wetting of the hydrophilic surface. Higher contact angles lead to large capillary forces, since the variation in the deformation energy of the surface with the radial position of a particle depends on the slope of the air–liquid interface. For the smaller particles, the increased capillary force is sufficient to prevent pinning. For the larger particles, it can displace particles from the monolayer to form multilayer structures. In addition, the smaller contact radius reduces the distance that the small particles are dragged by the contact line, reducing the opportunities for pinning. For the larger particles, the greater height of the droplet increases the sedimentation time and it is likely that particles from DCM droplets initially near the upper surface of the droplet deposit on top of layers of particles underneath. This study shows the importance of controlling the wettability to obtain uniform, ordered monolayers of particles. It is possible that a monolayer of the larger particles could also be formed on the hydrophobic substrate if the volume fraction of oil (and hence the number of particles) was reduced, but this parameter is not well-controlled in our experiment owing to sedimentation in the tube connecting the microfluidic device to the inkjet nozzle. Close-coupling of the microfluidic chip and the inkjet nozzle would eliminate this issue.

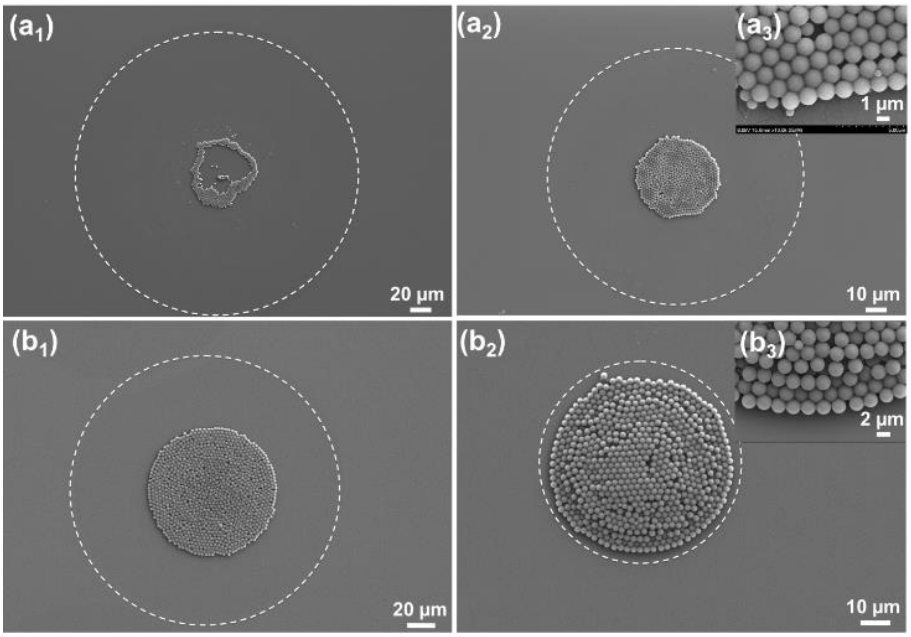

Figure 3.10. SEM images of deposits of (a) 1.1 µm and (b) 2.48 µm particles on (a_1, b_1) hydrophilic and (a_2, b_2) hydrophobic glass coverslips. The insets (a_3, b_3) show enlarged images of the edge of the deposits. The dashed line shows the maximum contact diameter of the emulsion drop.

3.3 Summary

In this chapter, I have demonstrated a strategy to obtain uniform monolayers of polymeric particles by inkjet printing of monodisperse oil-in-water emulsions generated by microfluidics. There is a small increase in the polydispersity of the particles compared to the emulsion (*CoV* in the particle diameter <6% under optimised conditions) which is ascribed to break-up and coalescence of oil droplets during jetting. The polydispersity is minimised by minimising the capillary number during jetting through three strategies: increasing the nozzle diameter to reduce the shear rate, increasing the oil–water interfacial tension and reducing the oil droplet size. The particle size is controlled by the polymer concentration in the oil phase. Relative humidity plays a minor role in the particle formation process. At low RH, the water droplet evaporates faster and some faceting of the particles was observed due to residual solvent in the PS particles as they pack into the monolayer. The effect of the substrate wettability on the morphology of the deposit was briefly explored: well-ordered monolayers of small particles formed on hydrophobic substrates and of large particles on hydrophilic substrates.

The objective of this chapter has been to explore the effect of process parameters on the combined microfluidic/inkjet method for generating uniform layers of particles. For this reason I only used a single chemical system: polystyrene in DCM as the oil phase and SDS solutions as the aqueous phase. The emulsion solvent evaporation method does, however, have wide applicability in terms of polymers, organic solvent and morphology of the particles formed. It can also be used to incorporate functional cargoes. Major benefits of combining the generation of the emulsion and inkjet printing are the reduction of nozzle clogging and avoidance of shelf-life issues since there is no need to stabilise a particle suspension against aggregation and sedimentation.

4. Mechanism of internal phase separation of core-shell microcapsules produced by emulsion solvent evaporation

Abstract

Emulsion solvent evaporation is a well-established method for generating functional particles from solutions of polymer dissolved in volatile solvents dispersed in aqueous solution. We have previously shown this method can be coupled with inkjet printing to produce core-shell microcapsules at a target surface driven by internal phase separation. The emulsion ink contains a shell-forming polymer and a core-forming poor solvent dispersed in an aqueous medium. However, the mechanism of formation of core-shell capsules is not very clear. Here, I show the mechanism of internal phase separation by constructing a ternary phase diagram. Depending on the ratio of polymer to poor solvent, either the polymer or poor solvent can phase separate out from the bulk solution, forming a core-shell structure after drying. Due to the fast evaporation of low-boiling DCM inside the emulsion droplet, there may be insufficient time for binodal decomposition to occur before the composition reaches the spinodal, at which point spinodal decomposition takes place. I discussed conditions necessary to form a core-shell structure. Factors affecting the phase separation process and final capsule morphology are described. Our system uses poly(methylmethacrylate) and hexadecane in dichloromethane as a model system, but this approach can be generalized to a wide variety of polymers, organic solvents and functional cargoes.

4.1 Introduction

The encapsulation of functional cargoes can be achieved by microcapsules, which contain a solid polymer shell and a liquid core. Compared with microspheres comprising active cargoes dispersed through the polymer matrix, microcapsules offers greater versatility for encapsulation and controlled release. For example, the polymer shell can protect encapsulated active drugs against environmental hazards (like moisture and oxidation), and hence increase their shelf life. Microcapsules can release the protected cargoes upon exposure to external triggers (pH, solvents, UV). Besides, microcapsules allow a safe handling of hazardous chemicals and allow them to be embedded in a solid matrix.

Various techniques have been developed to prepare microcapsules with a polymer shell and liquid core, including interfacial polycondensation with spontaneous emulsification [9], layer by layer assembly or polymerization on the surface of solid templates [10], solvent evaporation of pre-produced double emulsion [11] and internal phase separation driven by solvent evaporation in an oil-in-water emulsion [3, 12]. Each method has its own advantages and limitations, and has been optimized for different areas.

In the interfacial polycondensation technique, spontaneous emulsification was used to produce microcapsules. This strategy requires a mixture of diisocyanate monomer, a water-immiscible oil and a lipophilic surfactant completed dissolved in a water-miscible solvent as the oil phase, and an aqueous solution with diol and a hydrophilic surfactant. When the oil phase is mixed with the aqueous solution, the miscible solvent initially in the oil phase diffuse into the aqueous solution, leading to precipitations of oil as nano-oil droplets. An interfacial reaction then occurs between two monomers, forming a membrane encapsulating the oil core. The total removal of solvent gives rise to nanocapsules. However, in this strategy, the unreacted monomer may remain in the oil core as an impurity, and this approach only works for a limited range of polymer with specific solubility.

The template-based layer-by-layer assembly approach is achieved by absorption of several bilayers of alternating polymers on the surface of solid template spheres, followed by dissolution of the sacrificial core. However this template-based method requires multiple processing steps, especially for the inconvenient step of removal of templated solid core by chemical etching. Moreover, the encapsulation of active agent is performed by swelling of the polymeric shell and diffusion of functional cargoes into the microcapsules, leading to a relatively low productivity in encapsulation.

The double-emulsion evaporation method contains a two-step process: first is emulsification of inner droplets into a middle medium, second is the other emulsification process of the formed dispersion. For a w/o/w double emulsion, evaporation of the middle phase with polymer solutions results in a solid polymer wall surrounding the inner aqueous fluid. However, during preparation of the double emulsions, each emulsification step involves polydisperse distribution of droplets, resulting in a heterogeneous double emulsions and hence an ill-controlled morphology for the final microcapsules, consisting of variations in overall microcapsule size, wall thickness and porosity of polymer shells. Similar to the template-based layer-by-layer method, the double emulsion also suffer from a multi-step preparation process. Although homogeneous double emulsions can be prepared by microfluidics [13, 73-84], the overall size of capsules are limited to dozens of microns, which is not suitable for preparation of nano or micron-sized microcapsules.

Many problems mentioned above can be minimized by the method of inner phase separation within an oil-in-water emulsion, which provides a facile one-step process in which microcapsules are formed by evaporation of the discrete phase in the o/w emulsion under ambient environments. This strategy involves an oil-in-water emulsion, which contains, in the dispersed phase, a mixture of polymer, a low-boiling good solvent for the polymer and a high-boiling poor solvent that is miscible with the good solvent but immiscible with the poor solvent. An aqueous solution with a proper dispersant serves as the continuous phase. As is shown schematically in figure 4.1, during the evaporation of good solvent, when the composition reaches the binodal boundary, various small droplets which are rich in polymer and good solvent can phase separate out from the bulk solution within the oil droplet. These small droplets are mobile and move toward the oil/water interface, where they coalesce to engulf the surface, if the wetting conditions are correct. Further evaporation of the good solvent causes the polymer-rich droplets to precipitate at the interface and create a continuous film of polymer as the shell of microcapsules. As for the high-boiling poor solvent, it remains in the middle of oil droplets throughout the whole drying process, forming a liquid core of microcapsules after complete drying of the good solvent. I will show below that the thermodynamic preference for the formation of polymer-rich or polymer-poor droplets depends on the starting composition in relation to the critical point on the three-component phase diagram. I will also show that thermodynamics alone does not explain the experimental observations.

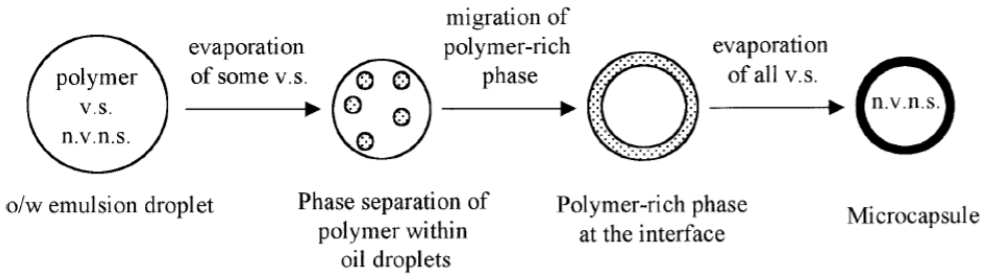

Figure 4.1. Schematic representation of evolution of microcapsules containing a polymer shell and liquid core, n.v.n.s indicates non-volatile non-solvent, v.s. indicates volatile solvent. This figure is adapted from ref[3] with copyright permission obtained.

Loxley and Vincent [3] used the above-mentioned approach of internal phase separation within an oil-in-water emulsion to prepare poly(methylmethacrylate) microcapsules with liquid cores. The emulsion contained poly(methylmethacrylate) as the polymer, a good solvent for the polymer (CH_2Cl_2), a poor solvent (hexadecane, decane, octanol, or tetrachloromethane) in the discrete phase. When hexadecane or decane was used as poor solvent, microcapsules with liquid core and solid shell were produced, as is shown in Figure 4.2. They have indicated that as the good solvents (i.e. DCM) dries, the gradual loss of the organic solvent will trigger a phase separation within the oil droplets when the system hits the binodal curve on the ternary phase diagram. This internal phase separation induced a migration of polymer moving to the oil/water phase, where the polymers engulfed the interface and forming a solid polymer shell after the solvent dries out. However, the microcapsules failed to be produced when octanol, or tetrachloromethane was chosen as poor solvent. As tetrachloromethane is a low-boiling solvent with boiling point of 77°C, it evaporated out with the DCM during the solvent evaporation process, leaving only solid spheres of PMMA after drying.

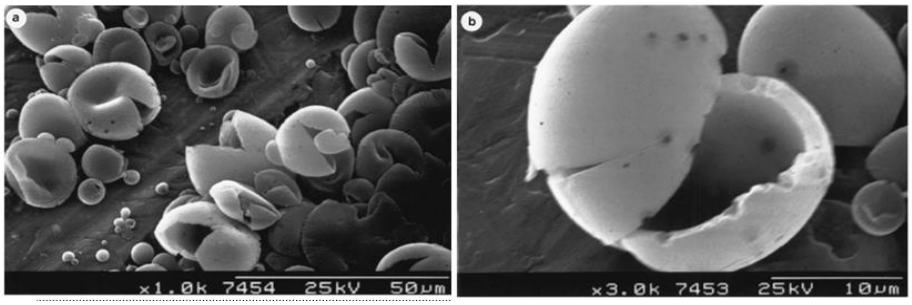

Figure 4.2. SEM images showing microcapsules with polymer shell and liquid core produced from emulsions containing PMMA as polymer, hexadecane as poor solvent, and PMMA as emulsifier, DCM plays as the good solvent. This figure is adapted from ref [3] with copyright permission obtained.

Internal phase separation within oil-in-water emulsions does not guarantee a core-shell structure. There are three equilibrium morphologies: core-shell, acorn-like and two separated spheres (Figure 4.3), which is mainly controlled by the interfacial tensions (σ) of the three phases (aqueous solution, poor solvent, and polymer). [4] When a mixture of immiscible liquids A and B is dispersed into a third medium S, the tendency of a liquid B to spread spontaneously across a surface of liquid A can be predicted by spreading coefficient λ, given by

$$\lambda_{BA} = \gamma_{AS} - \gamma_{BS} - \gamma_{BA},$$

where γ_{AS} and γ_{BS} is the interfacial tension of the third medium S and liquids A or B , γ_{BA} is the interfacial tension between liquid A and B. When the value of spreading coefficient λ_{BA} is positive, liquid B will spontaneously spread across liquid A. Otherwise, partial wetting will occur. In my o/w emulsion system, if I consider polymer and oil solvents as B and A, the equilibrium morphologies of the two-phase particles can be described by the three regimes of coefficient values, giving rise to core-shell capsules, acorn-like particles or two separated particles after phase separation within the emulsions, as is shown in figure 4.3.

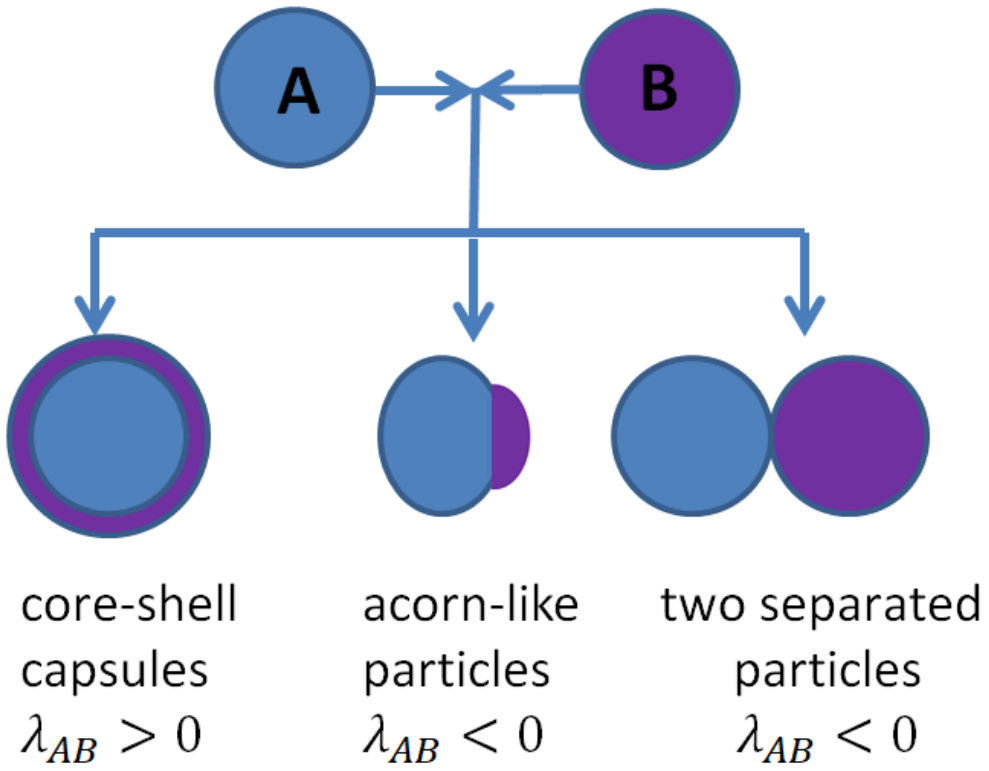

Figure 4.3 . Three possible configurations of two-phase particles: core-shell, acorn-like, two separated spheres. The interfacial tensions of the three phases determines which morphology is most thermodynamically stable.

In general, in order to create a core-shell structured microparticle, the interfacial tension between aqueous phase and poor solvent (γ_{wo}) should be higher than that of the aqueous phase and polymer (γ_{wp}), thus the poor solvent stays in the core. Octanol has a low interfacial tension with water, leading to an acorn-like particle. Neither octanol nor tetrachloromethane are suitable solvents for preparation of PMMA microcapsules, which highlight the importance of boiling point and interfacial tension in preparation of microcapsules.

Besides, for a given polymer in a solvent, the dissolution is governed by the polymer-solvent interaction parameter χ_{S-P}, given by

$$\chi_{S-P} = \frac{V_S(\delta_S - \delta_P)^2}{RT} + 0.34,$$

where V_S is the molar volume of the solvent, δ_S and δ_P the solubility parameters of the solvent and the polymer, respectively, *R* the ideal gas constant, *T* the temperature. The

Flory-Huggins criterion for complete polymer-solvent miscibility is $\chi_{S-P} < 0.5$. For the formulation of DCM/HD/PMMA, χ_{S-P} is 0.34 for DCM/PMMA and 1.42 for hexadecane/ PMMA, thus DCM can be considered as the good solvent for dissolving PMMA, whereas hexadecane is a poor solvent for PMMA.

Surfactants also plays an important role in determining the morphology of microcapsules. Ionic surfactants (like sodium dodecyl sulfate (SDS)) reduce the interfacial tension between the aqueous solution and oil droplets too much, leading to acorn-like microparticles; polymeric surfactants (like poly(vinylalcohol (PVA)) reduce the o/w interface by a moderate amount, thus acting as a suitable emulsifier for the DCM droplets.

As the volatile solvent dries, there is a gradual change in the composition of the three components, with decreasing concentration of good solvent and increasing concentration of poor solvent and polymer. When the composition crosses the binodal curve of the ternary phase diagram, phase separation can take place. Loxley and coworkers [3] constructed a ternary phase diagram by preparing emulsions with accurately weighted materials, and reweighing the emulsion when it showed the first sign of cloudiness. The mass loss was attributed solely to the evaporation of volatile solvent, thus a point on the binodal curve of the ternary phase diagram could be determined, as is shown in figure 4.4. This method does not establish the tie-lines and hence the composition of the co-existing phases is not determined. According to the phase diagram in Figure 4.4, the hexadecane-rich phase would separate out as droplets for almost all initial compositions, not the polymer-rich phase. The ternary phase diagram is a useful tool for predicting the points where phase separation occurs, for example, for an initial composition of 0.5wt% PMMA, 0.5 wt% hexadecane, 99 wt% DCM, the phase boundary is reached at approximately 70% DCM, resulting in a size of oil droplet that is 90% of its initial droplet size.

However, in practice, it is challenging to set a suitable criterion for the transition from clear solution to cloudy phases, especially for compositions near the critical point where the two separated phases have similar compositions and therefore similar refractive indices. Thus I uesd NMR for construction of the ternary phase diagram.

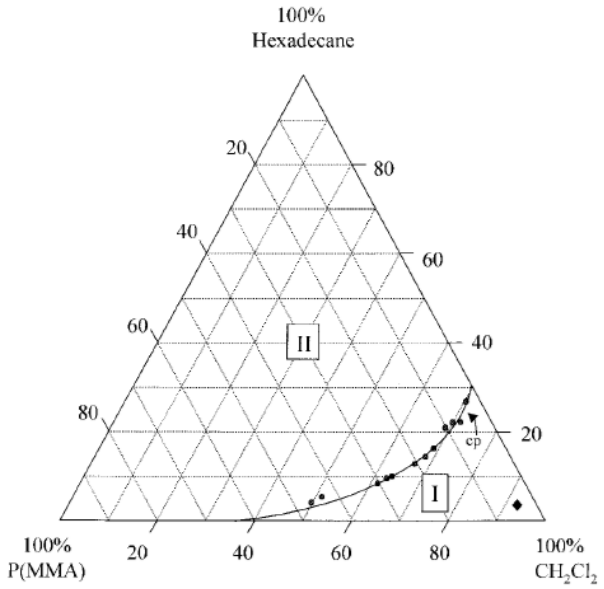

Figure 4.4. Experimentally measured ternary phase diagram for DCM/PMMA/hexadecane system by Loxley and coworkers [3]. I and II represents the one-phase and two-phase areas. Each corner represents 100 wt% of corresponding component, and the axis opposite each corner means 0 wt% of the material. The sum of three components for each point in the ternary phase diagram is 100 wt%. (This figure is adapted from ref[3] with copyright permission obtained.)

Vincent and co-workers [5] investigated the release rates of microcapsules by dissolving a UV-responsive ingredient (4-nitroanisole) in the oil phase before emulsification. This active molecule should be soluble in the organic core (hexadecane) and also have some solubility in the aqueous phase, thus providing a driving force for release. By measuring the UV-absorbance in the aqueous solution with time, the release rate for the microcapsules could be determined. They showed that the release rate is significantly affected by shell morphology and thickness, as is shown in figure 4.5. The evaporation rate of the volatile organic solvent affects the porosity of the polymer shell: rapid removal of the good solvent by rotary evaporation leads to large cracks or pores on the surface of microcapsules, giving rise to a higher release rate compared to that obtained by slow evaporation with free drying overnight. Reducing the evaporation rate of the good solvent has been demonstrated to reduce the porosity of the polymer shell significantly and hence the release rate of the active ingredient. Also increasing the thickness of the polymer shell with polymer concentration was found to slow down the release rate, as well as the total amount of released agents. The

reduction in release rate is mainly by diffusion of 4-nitroanisole through the pores of thicker polymer walls, and the decrease in released amount is due to retention of active ingredient inside the polymer shell.

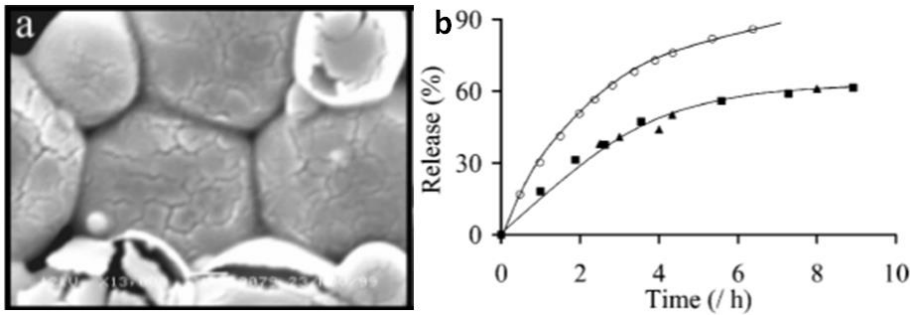

Figure 4.5. (a) SEM images showing microcapsules with cracked shells. (b) The release profile of 4-nitroanisole with different evaporation rate of volatile solvent (DCM), the hollow circle indicates fast rotary evaporation, the dark points indicate slow evaporation by free drying overnight (adapted from ref [5] with copyright permission obtained.).

The novelty of this chapter is to characterise the three-component phase diagram for PMMA / dichloromethane/ hexadecane mixtures in order to improve our understanding of how microcapsules form in emulsion solvent evaporation. Besides, this chapter studied the effect of difference processing parameters (i.e. droplet size, solvent to polymer ratio, evaporation rate and underlying substrates) on the morphology of the core-shell microcapsules, providing a reasonable prediction for the timing of the phase separation and microcapsule formation.

4.2 Discussion

The strategy for forming core-shell microcapsules prepared by solvent emulsion evaporation method requires an oil-in-water emulsion, wherein the oil phase contains a mixture of a shell-forming polymer and a core-forming poor solvent, and the aqueous phase contains a proper dispersant. In particular, the good solvent should be a low-boiling solvent compared to water, so the preferential evaporation of the good solvent before the continuous phase can produce discrete polymeric particles rather than continuous films of polymer; whereas

the poor solvent should be a high-boiling liquid that is immiscible with polymer, so it remains in the core of microcapsules after complete drying of the aqueous phase.

The dissolution of a given polymer in a solvent is governed by the polymer-solvent interaction parameter χ_{S-P}, given by $\chi_{S-P} = \frac{V_S(\delta_S-\delta_P)^2}{RT} + 0.34$, where V_S is the molar volume of the solvent, δ_S and δ_P the solubility parameters of the solvent and the polymer, respectively [85-90]. The Flory-Huggins criterion for complete polymer-solvent miscibility is $\chi_{S-P} < 0.5$. In our model system, δ_S is 19.8 $MPa^{1/2}$ for DCM and 16.4 $MPa^{1/2}$ for HD, and δ_P is 16.4 $MPa^{1/2}$ for PMMA, leading to a value of χ_{S-P} = 0.34 for DCM-PMMA and 1.42 for HD-PMMA. Thus, DCM is chosen as the good solvent, HD as the poor solvent, and PMMA as the polymer in the present study. During the drying process of emulsion inks on substrates, removal of the good solvent leads to internal phase separation, resulting in a polymer-rich phase and a phase rich in the poor solvent. To better understand the phase separation process during drying, we need to consider the phase behaviors of the DCM/PMMA/HD system.

4.2.1 Determination of ternary phase diagram for DCM/PMMA/HD

The ternary phase diagram for DCM/PMMA/HD system was constructed by mixing pre-weighed amount of each material in an NMR sampling tube with a 4.2 mm inner diameter. The amount of PMMA was fixed at 0.05g, HD remained at either 0.1g or 0.15g, while DCM varied in a range of 0.1–0.5g to obtain different compositions within the phase diagram. PMMA was first dissolved in DCM and incubated in a 40^0C water bath for 1 hour to ensure complete dissolution of polymer. HD was subsequently added and the sample was shaken by hand at least 50 times to homogenize the mixture. The cloudy mixture of DCM/PMMA/HD was allowed to phase separate at ambient conditions for 1 hour until two distinct separated layers (i.e. a PMMA-rich lower phase and a HD-rich upper phase) with a fixed boundary line was formed. Each layer was transferred to a different NMR tube with sufficient $CDCl_3$ by a gas-tight syringe. The prepared samples were immediately sent for NMR measurements. During the sample preparation process the NMR tube remained sealed by a cap, except for the adding of material or transferring of solutions, to avoid the loss of low-boiling solvent. 1H-NMR spectra were collected using a Varian VNMRS-600 spectrometer with operating frequencies of 599.42 MHz for ^{1}H. Vibrations during NMR measurements were minimized to reduce the fluctuations in the NMR spectrum. Selected peaks in the proton NMR spectra corresponding to DCM, PMMA or hexadecane were integrated (see Figure 4.7) and compared to each other to determine their relative ratios in

the different phases. The compositions of the PMMA-rich phase and HD-rich phase on the binodal of the ternary phase diagram were established and a binodal curve was obtained by fitting the experimental data. As a check on the reliability of the NMR process, the initial composition should lie on the tie line between the two compositions on the binodal. If, for example, volatile DCM were lost in the sample preparation process, the initial composition would lie on the DCM-rich side of the tie line.

As the total composition approaches the critical point, the compositions of the two phases at equilibrium tend towards the critical composition. It becomes increasingly challenging to determine the tie lines for three reasons: (i) the decreasing interfacial tension slows down the coalescence of the droplets; (ii) the decreasing density difference slows down creaming of the emulsion; (iii) it is difficult to observe the boundary between the two phases because the refractive indices approach the same value. Hence the critical point obtained in the ternary phase diagram is just an estimation of the extremum point on the fitted binodal curves. The solution viscosity depends predominantly on the polymer concentration. I experimentally observed that when the DCM concentration is below 50 wt%, a solution-to-gel transition occurs in the polymer-rich phase in the NMR tube, which freezes the motion of molecules and thus suppresses the phase separation. The ternary phase diagram thus only provides information for DCM above 50 wt%.

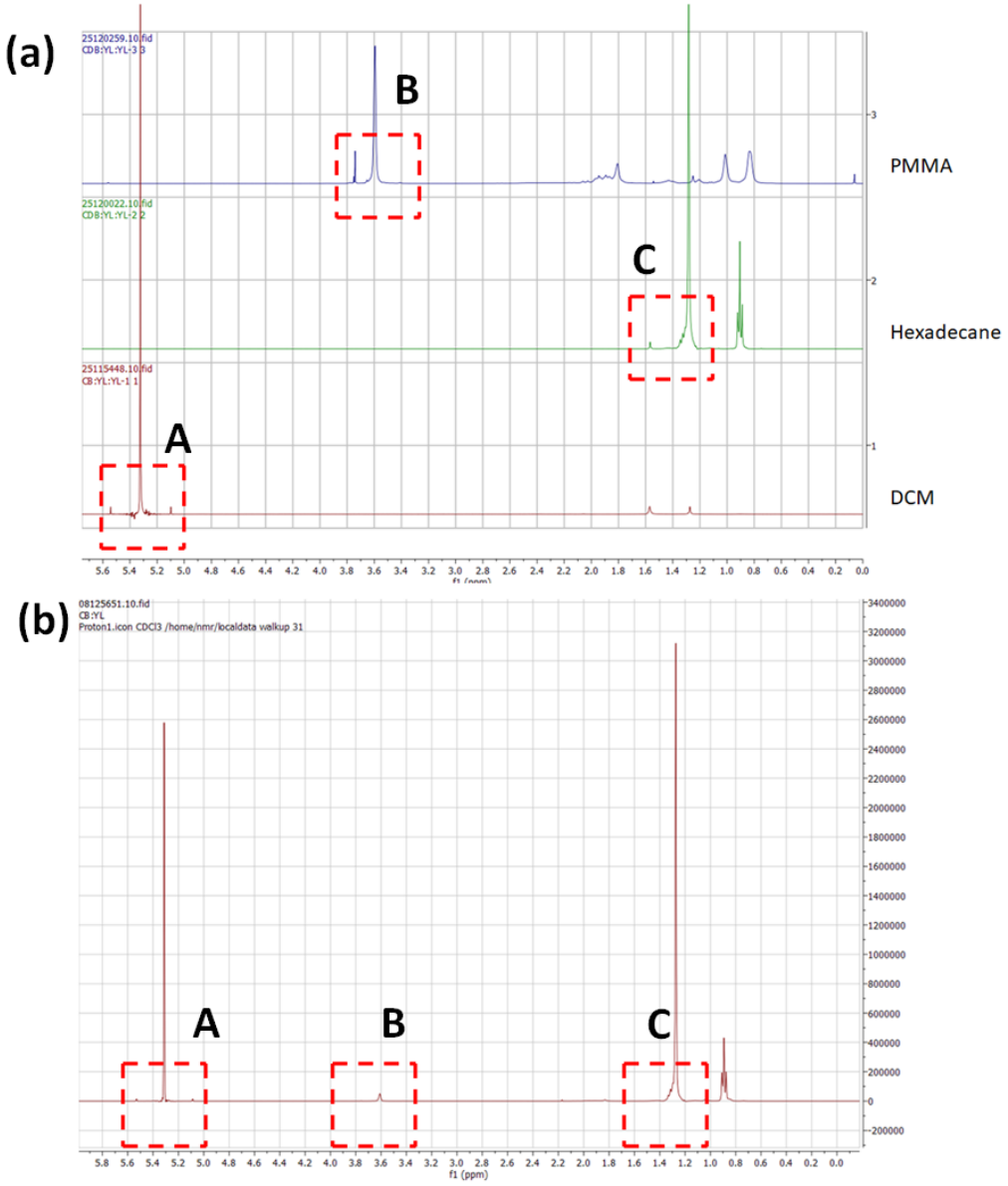

Figure 4.7. (a) a stack ^{1}H-NMR spectra for DCM, PMMA and hexadecane respectively, A, B and C indicate corresponding chemical shift for DCM, PMMA and hexadecane. (b) ^{1}H-NMR spectra for DCM/ PMMA / hexadecane system dissolved in deuterated chloroform. The horizontal axis represents chemical shift, and the vertical axis represents signal intensity.

For the ^{1}H-NMR spectrum, chemical shifts provide information about the molecule structures. For instance, there is one specific chemical shift for DCM, i.e. 5.32 ppm (A) for the -CH_2 group; For PMMA, there are three different groups of chemical shifts: 3.60 ppm (B) for one of the -CH_3 groups, 1.81 ppm for the CH_2 group, and 0.75-1.05 ppm for the other -CH_3 group. (Multiple peaks appear for the CH_2 and α-methyl groups depending on the

tacticity of the polymer.) For HD, there are two different chemical shifts: 1.29 ppm (C) for the 14 -CH_2 groups, and 0.90 ppm for of the two equivalent -CH_3 groups. Besides, the integration of NMR signal intensity is proportional to the number of hydrogen nuclei whose resonance leads to the signal. By integrating the different NMR resonances, the relative ratio of distinct hydrogens and corresponding molecules can be measured. Moreover, since there is no overlap between chemical shift A, B and C (see Figure 4.7b), the composition mass ratio of molecules can be calculated by $\frac{I_{DCM}M_{DCM}}{N_{DCM}} : \frac{I_{PMMA}M_{PMMA}}{N_{PMMA}} : \frac{I_{HD}M_{HD}}{N_{HD}}$, where *I* is the integrated area, *M* the molecular weight and *N* the number of hydrogens contributing to the peak with the chemical shift A, B, C (N = 2, 3 and 28 for DCM, PMMA and HD, respectively.)

Table 4.1 Compositions for mixtures containing DCM/PMMA/HD. Each initial mixture gives rise to a corresponding HD-rich layer and PMMA-rich layer after complete phase separation.

sample	Initial mixture (±0.1wt%)			HD-rich layer (±0.1wt%)			PMMA-rich layer (±0.1wt%)		
1	DCM	PMMA	HD	DCM	PMMA	HD	DCM	PMMA	HD
2	52.7	11.1	36.3	50.9	0.4	48.6	56.4	31.9	11.7
3	54.9	14.1	31.1	52.9	0.7	46.4	58.0	30.5	11.5
4	60.2	12.3	27.5	58.6	0.2	41.2	62.0	26.1	12.0
5	60.5	9.5	29.9	58.9	0.3	40.8	62.4	23.5	14.0
6	63.7	8.5	28.0	62.9	0.3	36.8	65.0	20.5	14.5
7	63.9	11.1	25.0	62.9	0.4	36.8	65.1	21.0	13.9
8	67.3	9.9	22.8	66.9	1.0	32.2	68.0	16.5	15.5
9	68.5	7.6	24.0	67.8	1.6	30.6	68.3	13.5	18.2

The experimentally determined ternary phase diagram is shown in Figure 4.8, representing phase behaviours of mixtures containing DCM/PMMA/HD under ambient conditions at 21–23°C and relative humidity of 30–35%. The concentration of each species is 100 wt% (pure phase) in each corresponding corner of the equilateral triangle and 0 wt% along the axis opposite to it; the percentage of a specific species decreases linearly with increasing distance from its corner. For a given point inside the ternary plot, the composition of DCM/PMMA/HD can be calculated by

$$X_{DCM} = \frac{L_{DCM}}{L}, X_{PMMA} = \frac{L_{PMMA}}{L}, X_{HD} = \frac{L_{HD}}{L}, L = L_{DCM} + L_{HD} + L_{PMMA}$$

where L_{DCM}, L_{PMMA}, L_{HD} is the perpendicular distance from the given point to the side opposite the DCM, PMMA and HD corner, respectively.

A typical feature of the ternary phase diagram is the binodal curve, which separates a one-phase region and a two-phase region. The one-phase region is near the DCM corner of the ternary phase diagram, any mixture in this area represents a homogenous DCM solution with completely dissolved PMMA and HD. Whereas in the two-phase region, the ternary system will phase separate into two distinct liquid phases: a polymer-rich phase and HD-rich phase. Tie lines connect compositions of the resultant phases in equilibrium, shown as red dots in Figure 4.8. In particular, any mixtures with an overall composition along a tie line will split into two phases with the same compositions but different relative volumes.

Upon drying, DCM gradually evaporates by diffusion through the aqueous phase while the mass of PMMA and HD remains approximately constant within the emulsion droplets, resulting in a constant ratio of PMMA to HD. This fixed ratio of PMMA to HD leads to the composition following a straight line from the DCM corner, through the initial point of droplet composition, ending up at the PMMA/HD axis.

There is a polymer-rich side and HD-rich side on the binodal, meeting at a critical point, at which the compositions of two phases are identical. If we draw a line from the DCM corner through the critical point, it ends up at a point of approximately 80 wt% HD / 20wt% PMMA on the PMMA/HD side. Any compositions above the critical line will phase separate into a PMMA-continuous phase surrounding a HD-discrete phase. Otherwise, for any systems below that line, small PMMA-rich droplets will be expected to separate out from the bulk HD-rich continuous phase. When the system crosses the binodal, the discrete phase forms by an activated ‘nucleation and growth’ process, so the number of droplets of the discrete

phase depends on the density of nucleation sites. Furthermore, if nucleation is slow compared to the rate at which the droplet is evaporating, the droplet can remain in a metastable one-phase state even after it has crossed the binodal line in the phase diagram.

Besides, I note that phase separation will not yield pure binary mixtures, i.e. DCM/PMMA or DCM/HD before the last drying of good solvent. In fact, both phases are still ternary mixtures of DCM/PMMA/HD. For example, for an initial composition of 67.3 wt% DCM, 9.9 wt% PMMA and 22.8 wt% HD, phase separation gives rise to a PMMA-rich phase containing 68 wt% DCM, 16.5 wt% PMMA and 15.5 wt% HD, and a HD-rich phase with 66.9 wt% DCM, 0.98 wt% PMMA and 32.2 wt% HD. Note that the amount of HD is nearly same as PMMA in the PMMA-rich phase and the HD content only reduces slowly as the DCM content decreases; consequently the diffusion of HD out of the PMMA-rich phase is an important process in the formation of a polymer-rich shell. Conversely, there is very little PMMA in the HD-rich phase. As the composition hits the binodal and moves further away from the DCM corner of the phase diagram, the HD-rich phase moves along the HD-rich boundary. Since HD and PMMA are very poorly miscible in the absence of DCM, the phase boundaries end very close to the PMMA and HD corners.

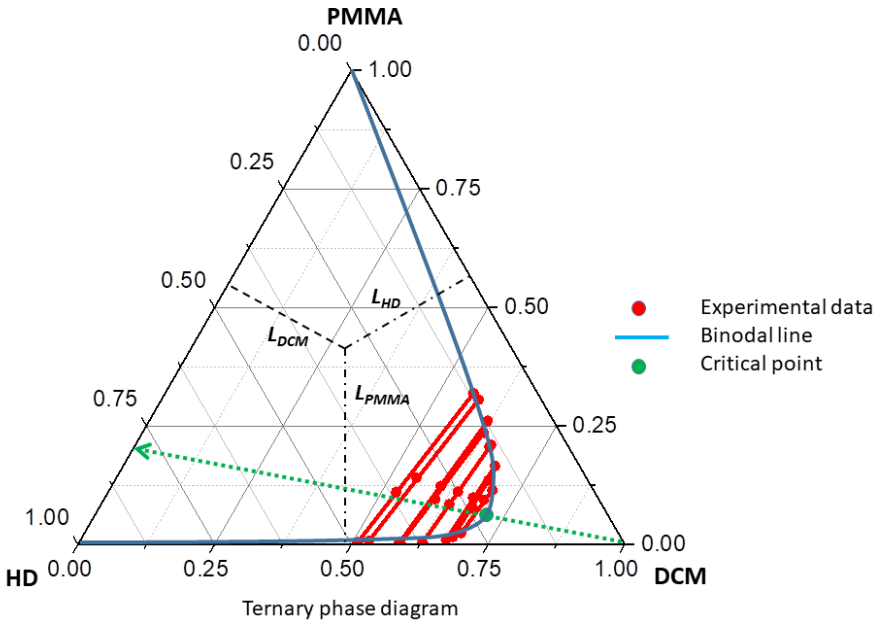

Figure 4.8. Experimentally determined ternary phase diagram for the DCM/ PMMA / HD system with 0.05g PMMA and varying amount of HD (0.1 or 0.15g) and DCM in the initial composition. The red dots on the binodal are measured by integration of NMR spectra, the red dots in the middle of tie lines represent initial compositions weighed by a high-precision balance, and the red lines are ties lines connecting the equilibrium phases. The green dot is the critical point of the fitted binodal. The axes are marked in wt%.

4.2.2 Microcapsule morphology

Figure 4.9 schematically shows the expected drying process of core-shell microcapsules. First, as shown in Figure 4.9a, an oil-in-water emulsion is prepared, which contains an oil phase predominantly formed of DCM with a small amount of PMMA and HD. The oil phase is then emulsified with an aqueous phase containing a chosen dispersant and allowed to dry under ambient conditions. Second, as shown in figure 4.9b, removal of the good solvent triggers phase separation within the emulsion droplets; depending on the ratio of PMMA to HD, either polymer-rich or HD-rich component will separate out as (multiple) small droplets from the bulk solution. During drying, the concentration gradient of PMMA or HD can be predicted by the Peclet number, *Pe* given by $Pe = \frac{Er}{D} = \frac{6\pi Er\mu a}{kT}$. If we consider PMMA and HD as small spherical objects in solution, the radius of gyration gives a measure of the radius, a, of the sphere [90-92]. For the DCM/HD/PMMA system, , a_{PMMA} = 4.8 nm and a_{HD} = 0.48 nm. The viscosity of pure DCM μ = 0.43 mPa s and this will be representative of the

initial dilute formulation. The viscosity of PMMA/DCM mixtures increases with increasing concentration of polymer, reaching ~100 mPa s at the phase separation point in the binary mixture (~10 wt% PMMA/DCM) [93]. The corresponding diffusion coefficient of PMMA in DCM decreases from ~1 × 10^{-10} ms^{-2} to ~ 4 × 10^{-13} ms^{-2}. I did not measure the viscosity of the PMMA-rich solutions along the binodal, but given that the PMMA concentration rapidly exceeds that in the 10% PMMA/DCM mixture, it is likely that the viscosity increases rapidly to values > 100 mPa s. Meanwhile, the viscosity of the HD-rich phase approaches that of pure HD (μ = 3.45 mPa s) as the DCM evaporates. Consequently, the diffusion coefficient of HD in DCM only decreases from ~1.2 × 10^{-9} ms^{-2} to ~ 1.4 × 10^{-10} ms^{-2}. However, the diffusion coefficient of HD in the PMMA-rich phase will be very much lower due to the high viscosity of the PPMA/DCM solution.

For initial 1-µm diameter oil droplets drying in a cast film, the evaporation rate $E \sim$ 0.1 µm s^{-1} and the droplet radius $r \sim$ 6 µm, resulting in a $Pe \sim$ 0.006 and 0.0006 for PMMA and HD respectively in the early stage of drying, and $Pe \sim$ 0.5 and 0.05 for PMMA and HD in polymer-rich phase, assuming a viscosity of 100 mPa s. The Peclet number represents the relative importance of convection versus diffusion, a value of Pe < 1 indicates diffusion plays a dominant role in the mass transport and hence the concentration of PMMA and HD are approximately uniform throughout the emulsion droplet within each phase. The only exception is near the final stages of evaporation of DCM, when the diffusion is significantly slowed down in the highly viscous (or gel-like) polymer solutions that were observed with DCM less than 50 wt%.

In the idealistic case for initial compositions above the green line in Figure 4.8, as DCM evaporates, HD-rich droplets nucleate when the composition crosses the phase boundary. These droplets grow in size as DCM evaporates further and coalesce into a single large droplet that forms the oil core, with the polymer forming a uniform shell.

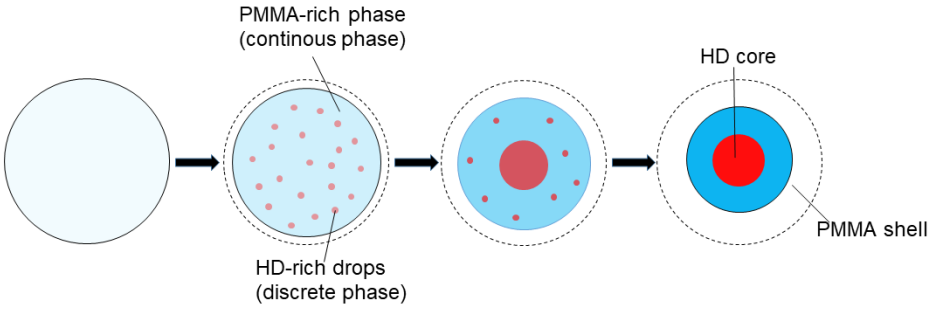

Figure 4.9. Schematic diagram for the phase separation in emulsion droplets and subsequent formation of microcapsules with PMMA shell and HD core. Gradual evaporation of DCM shrinks the emulsion droplet size, the dotted line represents the footprint of the initial emulsion droplet; more concentrated polymer-rich continuous phase and HD-rich drops (as presented by the increasing darkness of their colors). This drawing is based on ref [35].

Assuming the final particle contains a core-shell structure with a uniform thickness of polymer shell and a single oil core, for a microcapsule of shell thickness δ and oil radius r_o, the mass ratio of polymer to HD is given by

$$\frac{m_{PMMA}}{m_{HD}} = \frac{\frac{4}{3}\pi[(\delta + r_o)^3 - {r_o}^3]\rho_{PMMA}}{\frac{4}{3}\pi(r_o)^3\rho_{HD}}$$

Substituting, $\rho_{HD}/\rho_{PMMA} = 0.6525$, and rearranging gives the ratio of shell thickness to the oil core radius, namely

$$\frac{\delta}{r_o} = \sqrt[3]{\left(0.6525\frac{m_{PMMA}}{m_{HD}} + 1\right)} - 1$$

Table 4.2 reports the calculated ratio of shell thickness to the oil core radius for different droplet compositions. I note that with the same amount of PMMA and HD, the polymer shell thickness is only about 1/4 of the HD core radius.

Table 4.2 ratio of shell thickness δ to oil core radius r for different compositions.

m_{PMMA}/m_{HD}	$\delta/\ r_o$	m_{PMMA}/m_{HD}	$\delta/\ r_o$
4:1	0.7100	1:2	0.1447
2:1	0.4422	1:3	0.1006
1:1	0.2599	1:4	0.0772

However, in real cases, microcapsules produced by the method of evaporation-driven phase separation displayed more complex morphology rather than simple core-shell structure. Figure 4.10 shows particles produced by cast drying of homogenized emulsions with varying amount of PMMA and HD solution. 0.1 wt% PVA aqueous solution served as the aqueous phase. The total amount of PMMA and HD was fixed at 1 wt%, and the relative mass ratio of PMMA to HD was chosen to be 1:1, 1:2, and 1:5, respectively. After complete drying of the aqueous phase, the dry deposits were imaged by SEM. Characteristic features of the deposits are

(i) acorn-like capsules with non-uniform distribution of polymer shell, i.e., a relatively thick-layer covering half or more of the surface of the capsule with a thin smooth sheet of polymer covering the remainder of the surface;

(ii) many micron-sized craters in the thick part of the shell, which do not appear to penetrate the whole of the shell (the inside of the shell seen in the broken capsule in Fig 4.10(c) does not contain pores);

(iii) sub-micron polymer beads decorating the inside of the capsule wall.

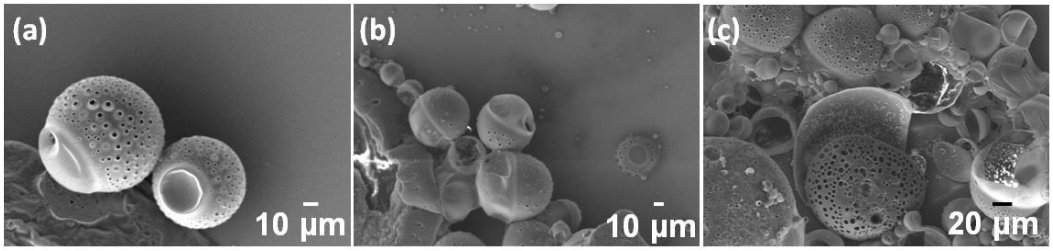

Figure 4.10. Cast drying of a hand-shaken emulsion: (a) $5.0\ \mathrm{mg\ ml^{-1}}$ PMMA, $5.0\ \mathrm{mg\ ml^{-1}}$ HD /DCM; (b) $3.3\ \mathrm{mg\ ml^{-1}}$ PMMA, $6.6\ \mathrm{mg\ ml^{-1}}$ HD /DCM; (c) $1.7\ \mathrm{mg\ ml^{-1}}$ PMMA, $8.3\ \mathrm{mg\ ml^{-1}}$ HD /DCM. In each case the aqueous phase contained $3.3\ \mathrm{mg\ ml^{-1}}$ PVA.

The acorn-shaped structure is characteristic of pseudo partial wetting. To successfully form core-shell structured particles, the emulsion must meet several wetting conditions. First, the interfacial tension between the aqueous phase and the phase rich in the poor solvent must be larger than that between the aqueous phase and the polymer-rich phase, so as the good solvent evaporates, the poor solvent remains in the core and the polymer migrates toward the o/w interface forming the shell. Given that the polymer-rich phase forms the shell, the spreading of the polymer phase at the oil-water interface, and the final particle morphology, depends strongly on the spreading coefficient and Hamaker constant. The spreading coefficient $S = \gamma^{ow} - (\gamma^{pw} + \gamma^{po})$, where γ^{ow}, γ^{pw}, γ^{po} are the water-oil, polymer-oil, and polymer-water interfacial free energies at a given point on the phase diagram, i.e. with varying concentrations of DCM, and in the presence of the chosen emulsifier. If $S > 0$, the free energy of the system is reduced by replacing a hexadecane/water interface by water/polymer and polymer/hexadecane interfaces, thus favouring complete spreading. If $S < 0$, the polymer will not fully wet the o/w interface thermodynamically, but will form a contact line with a finite contact angle determined by the balance of interfacial tensions. In the absence of DCM (subscript, 0) and in the presence of 0.1 wt% PVA, the measured interfacial tensions are γ^{ow} = 21.6 $\mathrm{mN^{-1}}$, γ^{op} = 14.6 $\mathrm{mN^{-1}}$ and γ^{pw} = 18.8 $\mathrm{mN^{-1}}$ [3], leading to $S = -11.8\ \mathrm{mN^{-1}} < 0$. This negative value of S should yield partial wetting. According to the ternary phase diagram, after phase separation, the polymer and oil phase are still ternary mixtures rich in DCM instead of being a single component. The residual DCM substantially reduces the interfacial tensions, especially between the two DCM-rich phases. Table 4.3 shows the interfacial tensions between the polymer-rich and HD-rich phases and the aqueous solution for one particular phase-separated mixture. The interfacial tension

between the two co-existing DCM phases was too low to measure by pendant drop tensiometry, indicating that the Bond number is >> 1 and hence that the IFT was << 1 mN m^{-1}. It is thus likely that the spreading coefficient $S > 0$ during the initial phases of capsule formation.

Table 4.3. Interfacial tension between polymer-rich phase (or HD-rich phase) and aqueous phase(0.1 wt% PVA solution)

Oil phase	Interfacial tension (mN m^{-1})
67.8 wt% DCM, 1.6 wt% PMMA, 30.6 wt% HD (HD-rich phase)	9.5 $\pm$ 0.1
68.3 wt% DCM, 13.5 wt% PMMA, 18.2 wt% HD (PMMA-rich phase)	8.7 $\pm$ 0.1

The morphology is determined not only by the spreading coefficient but also by the Hamaker constant, $\mathrm{A_{wpo}}$, which describes the long-range interactions between the water and oil phases separated by polymer shell. According to the combining correlation $A_{wpo} = (\sqrt{A_{ww}} - \sqrt{A_{pp}})(\sqrt{A_{oo}} - \sqrt{A_{pp}})$ with $A_{ww} = A(water\text{–}air\text{–}water) = 3.7 \times 10^{-20}$ J, $A_{oo} = A(hexadecane\text{–}air - hexadecane) = 5.2 \times 10^{-20}$ J and $A_{pp} = A(PMMA\text{–}air - PMMA) = 7.1 \times 10^{-20}$ J.[94] I calculate $A_{wpo} = 0.285 \times 10^{-20}$ J. A positive Hamaker constant indicates an attractive force between the water and oil causing the polymer layer to thin. For the case of $S > 0, A > 0$, it is favourable to form a lens of polymer with a small contact angle in equilibrium with a thin finite thickness of a polymer film rather than a uniform thickness of polymer shell enclosing the oil core.

Another possibility for the non-uniform distribution of core-shell structure is the density difference between the PMMA-rich phase and HD-rich phase. The PMMA-rich phase is denser than the HD-rich phase with which it is in equilibrium, so the HD-rich core could rise toward the top of the emulsion droplet and thus thin the polymer shell on the top hemisphere. The sedimentation rate of the oil core, *v*, can be approximately estimated by

$v = 2(\Delta\rho)gr^2/9\mu_c$, where $\Delta\rho$ is the density difference between the two phases, *g* the gravitational constant, *r* the droplet radius and μ_c the viscosity of the continuous phase. For a PMMA/HD ratio of 1:2, the equilibrium compositions right after phase separation are 58.6 wt% DCM/ 0.21 wt% PMMA/ 41.2 wt% HD for the discrete HD-rich phase and 61.9 wt% DCM/ 26.1 wt% PMMA/ 12.0 wt% HD for the continuous PMMA-rich phase. At this point, the density difference is about 0.12 $\mathrm{g\ cm^{-3}}$. However, such a high polymer concentration results in a viscosity at an order of 100 $\mathrm{Pa\ s}$ [95] for the continuous phase, and it increases rapidly with PMMA concentration [95]. For a 10-µm diameter droplet, *v* $\sim$ 0.06 nm/s indicating that density difference plays only a negligible influence on the capsule morphology.

The second feature to explain is the crater-like texture of the thicker part of the polymer shell. These craters arise from the evaporation of very small hexadecane droplets at the polymer-water interface. The question is why they are there? For initial compositions above the green line in Figure 4.8, hexadecane droplets are predicted to separate out in a continuous polymer-rich phase. If these droplets do not all diffuse towards the oil core before the polymer shell gels, they may remain trapped in the polymer matrix. The wetting arguments above would predict that the HD droplets would adsorb to the interface between the polymer-rich phase and the aqueous solution, either in a pseudo-partial wetting state (i.e. covered with a thin polymer film) early in the drying process when $S > 0$ or in a partial wetting state (i.e. with no polymer film coating the HD-water interface) later in the drying process when $S < 0$. The observation that no craters are observed on the internal wall of the capsule argues against the oil droplets simply being randomly trapped in the fast-drying polymer shell and in favour of a thermodynamic explanation in terms of wetting at the polymer-water interface.

The third feature I noted was the small polymer beads on the inside of the capsule wall in the broken capsule in Figure 4.10(c). This formulation lies below the green line in Figure 4.8(c) and so polymer-rich droplets would be expected to phase-separate from an HD-rich phase. If these droplets do not have time to diffuse to the polymer–oil boundary before they gel, they remain as tiny polymer beads that ultimately attach themselves to the capsule wall when the HD evaporates. Note that the larger diameter of the polymer-rich droplets compared to individual polymer molecules leads to a lower diffusion coefficient and higher Peclet number.

In the discussion up to now, I have assumed that the droplet phase separates when it crosses the binodal. Figure 4.11 shows a set of images illustrating the evolution of a cast drying emulsion droplet in an aqueous film. The emulsion droplet contains 5.8 wt% HD and either 7 wt% PMMA (4i) or 1.5 wt% PMMA(4ii) in DCM solution. In the early stages of evaporation, the emulsion droplet appears clear. As DCM evaporates, the droplet shrinks and suddenly appears cloudy, internally containing various tiny droplets, which is consistent with the idea that the concentration of PMMA and HD are approximately uniform within the droplet prior to phase separation. As DCM evaporates further, these tiny internal droplets coalesce rapidly and grow into bigger droplets. After the last drying of good solvent, a solid microcapsule is formed.

I note that, when the droplet composition reaches the phase boundary, the composition in figure (4.12i) is at the polymer-rich side and in figure (4.12ii) is at the HD-rich side.

The sudden appearance of a large number of small droplets that then coarsen could be due to simultaneous nucleation of a large number of droplets but is reminiscent of a different type of phase separation. Nucleation and growth occurs when the free energy of a single phase as a function of concentration is concave. The system is stable with respect to small fluctuations in concentration but unstable with respect to large changes: phase separation can only occur via nucleation of a phase with a significantly different composition from the continuous phase, with this difference increasing the further the system is from the critical point. Consequently the system is metastable with the metastability increasing with distance from the critical point. At a composition sufficiently far from the binodal, the free energy function becomes convex and the system is now unstable with respect to small fluctuations. Any random local fluctuations of composition will spontaneously phase separate from one phase to two coexisting phases, i.e., a solvent-rich phase and a polymer-rich phase throughout the phase. This mode of phase separation is known as spinodal decomposition (see Figure 4.11(iii) and 4.12). Due to the fast evaporation of low-boiling DCM inside the emulsion droplet, there may be insufficient time for binodal decomposition to occur before the composition reaches the spinodal, at which point spinodal decomposition takes place. The ternary phase diagram that I constructed only provides information about binodal and therefore does not predict when phase separation will take place by spinodal decomposition. However, it does still predict the compositions to which the phases evolve as the two-phase system coarsens and their relative volumes, which provides an indicator of which of the two phases will be continuous.

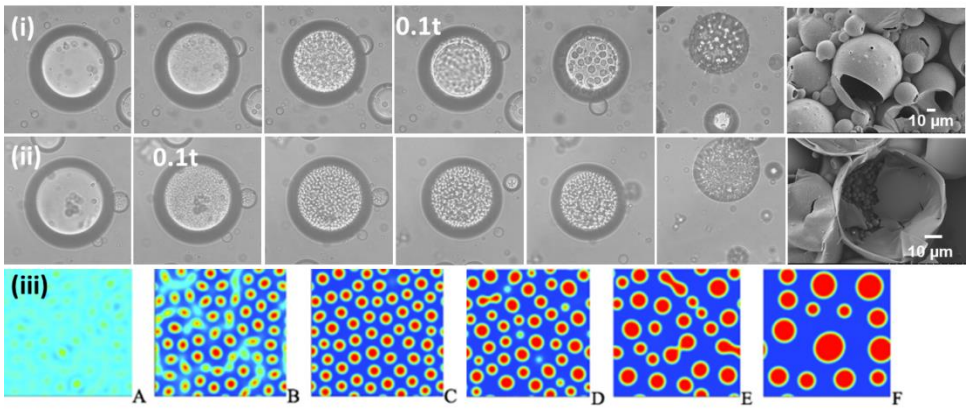

Figure 4.11. Optical micrographs and schematic diagrams showing the spinodal decomposition process of a cast drying of an o/w emulsion produced by hand shaken, (i): 7 wt% PMMA, 5.8 wt% HD in DCM; (ii): 1.5wt% PMMA, 5.8 wt% HD in DCM; 0.1t means one tenth of the time from phase separation to complete drying; (iii) schematic cartoons representing spinodal decomposition process. The drawing of figure 4.11(iii) is based on ref [96] with copyright permission obtained.

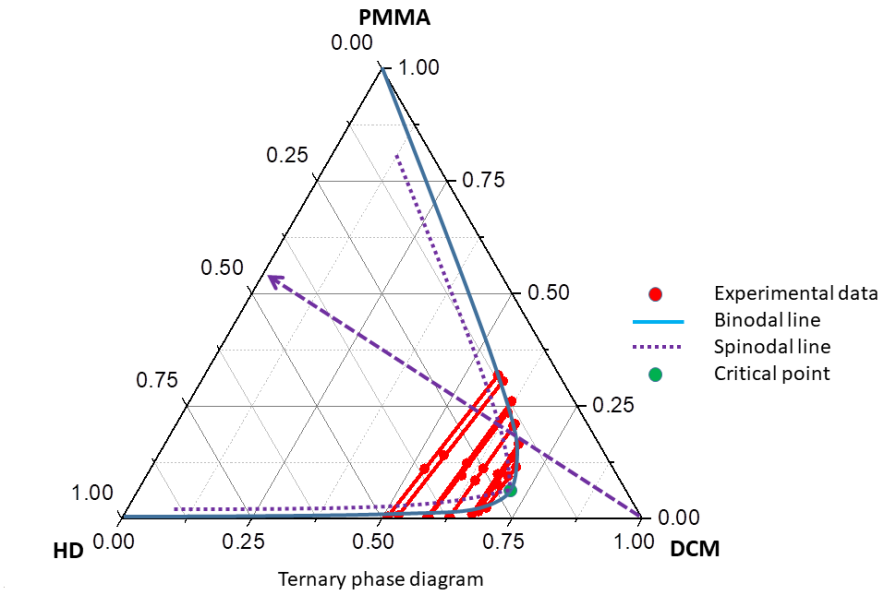

Figure 4.12. Schematic representation for the binodal and spinodal line in the ternary phase diagram. Note that the location of the spinodal line is illustrative and has not been determined in this work.

4.2.3 Influences of emulsion droplet size

In the previous section, I have shown that large emulsion droplets show complex morphologies and have proposed a theoretical explanation for the observations. Previous reports by Deng et al [35] with smaller droplets showed the formation of microcapsules so I also studied smaller droplets to seek to understand the difference between these results.

Particle size can be readily tuned through variation of solute (i.e. PMMA and HD), concentration or initial emulsion droplet size. The initial concentration must be in the one-phase region of the ternary diagram, where the solute concentration is relatively low, and the elasticity of the polymer solution must be sufficiently low that an emulsion can readily be formed. Consequently, I adopted the latter method, with an approximately constant total solute concentration and a variation of the initial emulsion droplet size. DCM solutions containing 1 wt% PMMA and 1 wt% HD were used as the oil phase, and emulsified with aqueous solutions of 0.1 wt% PVA to prepare emulsions. As reported previously, a polydisperse mixture of particles with an average diameter ranging from 2 μm to hundreds of microns can be made by homogenizer. The average diameter of particles is determined by the shear forces. Monodisperse particles with a smaller diameter from 1 μm to 2 μm can be readily produced by microfluidics. These emulsions were then allowed to dry in a puddle of 0.1 wt% PVA solution on a plasma-treated coverslip.

Figure 4.13 shows the average diameters of microcapsules approximately 30–100 μm (a), 4–8 μm (b), and 1 μm (c), respectively. Acorn-like capsules were observed in deposits of the largest capsules (a) with a cratered shell on the thick domain, which covered the larger part of the surface, and smooth shell on the smaller thin-layer domain. Medium (b) and small (c) capsules both have smooth shell all over the surface and are more spherical. The absence of craters in the smaller capsules can be rationalised in terms of the thickness of the polymer shell. The smaller capsules have a thinner polymer shell which makes it easier for hexadecane droplets to diffuse towards the oil core before the viscosity of the polymer is so high that diffusion of droplets is frozen. The absence of HD drops in the polymer shell, gives rise to a smooth HD-free shell after complete removal of DCM.

Most of the medium capsules still show an acorn-like morphology; the occasional capsule that looks spherical may just have the thin-shelled domain on the underside where it is hidden from view (Fig 4.13(b)). Conversely, only a few of the 1-μm capsules show a small, thin domain at one pole of the particle. Given that the thermodynamics of wetting are independent of particle size, I infer that the more uniform morphology of the smaller

capsules is a kinetic phenomenon. The larger the initial droplet, the longer the evaporation time, which provides more time for polymer shell to reorganize into the non-uniform domains characteristic of pseudo partial wetting of the polymer film over the o/w interface.. This argument would suggest that microcapsules produced by inkjet printing rather than cast-drying would be even more likely to have uniform shells since the drying time is faster.

These images have shown that smaller emulsion droplet size favours the formation of spherical core-shell microcapsules, with a smooth polymer shell surrounding a liquid HD core of the microcapsule. This morphology is desired in controlled release of cargoes and functional species to give a steady long-lasting release rate.

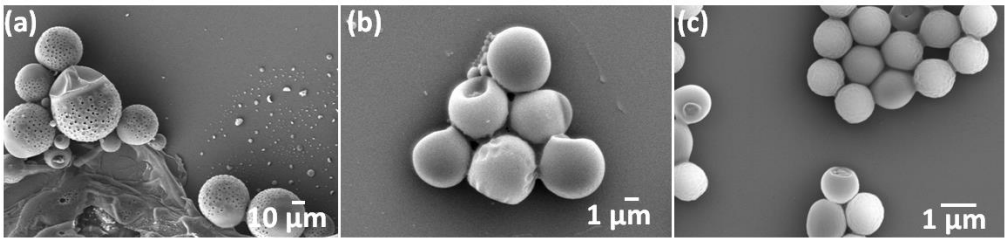

Figure 4.13. SEM images of deposits from emulsions containing 1wt% PMMA and 1wt% HD in the oil phase with different size of initial oil droplets. Deposits with PMMA-shell and HD-core microcapsules with diameters ranging from (a) 30–100 µm, (b) 4–8 µm and (c) 1 µm were observed.

4.2.4 Influence of ratio of PMMA to HD

Shell thickness is an important parameter for the core-shell microcapsules: for example, the shell thickness of the microcapsule is related to the rupture strength of the microcapsule as well as the release rate of encapsulated cargoes or functional species. SEM images of the capsules from emulsions prepared with an oil phase containing a 1 wt% mixture of PMMA and HD with varied PMMA/HD ratios ((a) 1:0, (b) 4:1, (c) 2:1, (d) 1:1, (e) 1:2, (f) 1:4) are presented in Figure 4.14. In the absence of HD in the initial composition, there is lots of wrinkling on the PMMA capsule surface. As DCM evaporates, the polymer become viscous and forms a viscoelastic shell before complete removal of DCM. As DCM further evaporates, the droplet shrinks and buckles the polymer shell. With a high PMMA/HD ratio (4:1), spherical particles with a cratered surface are observed, which can be explained by incomplete phase separation within the emulsion droplet where the phase separation of small HD-rich droplets were hindered by a bulk viscous polymer-rich phase with high PMMA

concentration. According to the ternary phase diagram, the droplet composition reaches the binodal boundary at 37.5 wt% DCM/ 50 wt% PMMA/ 12.5 wt% HD, confirming the solution has been very viscous just before phase separation. Consequently, various small HD droplets were trapped in a PMMA matrix after drying. When reducing the PMMA/HD ratio to 2:1, some acorn-like capsules appear, though in the main spherical capsules are observed. A further reduction in PMMA/HD ratio (1:1 (figure 4.14d), 1:2 (figure 4.14e), 1:4) (figure 4.14f) results in acorn-like capsules dominating the capsule morphology. This is probably due to reduction of oil phase viscosity with lower polymer viscosity, facilitating complete phase separation and non-uniform distribution of polymer-rich phase surrounding the HD-rich phase core. More collapsed microcapsules were observed under SEM imaging as the content of HD increased, since a thinner polymer shell weakens its rupture strength. Besides, as shell thickness reduces further, smooth shells are observed throughout the droplet surface (figure 4.14e, 4.14f) as nearly all HD has migrated to the inside core through the very thin polymer shell, leaving no craters in the shell.

A lower PMMA/HD ratio is desirable for the generation of core-shell microcapsules since the continuous phase will be relatively dilute HD-rich solvent, which favours phase separation of PMMA-rich droplets from the bulk phase to the o/w interface. Note that location of the critical point means that even with excess HD I still get polymer separating out as the discrete phase (up to the ratio at the critical point). Spinodal decomposition means that the thermodynamic predictions may not be realized. Besides, less PMMA means a thinner polymer shell, which contributes to the mass exchange between the polymer-rich shell and HD-rich core during the latter stages of phase separation, resulting in a relatively smooth polymer shell and pure HD core. Otherwise, when a highly viscous polymer solution is chosen as continuous phase, the motion of both phases within the emulsion droplet would be hindered, leading to a porous structure with small HD droplets embedded in a PMMA matrix due to incomplete phase separation. On the other hand, a very thin shell is not strong enough to withstand the capsule structure. Thus HD/PMMA ratio should be optimised at a relatively high ratio range to make a uniform microcapsule.

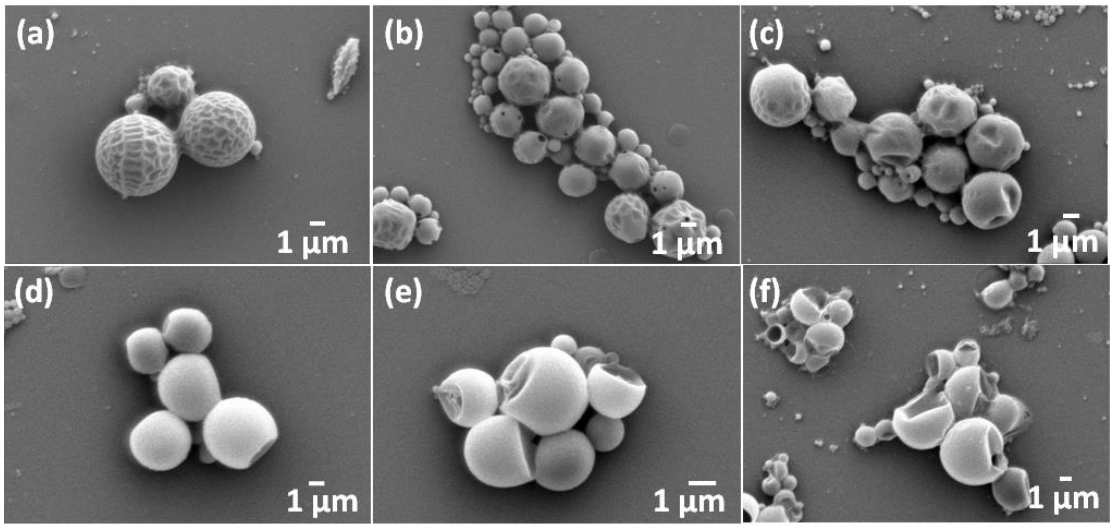

Figure 4.14. Morphology of PMMA/hexadecane particles from cast drying of emulsion containing a 1 wt% mixture of PMMA and hexadecane in the dispersed phase with varied ratios: (a) 1:0, (b) 4:1, (c) 2:1, (d) 1:1, (e) 1:2, (f) 1:4.

4.2.5 Effect of evaporation time on capsule morphology

The evaporation rate of the discrete phase depends on the thickness of the continuous phase through which the DCM has to diffuse. Consequently the thickness of the continuous phase has an impact on the phase separation process and the morphology of microcapsules after drying. Figure 4.15 compares the morphology of particles formed from emulsion droplets by cast drying (a) and inkjet printing (b). The typical evaporation time for emulsion droplets is 10 mins for (a), and 2 s for (b). Core-shell capsules are observed at both evaporation rates, but the particles formed at a low evaporation rate were more spherical in shape and smoother in shell. The particles formed at a high evaporation rate show a less regular particle with the thin polymer shell buckled. The features arise from embedded HD droplets (as opposed to lenses at the polymer-water interface), which contained DCM – when the DCM evaporated the thin polymer shell buckled (like I saw in the pure polymer).

First the difference in particle shape can be rationalised by interaction forces between particles. The slow evaporation rate gives more time for emulsion droplets to transform into solid particles before they are compressed under capillary forces with their nearest neighbours. However, the facetted sides of particles in figure 4.15 indicate the particles are still soft when they are compressed together under the inward capillary forces. In our previous study particles formed at a high relative humidity (RH) yielded a more spherical

shape, while those dried at a low RH produced a less regular structure with facetted sides, which is consistent with the idea that a low evaporation rate contributes to the formation of smooth-shaped particles.

Second the difference in shell morphology can be explained by phase separation. Particles formed by cast drying have sufficient time for the HD-rich phase to migrate toward the centre forming an oil-core and PMMA-rich phase to spread over the o/w interface resulting in a pure polymer-shell. On the contrary, the particles formed by inkjet printing yields a viscous-elastic polymer shell before the HD-rich phase have moved inward, thus ceasing the phase separation and effectively freeze the HD-rich phase in the polymer shell.

As discussed above, I argued that in the cast drying case, reducing the droplet size tends to minimise the pseudo partial wetting effect, as less evaporation time tends to decrease the rearrangement of the initial uniform shell. Indeed, there is no evidence in Figure 4.15(b) of acorn-shaped capsules. However, there are also disadvantages to rapid evaporation in inkjet printing: if the continuous polymer phase becomes highly viscous before HD droplets have had time to diffuse to the centre and coalesce, phase separation may be incomplete with some HD droplets embedded in a PMMA matrix. This study shows the importance of controlling the evaporation time within a proper range, resulting in a complete phase separation and freezing of the structure before redistribution of polymer shell.

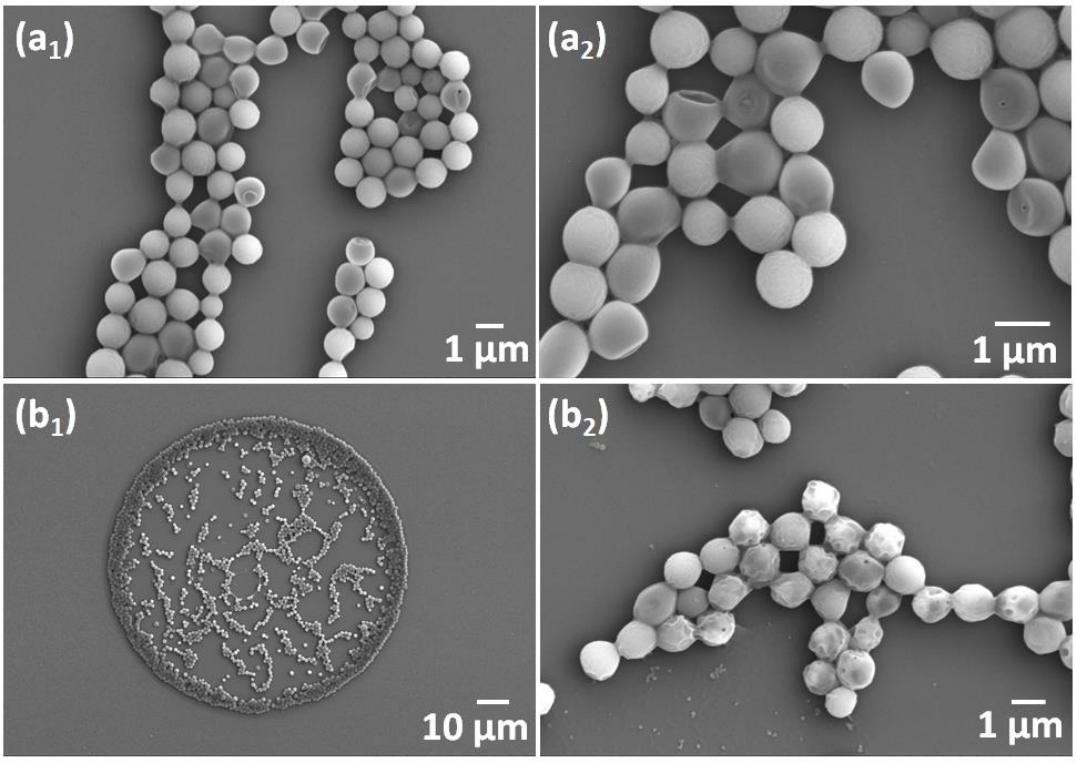

Figure 4.15. SEM images of deposits from emulsion (PMMA, 0.05 wt%, HD 0.05 wt%) by (a) cast drying and (b) inkjet printing. Core-shell shaped microcapsules are observed at both conditions.

4.2.6 Internal structure of microcapsule

To investigate the internal structure of the microcapsules, and to estimate their shell thickness, the inkjet-printed microcapsules were investigated in a FIB/scanning electron microscope dual beam system.

Figure 4.16 shows a cross-sectional image of microcapsules produced from emulsion with 0.5 wt% PMMA and 0.5 wt% HD in the oil phase. Although the capsule deforms against the platinum protection layer, an evident core-shell structure for the capsule was observed. The shell thickness of the selected microcapsules in figure 4.16a_1 are quite variable, which is a bit of a surprise since I would expect the initial compositions to be uniform. Possibly reason is the indistinct boundary between the edge of the cross section and the adjacent surface of the microcapsules, giving rise to inaccurate measurements. More measurements with a quantitative comparison of the microcapsule geometry between the theoretical calculations and experimental data will be beneficial in the future research.

Other evidence that the microcapsules contain HD is demonstrated in the sequence of images in Fig 9b. During SEM investigation, the electron beam was left at the same location to increase the local heating, resulting in the melting of the polymer shell. This secondary electron image indicated the microcapsule collapsed and the oil was ejected from the capsule core, forming a puddle alongside the capsule remnant. It is worth noting that the low volatility of the HD means that it takes some time to evaporate even in the vacuum of the SEM chamber.

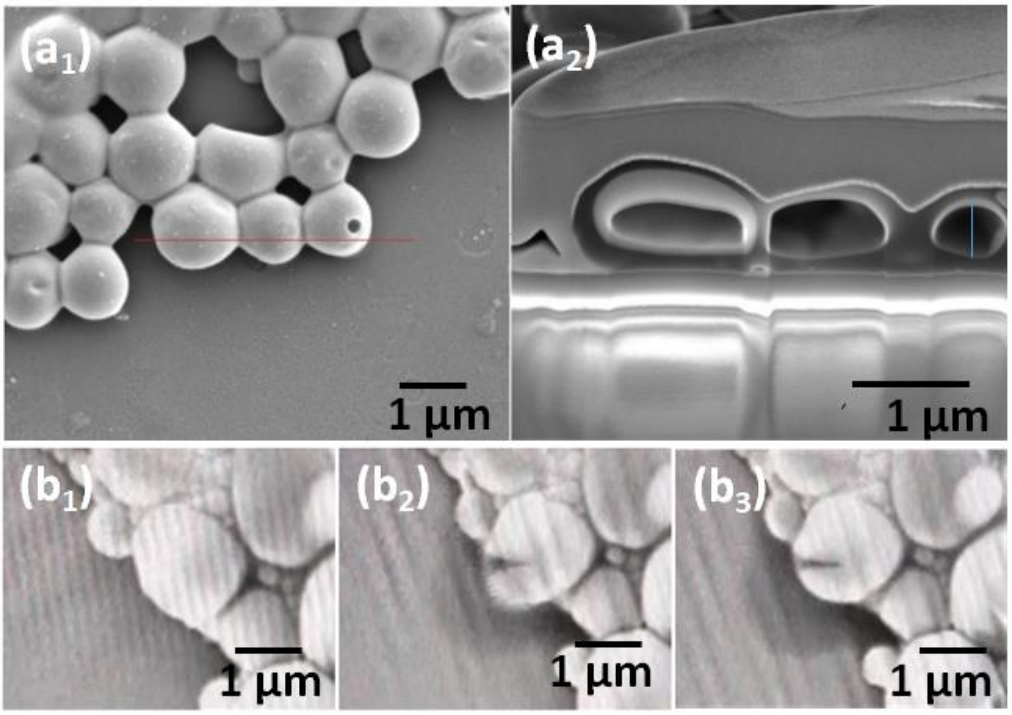

Figure 4.16. (a) surface morphology (a_1 ,by SEM) and cross-sectioned image (a_2, by FIB) of the microcapsule from emulsions containing 1 wt% HD and 1 wt% PMMA in the oil phase. (b) A set of images (b_1, b_2, b_3) extracted from a video indicate the evolution of capsule rupture during SEM imaging. Once the electron beams start to focus on the selected regimes in figure 4.16b, it takes 5~20s for the rupure process.

To confirm the poor solvent has been loaded into the liquid core of the microcapsules produced by inkjet printing of emulsions, I adopted an elemental analysis of the microcapsules using EDS [97-102], as shown in Figure 4.17. 1 wt% of bromohexadecane and

1 wt % of PMMA were pre-dissolved in DCM as the oil phase and then emulsified with PVA aqueous solution to produce the bromohexadecane-loaded microcapsules. Figure 4.17 a-d represent the sample, C element, (c) Br element, and (d) Si element, respectively. The elemental map of C, Br and Si element fit into the sample morphology with C, Br elements in the microcapsules and with Si element outside of the microcapsules, which indicates the poor solvent bromohexadecane have been loaded into the inner core rather than spread over the surface. The point ID test inside the microcapsules also shows that Br element was detected in the internal core of the microcapsules. Further line scan in figure 4.18 compares the elemental distribution inside and outside of the microcapsules, the red line and blue line represent the distribution of element C and Br, respectively: Both elements show two peaks at the locations of microcapsules, showing a good agreement with the map analysis in figure 4.17.

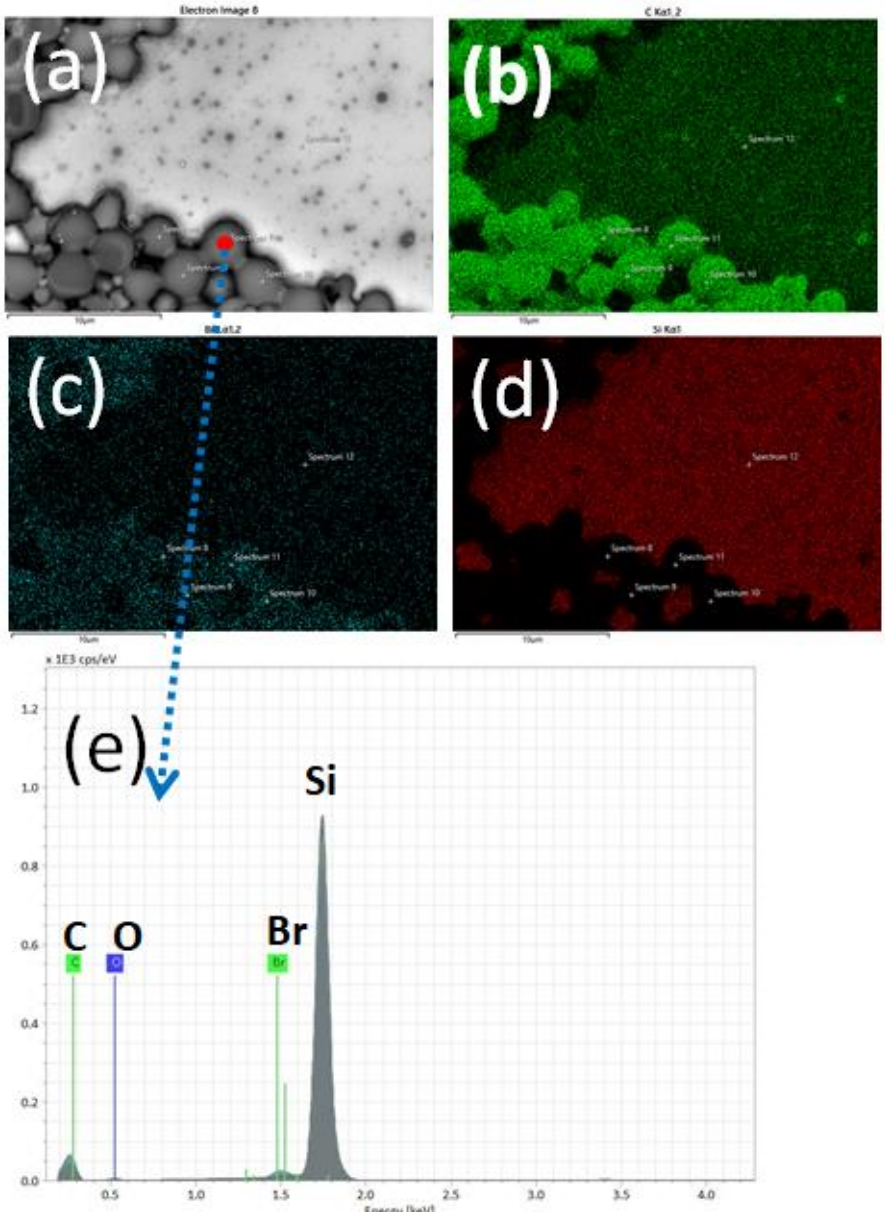

Figure 4.17. EDS element map analysis of bromohexadecane-loaded microcapsules showing: (a) electron image of microcapsules, and EDS elements maps of (b) C element, (c) Br element, and (d) Si element. (e) Point identification of EDS element analysis of the bromohexadecane-loaded microcapsules. This point on the sample was selected as the red dot in figure 4.17a. The peaks of C, O, Br and Si are illustrated in figure 4.17e, respectively.

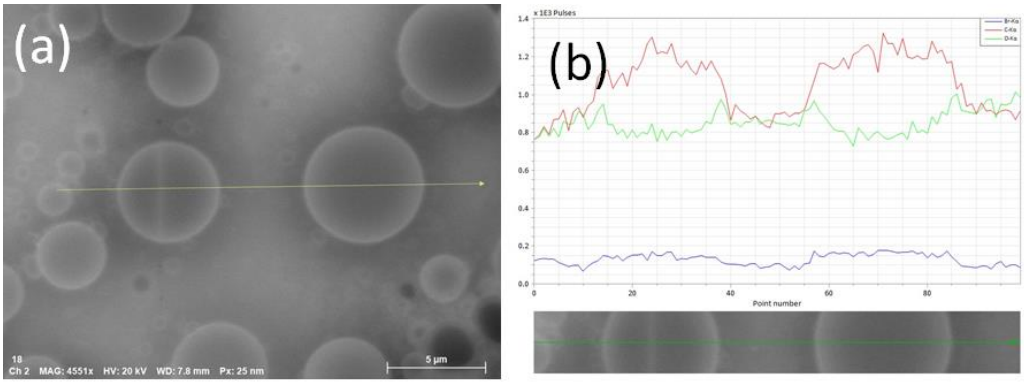

Figure 4.18. Line scans of the microcapsules produced by emulsions containing 1 wt% of bromohexadecane and 1 wt% of PMMA in DCM, (a) represents BSE image of the dry deposits on Si substrates; (b) represents the chemical distribution along the scanned line, the red line indicates element C, the green line indicates element O and the blue line represents element Br.

4.3 Conclusion

In this chapter, I characterised the three-component phase diagram for PMMA / dichloromethane/ hexadecane mixtures in order to improve our understanding of how microcapsules form in emulsion solvent evaporation. I have explored the effect of droplet size and oil composition on the success of the method. Smaller emulsion droplet size favors the formation of spherical core-shell microcapsules, with a smooth and uniform thickness of polymer shell surrounding a pure liquid HD core inside the microcapsule. Lower PMMA/HD ratio is desirable for the generation of core-shell microcapsules since the continuous phase will be relatively dilute HD-rich solvent, which favours phase separation of PMMA-rich droplets from the bulk phase which can then diffuse through a low viscosity HD-rich phase to the o/w interface. The particles formed at a low evaporation rate were more spherical in shape and smoother in shell, while particles formed at a high evaporation rate show a less regular particle which may arise from multiple small droplets of HD being embedded in a PMMA matrix.

5. Fabrication of hierarchical porous materials with macro-meso structure by inkjet printing of emulsions produced by microfluidics

Abstract

Emulsion solvent evaporation is a versatile approach for the preparation of polymeric particles from emulsions in which the discrete phase evaporates preferentially. In Chapter 3, I have shown that this method can be combined with inkjet printing of monodisperse emulsions to produce monolayers of uniform polymeric particles. Here I demonstrate this strategy can be used in the generation of hierarchical "Murray materials" with multi-scale interconnected pores by introducing silica nanoparticles in the discrete phase. A continuous monolayer of well-defined, hexagonally packed silica microspheres with hierarchical macro-meso porous structure is obtained. The porosity of the Murray material can be readily tuned by varying the size of the primary silica nanoparticles. Factors affecting the morphology of the deposit pattern have been explored. This study uses solid silica nanoparticles dispersed in the discrete phase as a model system to produce macro-meso porous material with two-scale interconnected pores, but the strategy can be generalized to porous nanoparticles for the production of three-level porous Murray material with pores on the macro, meso and micro scale.

5.1 Introduction

In nature, biological organisms have developed hierarchical porous networks during evolution by natural selection [103-113]. These hierarchical porous structures involve multi-scale pores and well-defined pore size ratios to minimise transport resistance and achieve optimum transfer efficiencies throughout the entire system, as can be commonly seen in many organisms, such as plant stems, leaf veins and vascular and respiratory systems [114-123]. Introducing these natural hierarchical structures into synthetic materials with multi-scale pores enables enhanced mass transfer and reaction rates. Therefore, such hierarchical porous materials have attracted increasing interests in industrial applications, such as self-healing materials, Li-ion batteries, gas sensors and photocatalysis [124-135]. Synthetic materials with pore-size ratios mimicking those found in nature are known as Murray materials.

Many approaches have been developed to manufacture Murray materials, including solid template-based methods and evaporation-driven self-assembly (EDSA) of nanoparticles in suspensions [136-141]. Each method has its limitations and has been optimized for different

applications. The silica or polymer template-based method requires the removal of the template. The separation process involves extra processing step and harsh reaction conditions, such as high temperature or use of hydrogen fluoride, which may decompose the porous materials, leading to limited choice of material types [136-139]. The evaporation-driven self-assembly (EISA) method allows the production of vascularized porous networks with macro-meso-micropores under room temperature and atmospheric pressure and avoids the use of corrosive acid. However, the distribution of macropores of the porous networks by EISA method is strongly affected by the concentration of nanoparticles and the choice of solvent. The inter-particle mesoporisity is unstable due to the cast drying of nanoparticle suspension during the EISA process [140-141].

Evaporation of a bulk dispersion of colloidal particles on a substrate to design desired patterns can be challenging unless a template is used. The drops of dispersions can be deposited onto substrates to develop well-defined patterns (i.e., arrays of dots, lines and large-scale patterns) via inkjet printing. Compared with templated EISA strategy, inkjet printing possesses attractive features including sufficient use of inks, precise control over patterns, no contact with substrates and easy scale-up. Thus inkjet printing has been widely used as a manufacturing technology in applications such as graphics, conducting organic electronic devices, biological samples for high throughput micro-assays and organic light-emitting diodes [142-152].

In chapter3, I have demonstrated that inkjet printing of oil-in-water emulsions onto substrates can generate uniform deposits of polymeric particles [153]. In this strategy, polymers and other non-volatile components are dissolved in the discrete phase of the oil-in-water emulsion. The organic solvent is chosen to be more volatile than the continuous phase so that the preferential evaporation of the discrete phase leads to polymeric particles. Depending on the solutes used and their phase behaviour, a wide variety of morphologies can result, such as solid polymeric particles, core-shell microcapsules and Janus particles. Chapters 3 and 4 demonstrate that the same approach can be applied with monodisperse emulsions produced in a microfluidic chip, giving rise to monolayers of uniform polymeric particles.

The purpose of this chapter is to demonstrate a strategy to prepare hierarchically macro-mesoporous material with tuneable pores by inkjet printing monodisperse emulsions containing silica nanoparticles dispersed in the discrete phase. I first show emulsions containing silica nanoparticles dispersed in the discrete phase evaporate in a cast film and

form monodisperse silica microporous particles that self-assemble into hexagonal arrays with macro-pore structures. I then show these emulsions can be inkjet printed to form a monolayer of closely packed porous networks with interconnected macropores and mesopores. Depending on the surface functionalities of the silica nano-particles, both oil-in-water and water-in-oil emulsions are applicable for this strategy. These M-M patterns are repeatable with silica nanoparticles of a range of sizes. Finally, I discuss the prospects for manufacturing more complex hierarchically porous materials, like Macro-Meso-Micro structures by introducing porous nanoparticles as the primary building blocks.

The novelty of this chapter is to include nanoparticles with different surface functionalities in the strategy of inkjet printing emulsions and produce Murray materials with multi-scale pores. Besides, the choice of emulsions is successfully extended to water-in-oil emulsions, which is benefical for industrial use, as high-boiling point solvents are favourable in practical use.

5.2 Results and discussion

5.2.1. Preparation of o/w emulsion by microfluidics and cast drying

The silica nanoparticles treated with acrylate coatings contain terminal $-CH=CH_2$ groups. Nanoparticles with these non-polar molecules on their surfaces will tend to remain inside the non-polar oil solvent and stick together to minimize their contact with the water molecules as DCM evaporates, forming individual porous structured particles after evaporation. Therefore, I chose DCM containing silica nanoparticles with acrylate surface as the oil phase, and SDS aqueous solution as the water phase, to produce the oil-in-water emulsion.

As I previously demonstrated in chapter 3, the flow rate ratio Qo/Qw is the primary factor for the size of the oil droplets. At a constant flow rate ratio of 0.1, highly uniform oil droplets with a size of around 14 μm were observed at the flow-focusing junction of the microfluidic chip for a range of silica concentrations (0.25 wt% – 1 wt%) and size of silica nanoparticles (30 nm and 200 nm), as is shown in figure 5.1a.

The emulsions were cast onto clean glass coverslips and allowed to dry freely under ambient conditions, forming a continuous monolayer of well-defined hexagonally packed porous silica microparticles. These porous silica microspheres are highly uniform with silica nanoparticles as the primary building blocks (figure 5.1c). The size of porous silica

microparticles depends both on the concentration of silica nanoparticles and porosity of the microparticles: the silica microparticles are porous spheres and highly uniform with the size of 3.1 $\pm$ 0.1 μm, 1.9 $\pm$ 0.1 μm and 3.2 $\pm$ 0.1 μm for the samples in figure 5.1b_1, 5.1b_2 and 5.1b_3, respectively. Figure 5.1c shows typical SEM image at higher magnification of the corresponding porous microparticles composed of 30 nm silica nanoparticles with $\sim$ 5 nm mesopores for the samples in figure 5.1c_1, 5.1c_2, and 200 nm silica nanoparticles with $\sim$ 80 nm mesopores for the samples in figure 5.1c_3.

The porosity of the silica nanaparticles can be calculated by the ratio of the microparticles and oil droplet sizes and the volume fraction of silica in the oil droplets. Taking an approximate density of silica nanoparticles of 2 g/cm^3 and DCM = 1.33 g/cm^3, then 1 wt% of silica in oil droplets refers to 0.66 volume %. Therefore, if the microparticles had zero porosity, then the microparticles would have a diameter given by (d / 14 μm)^3 = 0.0066, or d = 2.6 μm. The actual diameter is 3.1 μm so the solid fraction is (2.6/3.1)^3 = 60%. The solid fraction in close-packed spheres (fcc or hcp packing) is 74%. The jamming transition for amorphous hard spheres is ~ 64% [154]. So this calculation suggests that the packing density is close to the maximum and hence that the particles are probably not hollow (or if they are hollow, the cavity is quite small). For the samples in figure 5.1c_2, the solid fraction works out at about 67%. For the samples in figure 5.1c_3 it is 54%.

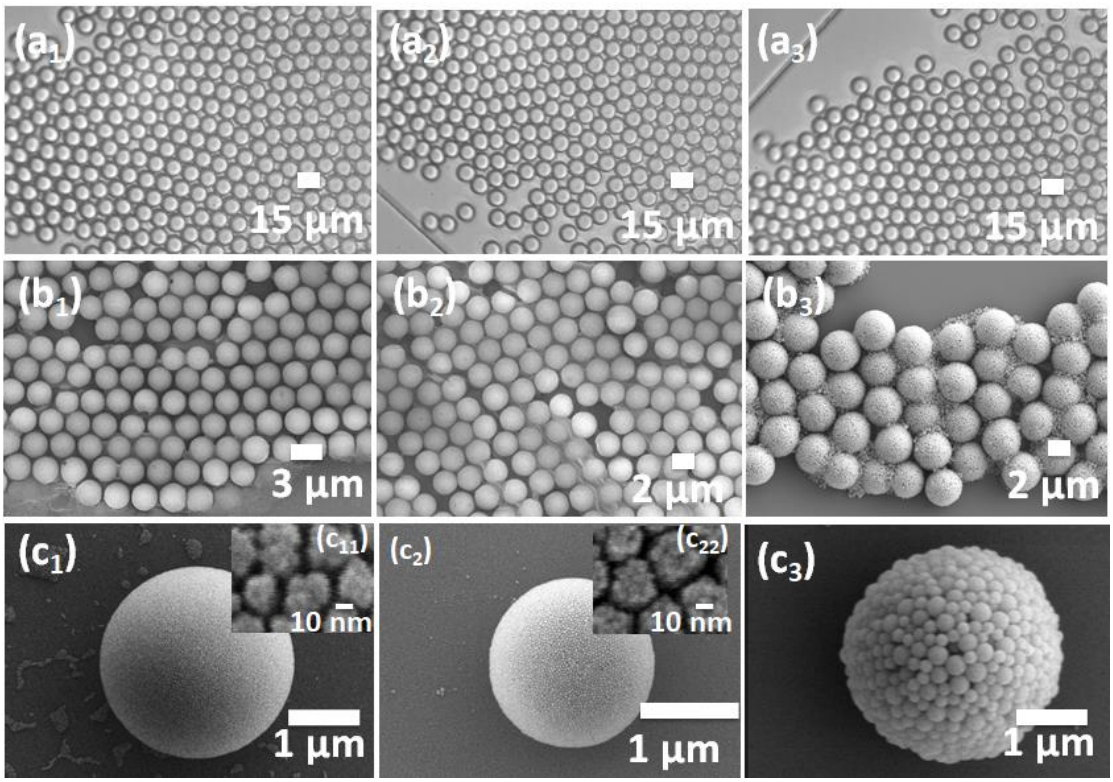

Figure 5.1. (a) Optical images of monodisperse emulsions formed from a continuous phase of 0.1 wt% SDS aqueous solution and a discrete phase containing (a_1) 1 wt%, (a_2) 0.25 wt% of 30 nm silica nanoparticles and (a_3) 1 wt% of 200 nm silica nanoparticles in DCM. The flow rate of the continuous phase and discrete phase was fixed at 4 µL min^{-1} and 0.4 µL min^{-1}, respectively; (b) SEM images of a monolayer of deposits with silica micron-sized particles from corresponding emulsions after free drying of a film of emulsions cast onto a plasma-treated glass coverslip; (c) SEM images at high resolution and magnification showing the morphology of the corresponding micron-sized porous silica particles with an overall diameter of (c_1) 3.1 µm, (c_2) 1.9 µm and (c_3) 3.2 µm. The insets c_{11} and c_{22} showed enlarged images of the 5-nm mesopores between the nanoparticles.

5.2.2. Schematic formation of Macro-Meso porous materials

Figure 5.2a shows a typical SEM image for a monolayer of densely packed particle deposit from cast drying an emulsion including a 0.25 wt% of 30 nm hydrophobic silica nanoparticles pre-dispersed in the oil phase. I observe all silica nanoparticles closely compacted in the porous microspheres. The mean gaps between the nanoparticles are around 5 nm. Figure 5.2b schematically illustrates the evolution process of the formation of porous silica

microspheres during evaporation. In figure 5.2b$_1$, at the early stages of evaporation, silica nanoparticles are well dispersed in the oil phase. As the nanoparticles are repelled from the o/w interface they are pushed towards the centre of the droplets as the o/w interface recedes. Only the nanoparticles near the surface of the oil droplet are repelled by the surface. *Pe* is not <<1, so the density of nanoparticles near the o/w interface is higher than that in the centre, as is shown in figure 5.2b$_2$ and 5.2b$_3$. So long as there is DCM between the nanoparticles, they remain mobile and do not jam and so do not form a shell. Once the last of the DCM evaporates, they then stick together due to the hydrophobic interaction (figure 5.2b$_4$).

Due to the hydrophobic nature of the acrylate surface of the nanoparticles, the particles near the initial interface are less attracted to the water phase compared with the oil phase. Surface energy effects only have a short range so there is no driving force to move the particles towards the centre once they are fully immersed in the oil phase (i.e a few nm from the o/w interface). The Peclet number for 30 nm nanoparticles is calculated as follows: If a 7-µm diameter inkjet printed droplet evaporates in, say, 2s then the characteristic velocity is $\sim$3.5 µm s^{-1}. A 15-nm radius particle has a diffusion coefficient from Stokes-Einstein of $\sim 10^{-11}$ m^2 s^{-1}. So $Pe = \frac{Ed}{D} \sim 2$. For the 100-nm radius nanoparticles, *Pe* is $\sim$8 times bigger so the interface is expected to sweep up the particles and form a jammed shell, either giving rise to hollow particles or collapsed shells. However, if the particles do not adhere strongly and remain mobile during drying they could still rearrange to form a solid sphere. These behaviours are well-known in the spray-drying applications [155]. In the case of a 7-µm diameter droplet in a cast film, the evaporation time, say, is 20s. So *Pe* < 1 for the cast films and the particles are expected to diffusive transport inward to form a solid sphere.

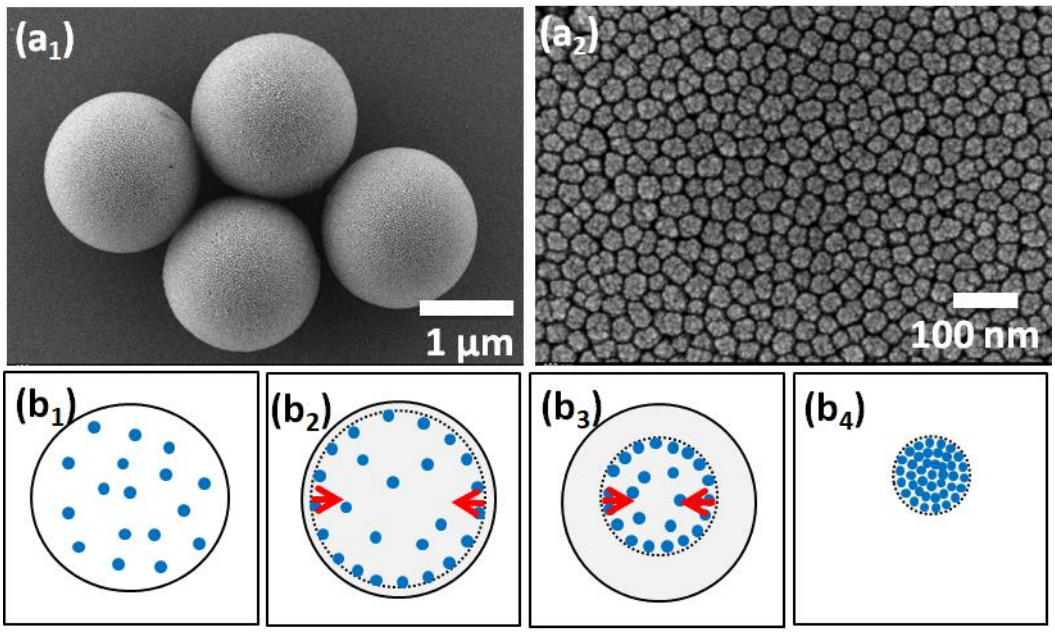

Figure 5.2. (a1) SEM images at higher resolution showing the morphology of porous microparticles composed of 30 nm silica nanoparticles: (a2) SEM images at higher magnification showing the morphologies of the 30 nm silica nanoparticles; (b1-b4) schematic graphs illustrating the evolution of an oil droplet containing nanoparticles drying in the emulsions. The solid black circle in (b) indicates the maximum extent of the initial diameter of the oil droplet, the dashed black circle in (b) shows the real-time diameter of the oil droplet during drying, and the red arrows in (b) represents the direction of the motion of the hydrophobic silica nanoparticles during the evaporation of DCM droplets.

5.2.3. Effect of silica nanoparticle size on porosity of macro-meso porous materials

The size of silica nanoparticle size not only affects the manufacturing of silica microparticles, but also determines the morphology of the porous networks. Figure 5.3 shows the consequences of using larger silica nanoparticles (200 nm in size, figure 5.3a) or smaller silica nanoparticles (30 nm in size, figure 5.3b) as the primary building blocks to prepare the porous patterns. For 200 nm nanoparticles in figure 5.3a, quite a lot of nanoparticles end up outside of the spheres, while in figure 5.3b_1 there are only a very few additional particles, a few of which are on the substrate and a few on the outside of the sphere. Note that the larger silica nanospheres are highly spherical (figure 5.3a_2) while the small silica nanospheres are relatively irregular (figure 5.3b_2), this difference in morphology affects the interactions between the neighbouring nanoparticles during packing: larger nanoparticles tend to

contact their nearest neighbours at a point, reducing the possibility of maintaining intact microspheres; as a contrast, the irregular shapes of smaller nanoparticles enables the nanoparticles to fill into the void gap, leading to successfully packing of microspheres. Nevertheless, both larger and smaller silica nanoparticles function well in the preparation of macro-meso hierarchically porous materials.

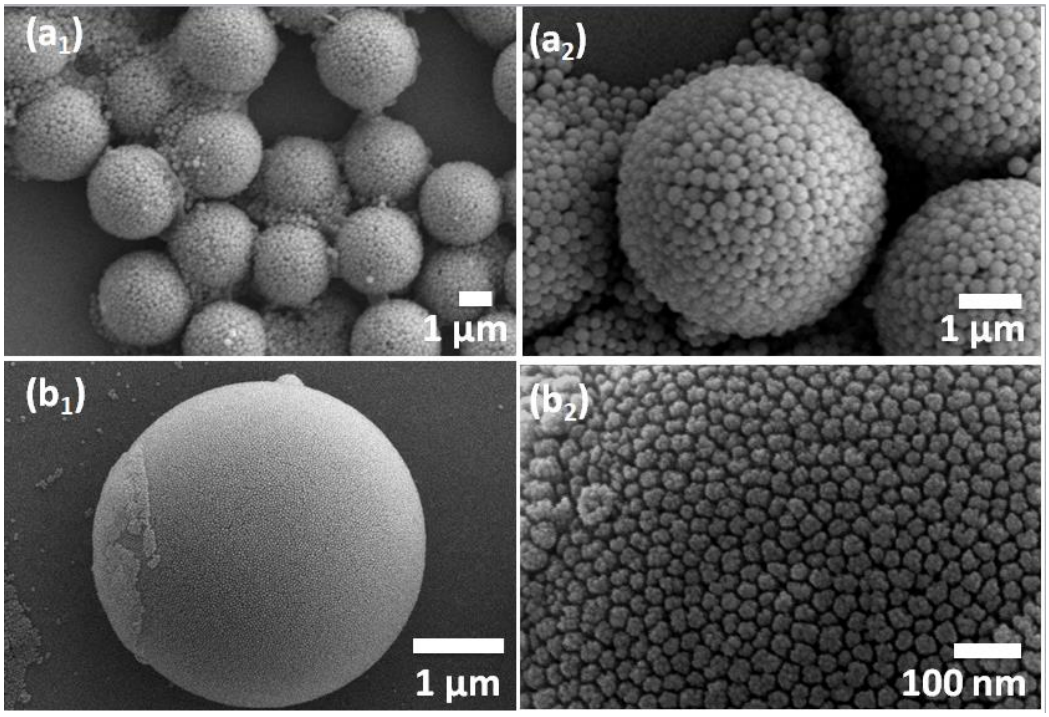

Figure 5.3. SEM images of deposits from emulsions containing (a) 200 nm and (b) 30 nm silica nanoparticles pre-dispersed in DCM as the oil phase, (a_2) and (b_2) are SEM images at higher magnification showing the morphology of the porous silica microspheres from the corresponding samples.

5.2.4. Inkjet printing of monodisperse o/w emulsion

Together with cast drying, the same o/w emulsions have been inkjet-printed continuously at 2 Hz through an 80 µm nozzle onto substrates. Different wetting properties of the underlying substrates have been demonstrated to affect the final particle distribution of the dry deposits [156-161]. Figure 5.4 compares deposits formed from emulsions with 1 wt% of 30 nm silica nanoparticles pre-dispersed in the oil phase on substrates with two different wettability: CDMOS-treated and plasma-treated. A densely packed disk-shaped deposit was obtained on CDMOS-treated glass coverslip, as is shown in figure 5.4a. By contrast, the

deposit formed on plasma-treated coverslip was sparse at the centre and a bit denser near the edge (figure 5.4b), presumably due to dragging of particles by the contact line.

The diameter of the deposit on the hydrophobic substrate is nearly the same to the initial footprint (95.2 μm and 96.8 μm), and the diameter of the deposit on the hydrophilic substrate is less than the maximum extent of the contact line (131.8 μm and 150.5 μm). I note that the initial contact radius on the hydrophobic coverslip is much less than that on the hydrophilic coverslip (96.8 μm to 150.5 μm), which reduces the distance that particles are dragged by the contact line, reducing the likelihood of pinning. Moreover, I observe that on the hydrophilic substrate there is gap between the initial contact radius to the deposit periphery (131.8 μm and 150.5 μm), indicating that particles initially near the droplet footprint are excluded from this region as the contact line moves inward. The capillary forces on the particles near the moving contact line increase the density of particles, eventually leading to pinning of the contact line.

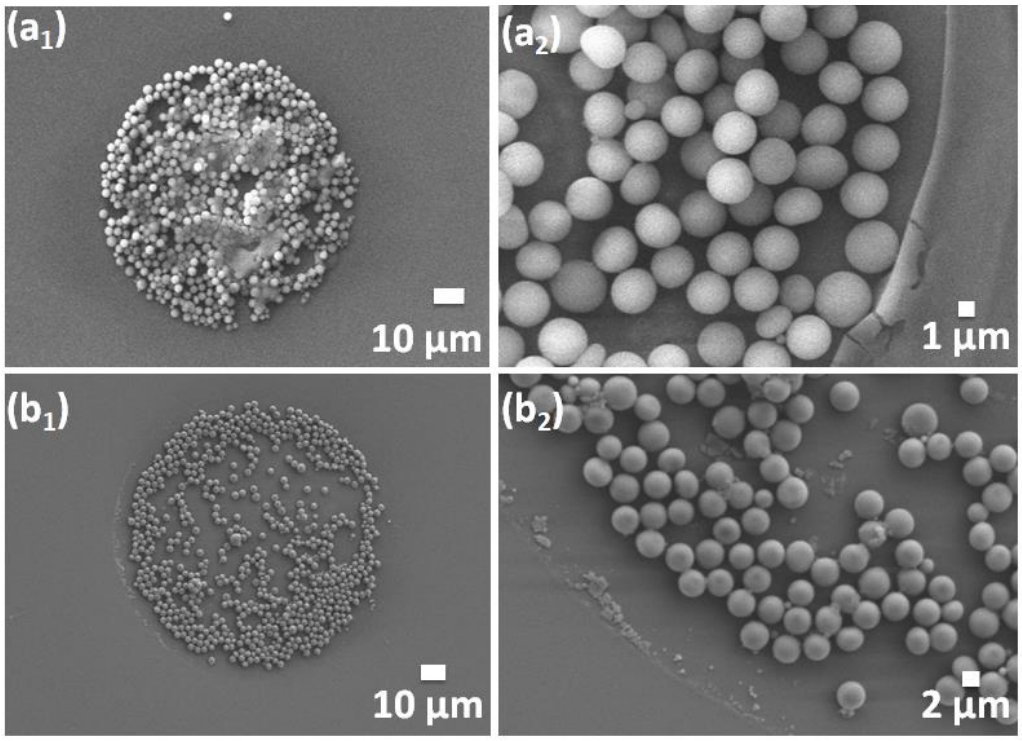

Figure 5.4. SEM images of the deposits from printed emulsion drops (o, 1wt% of 30nm silica nanoparticles in DCM, w, 0.1 wt% of SDS aqueous solution) on (a_1, a_2) hydrophobic and (b_1, b_2) hydrophilic glass coverslips.

The morphology of porous Murray materials is closely related to their transfer efficiencies. Figure 5.5 compares the morphology of porous materials from inkjet printing of o/w emulsions with 200 nm (figure 5.5a) or 30 nm (figure 5.5b) silica nanoparticles in the oil phase. The ink droplets were landed on the hydrophobic glass coverslips and dried freely. Figure 5.5a shows a circular deposit with most nanoparticles formed microspheres and the rest of the nanoparticles filled in the gap between the above microspheres or in a region near the contact line a possibly reason is smaller particles can be closer to the contact line before they deform the air-water interface. The particles from 30 nm nanoparticles in figure 5.5b are less uniform than the particles from 200 nm nanoparticles in figure 5.5a. There is 'raft' of 30-nm nanoparticles that deposits on top of the microparticles and near the contact line. This phenomenon might be explained by droplets fusing with the free surface, whereupon the hydrophobic nanoparticles would absorb to the air/water interface. Notwithstanding the small fraction of nanoparticles that are not incorporated in the microparticles, Figure 5.5 demonstrates that the pore-size ration of the porous Murray material, and hence its transfer performance can be readily tuned by varying the size of primary building blocks (i.e. 200 nm nanoparticle and 30 nm nanoparticles).

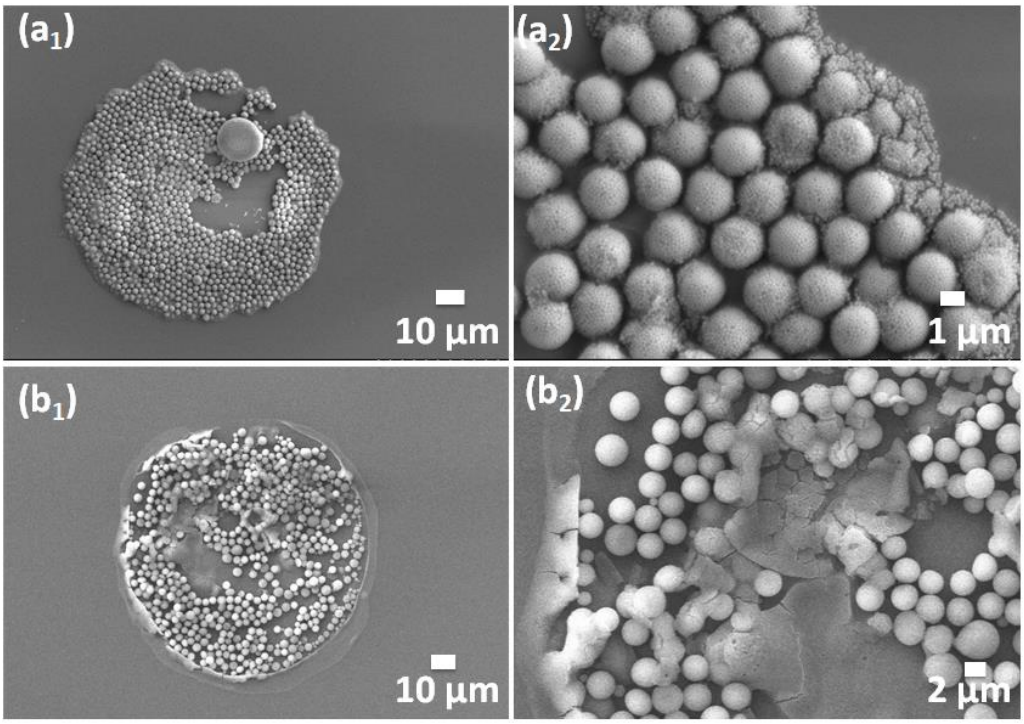

Figure 5.5. SEM images of the deposits from printed emulsion drops of (a_1, a_2) 200 nm and (b_1, b_2) 30 nm nanoparticles as the primary building blocks on the hydrophobic glass coverslips.

5.2.5. w/o emulsion

In the previous experiments we only used oil-in-water emulsions as the formulations of the liquid inks during inkjet printing, which limits the choice of solvents, polymers, etc. For example, industries favours the type of water-in-oil emulsions as the inks, as a less-volatile oil solvents reduces the possibility of nozzle clogging problem during inkjet printing process. Thus in this section, I explored the strategy of using w/o emulsion to produce the functional and structural particles. For the choice of the oil solvent for the continuous phase, the discrete phase (i.e. the aqueous phase) should be more volatile than the continuous phase (i.e. oil solvent) and appreciably soluble in the oil solvent in order that the water diffuses through the oil solvent and evaporates out through the emulsion/air interface. At 20^0C, the solubility of water in 2-pentanol is 11 wt% [162]. The problem of using microfluidics to produce w/o emulsions is the relatively high solubility of water in 2-pentanol. At a constant flow rate ratio Q_W/Q_O of 0.1, the water phase will be completely dissolved in 2-pentanol when the two phases meet at the flow-focusing junction of the microfluidic chips, leading to no formation of w/o emulsions. Instead, water phase and 2-pentanol were mixed at a ratio of 1:3 in a glass vial and sheared off by a high-speed homogenizer, to produce polydisperse w/o emulsions.

Figure 5.6 shows images extracted from videos to illustrate the evolution of both o/w emulsion and w/o emulsion cast drying on plasma-treated glass coverslips. In figure 5.6a and 5.6b I observe emulsion droplets throughout the continuous phase right after landing onto the glass coverslips, indicating no emulsion-to-dispersion has occurred before cast drying on the substrates. During the drying process, all emulsion droplets are stabilized by the corresponding surfactant without any coalescence or breakup, showing a good performance of the emulsion formulation as it dries. In figure 5.6a, due to the preferential evaporation of the discrete phase, all emulsion droplets have dried out and formed individual particles before the last drying of the continuous phase, which is consistent with the idea to form polymeric particles rather than continuous films. In figure 5.6b, as no polymer or particles have been pre-added into the emulsion droplet, as the water droplets evaporate they vanished from the video.

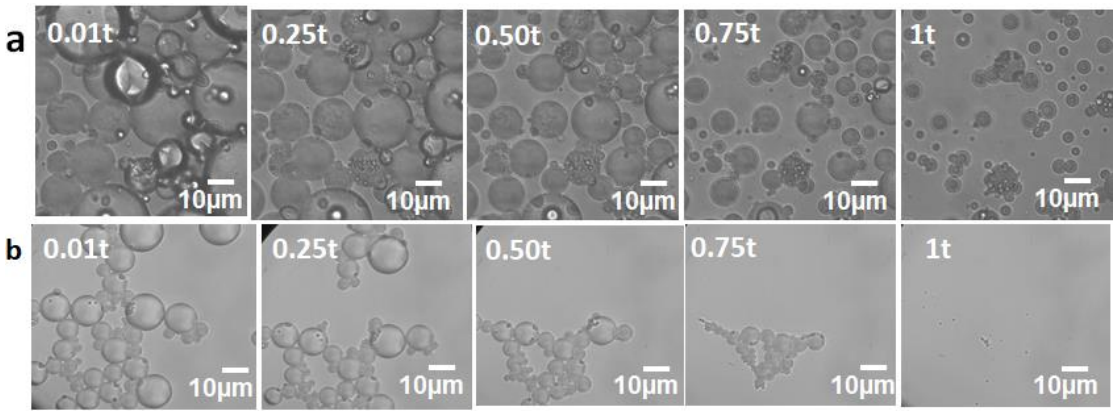

Figure 5.6. Bottom view optical microscopy images showing the evolution of a large drop of cast drying emulsion generated by a homogenizer on a CDMOS-treated glass coverslip. (a) shows o/w emulsions containing 200 nm-sized silica spheres with acrylate surface dispersed in DCM as the discrete phase; B indicates w/o emulsions including 0.3 wt% SDS aqueous solutions as the discrete phase. Symbol *t* represents the total drying time of the emulsion droplets.

Figure 5.7 shows a typical SEM image for a particle deposit from emulsions containing 1 wt% of 30 nm hydrophilic nanoparticles in the aqueous phase as the discrete phase and 2-pentanol as the continuous phase. As the w/o emulsion is produced by a homogenizer, the water droplets and the corresponding particles are less uniform than that by microfluidics (figure 5.2a). Nevertheless, in figure 5.7, all hydrophilic silica nanoparticles pre-dispersed in the water droplets have successfully formed micron-sized microspheres, demonstrating the strategy of using w/o emulsion is practical in the manufacturing of macro-meso porous materials.

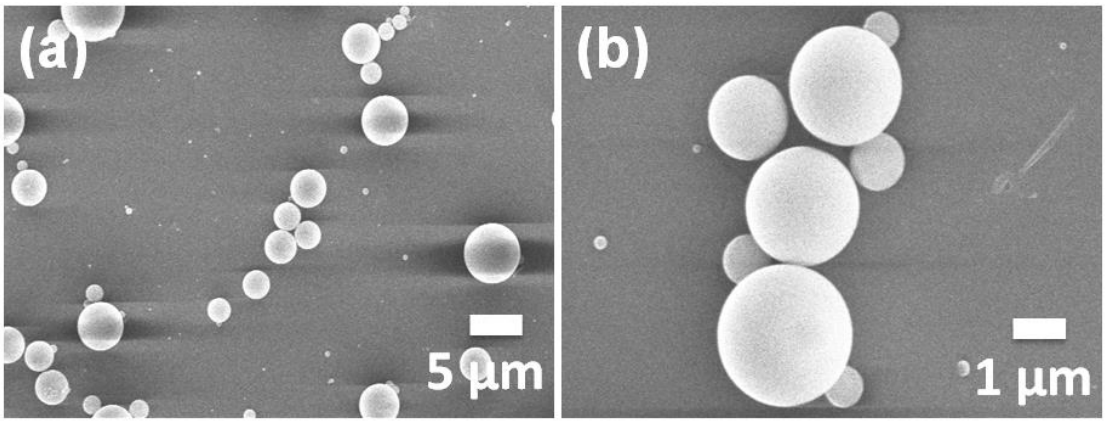

Figure 5.7. SEM images of deposits with micron-sized silica particles composed with 30 nm silica spheres from emulsions (w, 1 wt% 30 nm silica spheres with plain surface in 0.3 wt% SDS aqueous solution; o, DCM solution) after free drying of a film cast onto a plasma-treated glass coverslip. (b) SEM images at higher magnification showing the morphologies of the micron-sized silica spheres.

As there were difficulties with accessing SEM during lock-down, the images of microcapsules from water-in-oil emulsions are limited. Future work will add more results, especially individual micron-sized particles with higher magnification to show the primary building blocks of the 30 nm silica spheres. Moreover, uniform patterns of multi-scale porous materials via inkjet printing will be desired for the future research.

5.3 Conclusion

In this chapter, I have presented a method to obtain disk-shaped deposits of silica porous particles with macro-meso hierarchical structure by inkjet printing of monodisperse o/w emulsions by microfluidics. Intact silica microspheres with mesopores are formed due to the repulsion force between the non-polar silica nanoparticles and water molecules. Further evaporation of the continuous phase provides an inward capillary force to form macropores between the above microspheres. The morphology of the macro-meso hierarchical material can be readily tuned by varying the size of primary silica nanoparticles.

I extended this strategy to w/o emulsions, which generalizes the choice of silica nanoparticles from hydrophobic surface to either hydrophilic or hydrophobic surfaces. This

strategy can also be combined with porous silica nanoparticles to obtain macro-meso-micro porous Murray materials, which will be explored in the future research.

6. Concluding remarks and future research

This thesis focuses on the fabrication of functional and structured particle by inkjet printing monodisperse emulsions where the controlled evaporation of the solvents and functional cargoes leads to the formation of microstructures. Based on this idea, this thesis mainly covers three parts.

The first part is generation of monolayers of polymer particles by inkjet printing of monodisperse emulsions created in a microfluidic device. There is a small increase in the polydispersity of the particles compared to the emulsion (CoV in the particle diameter < 6% under optimised conditions) which is ascribed to break-up and coalescence of oil droplets during jetting. The polydispersity is minimised by minimising the capillary number during jetting through three strategies: increasing the nozzle diameter to reduce the shear rate, increasing the oil–water interfacial tension, and reducing the oil droplet size. The particle size is controlled by the polymer concentration in the oil phase. Relative humidity plays a minor role in the particle formation process. At low RH, the water droplet evaporates faster, and some faceting of the particles was observed due to residual solvent in the PS particles as they pack into the monolayer. The effect of the substrate wettability on the morphology of the deposit was briefly explored: well-ordered monolayers of small particles formed on hydrophobic substrates and of large particles on hydrophilic substrates. The objective of this work has been to explore the effect of process parameters on the combined microfluidic/inkjet method for generating uniform layers of particles. For this reason, I only used a single chemical system: polystyrene in DCM as the oil phase and SDS solutions as the aqueous phase. The emulsion solvent evaporation method does, however, have wide applicability in terms of polymers, organic solvent and morphology of the particles formed. It can also be used to incorporate functional cargoes. In a subsequent paper, we will explore the encapsulation of functional cargoes in the polymeric particles formed during the drying of inkjet-printed emulsions. Major benefits of combining the generation of the emulsion and inkjet printing are the reduction of nozzle clogging and avoidance of shelf-life issues since there is no need to stabilise a particle suspension against aggregation and sedimentation.

The second part is the production of microcapsules by emulsion solvent evaporation in inkjet printed drops and characterised the three-component phase diagram for PMMA/dichloromethane/ hexadecane mixtures to improve our understanding of how microcapsules form in emulsion solvent evaporation. I have explored the effect of droplet size, oil composition and emulsifier on the success of the method. Smaller emulsion droplet size favours the formation of spherical core-shell microcapsules, with a smooth and uniform thickness of polymer shell surrounding a pure liquid HD core right at the capsule centre. Lower PMMA/HD ratio is desirable for the generation of core-shell microcapsules since the continuous phase will be relatively dilute HD-rich solvent, which favours phase separation of PMMA-rich droplets from the bulk phase to the o/w interface. The particles formed at a low evaporation rate were more spherical in shape and smoother in shell, while particles formed at a high evaporation rate show a less regular particle with multiple small droplets of HD embedded in a PMMA matrix.

The last part concerned the drying of emulsions containing nanoparticles rather than polymers and is about the fabrication of hierarchical porous materials with macro-meso structure by inkjet printing of uniform nanoparticle-containing emulsions produced by microfluidics. Intact silica microspheres with mesopores are formed due to the repulsion force between the non-polar silica nanoparticles and water molecules. Further evaporation of the continuous phase provides an inward capillary force to form macropores between the above microspheres. The morphology of the macro-meso hierarchical material can be readily tuned by varying the size of primary silica nanoparticles. I further extend this strategy to w/o emulsions, which generalizes the choice of silica nanoparticles from hydrophobic surface to either hydrophilic or hydrophobic surfaces.

This strategy can also be combined with porous silica nanoparticles to obtain macro-meso-micro porous Murray materials, which will be explored in the future research. As porous nanoparticles with sub-micron pores formed inside individual nanoparticles and different surface functionalities can be purchased from commercial companies (like sigma), it is possible to use the strategy of inkjet printing of emulsions to prepare Murray materials with micron-nanometre-subnanometre scale pores. Another future plan is to explore the choice of microfluidics to produce uniform emulsions with smaller size of oil droplets inside the microfluidic chips. Possible method is to prepare microfluidic chips with smaller length scale of the flow-focusing junction, thus resulting in smaller diameter of the discrete emulsions. This strategy gives rise to a smaller shear force

on the oil droplets of the oil-in-water emulsions during inkjet printing, leading to improvements of the uniformity of the size distribution of the final structured polymeric particles and the morphology of the monolayer of the deposits.

7. References

1. Rosca, I.D., Watari, F. and Uo, M., 2004. Microparticle formation and its mechanism in single and double emulsion solvent evaporation. Journal of controlled release, 99(2), pp.271-280.

2. Ito, F., Fujimori, H., Honnami, H., Kawakami, H., Kanamura, K. and Makino, K., 2009. Study of types and mixture ratio of organic solvent used to dissolve polymers for preparation of drug-containing PLGA microspheres. European Polymer Journal, 45(3), pp.658-667.

3. Loxley, A. and Vincent, B., 1998. Preparation of poly (methylmethacrylate) microcapsules with liquid cores. Journal of colloid and interface science, 208(1), pp.49-62.

4. Pekarek, K.J., Jacob, J.S. and Mathiowitz, E., 1994. Double-walled polymer microspheres for controlled drug release. Nature, 367(6460), pp.258-260.

5. Dowding, P.J., Atkin, R., Vincent, B. and Bouillot, P., 2004. Oil core− polymer shell microcapsules prepared by internal phase separation from emulsion droplets. I. Characterization and release rates for microcapsules with polystyrene shells. Langmuir, 20(26), pp.11374-11379.

6. Dowding, P.J., Atkin, R., Vincent, B. and Bouillot, P., 2005. Oil core/polymer shell microcapsules by internal phase separation from emulsion droplets. II: controlling the release profile of active molecules. Langmuir, 21(12), pp.5278-5284.

7. Bouchemal, K.S.E.H.I.N., Briançon, S., Perrier, E., Fessi, H., Bonnet, I. and Zydowicz, N., 2004. Synthesis and characterization of polyurethane and poly (ether urethane) nanocapsules using a new technique of interfacial polycondensation combined to spontaneous emulsification. International Journal of Pharmaceutics, 269(1), pp.89-100.

8. Liu, J., Zhang, Y., Wang, C., Xu, R., Chen, Z. and Gu, N., 2010. Magnetically sensitive alginate-templated polyelectrolyte multilayer microcapsules for controlled release of doxorubicin. The Journal of Physical Chemistry C, 114(17), pp.7673-7679.

9. Taqieddin, E. and Amiji, M., 2004. Enzyme immobilization in novel alginate–chitosan core-shell microcapsules. Biomaterials, 25(10), pp.1937-1945.

10. Yu, X., Zhao, Z., Nie, W., Deng, R., Liu, S., Liang, R., Zhu, J. and Ji, X., 2011. Biodegradable polymer microcapsules fabrication through a template-free approach. Langmuir, 27(16), pp.10265-10273.

11. Hutchings, I. M., Martin, G. D., Eds.; 2013. Inkjet Technology for Digital Fabrication; John Wiley & Sons, Ltd.

12. Walther, A. and Muller, A.H., 2013. Janus particles: synthesis, self-assembly, physical properties, and applications. Chemical reviews, 113(7), pp.5194-5261.

13. Deng, R., Li, H., Zhu, J., Li, B., Liang, F., Jia, F., Qu, X. and Yang, Z., 2016. Janus nanoparticles of block copolymers by emulsion solvent evaporation induced assembly. Macromolecules, 49(4), pp.1362-1368.

14. Breslouer, O., 2010. Rayleigh-plateau instability: falling jet. Project Report.

15. Johns, A.S. and Bain, C.D., 2017. Ink-jet printing of high-molecular-weight polymers in oil-in-water emulsions. ACS applied materials & interfaces, 9(27), pp.22918-22926.

16. Deng, R., Yang, L. and Bain, C.D., 2018. Combining inkjet printing with emulsion solvent evaporation to pattern polymeric particles. ACS applied materials & interfaces, 10(15), pp.12317-12322.

17. Anna, S.L. and Mayer, H.C., 2006. Microscale tipstreaming in a microfluidic flow focusing device. Physics of Fluids, 18(12), p.121512.

18. Nisisako, T., Torii, T., Takahashi, T. and Takizawa, Y., 2006. Synthesis of monodisperse bicolored janus particles with electrical anisotropy using a microfluidic Co‐Flow system. Advanced Materials, 18(9), pp.1152-1156.

19. Okushima, S., Nisisako, T., Torii, T. and Higuchi, T., 2004. Controlled production of monodisperse double emulsions by two-step droplet breakup in microfluidic devices. Langmuir, 20(23), pp.9905-9908.

20. Link, D.R., Anna, S.L., Weitz, D.A. and Stone, H.A., 2004. Geometrically mediated breakup of drops in microfluidic devices. Physical review letters, 92(5), p.054503.

21. Deegan, R.D., Bakajin, O., Dupont, T.F., Huber, G., Nagel, S.R. and Witten, T.A., 1997. Capillary flow as the cause of ring stains from dried liquid drops. Nature, 389(6653), pp.827-829.

22. Hu, H. and Larson, R.G., 2002. Evaporation of a sessile droplet on a substrate. The Journal of Physical Chemistry B, 106(6), pp.1334-1344.

23. Picknett, R.G. and Bexon, R., 1977. The evaporation of sessile or pendant drops in still air. Journal of Colloid and Interface Science, 61(2), pp.336-350.

24 H. Hu, and Larson, R.G., 2005. Analysis of the effects of Marangoni stresses on the microflow in an evaporating sessile droplet. Langmuir, 21(9), p. 3972-3980.

25. Weon, B.M. and Je, J.H., 2010. Capillary force repels coffee-ring effect. Physical Review E, 82(1), p.015305.

26. Yunker, P.J., Still, T., Lohr, M.A. and Yodh, A.G., 2011. Suppression of the coffee-ring effect by shape-dependent capillary interactions. Nature, 476(7360), pp.308-311.

27. Bigioni, T.P., Lin, X.M., Nguyen, T.T., Corwin, E.I., Witten, T.A. and Jaeger, H.M., 2006. Kinetically driven self assembly of highly ordered nanoparticle monolayers. Nature materials, 5(4), pp.265-270.

28. Cui, L., Li, Y., Wang, J., Tian, E., Zhang, X., Zhang, Y., Song, Y. and Jiang, L., 2009. Fabrication of large-area patterned photonic crystals by ink-jet printing. Journal of Materials Chemistry, 19(31), pp.5499-5502.

29. Orejon, D., Sefiane, K. and Shanahan, M.E., 2011. Stick–slip of evaporating droplets: substrate hydrophobicity and nanoparticle concentration. Langmuir, 27(21), pp.12834-12843.

30. Talbot, E.L., Yang, L., Berson, A. and Bain, C.D., 2014. Control of the particle distribution in inkjet printing through an evaporation-driven sol–gel transition. ACS applied materials & interfaces, 6(12), pp.9572-9583.

31. Kajiya, T., Kobayashi. W, Okuzono. T, and Doi. M, 2009. Controlling the drying and film formation processes of polymer solution droplets with addition of small amount of surfactants. The Journal of Physical Chemistry B, 113(47), pp. 15460-15466

32. S. Liu, R. Deng, W. Li and J. Zhu, Adv. Funct. Mater., 2012, 22, pp. 1692-1697.

33. Zhao, Y., Cheng, Y., Shang, L., Wang, J., Xie, Z. and Gu, Z., 2015. Microfluidic synthesis of barcode particles for multiplex assays. Small, 11(2), pp.151-174.

34. Wang, J., Hu, Y., Deng, R., Xu, W., Liu, S., Liang, R., Nie, Z. and Zhu, J., 2012. Construction of multifunctional photonic crystal microcapsules with tunable shell structures by combining microfluidic and controlled photopolymerization. Lab on a Chip, 12(16), pp.2795-2798.

35. Deng, R., Wang, Y., Yang, L. and Bain, C.D., 2019. In situ fabrication of polymeric microcapsules by ink-jet printing of emulsions. ACS applied materials & interfaces, 11(43), pp.40652-40661.

36. Sun, J., Bao, B., He, M., Zhou, H. and Song, Y., 2015. Recent advances in controlling the depositing morphologies of inkjet droplets. ACS applied materials & interfaces, 7(51), pp.28086-28099.

37. Wang, J., Wang, L., Song, Y. and Jiang, L., 2013. Patterned photonic crystals fabricated by inkjet printing. Journal of Materials Chemistry C, 1(38), pp.6048-6058.

38. Hou, J., Li, M. and Song, Y., 2018. Patterned colloidal photonic crystals. Angewandte Chemie International Edition, 57(10), pp.2544-2553.

39. Kuang, M., Wang, L. and Song, Y., 2014. Controllable printing droplets for high‐resolution patterns. Advanced materials, 26(40), pp.6950-6958.

40. Singh, M., Haverinen, H.M., Dhagat, P. and Jabbour, G.E., 2010. Inkjet printing—process and its applications. Advanced materials, 22(6), pp.673-685.

41. Le, H.P., 1998. Progress and trends in ink-jet printing technology. Journal of Imaging Science and Technology, 42(1), pp.49-62.

42. Park, J.U., Hardy, M., Kang, S.J., Barton, K., Adair, K., kishore Mukhopadhyay, D., Lee, C.Y., Strano, M.S., Alleyne, A.G., Georgiadis, J.G. and Ferreira, P.M., 2007. High-resolution electrohydrodynamic jet printing. Nature materials, 6(10), pp.782-789.

43. Park, J., Moon, J., Shin, H., Wang, D. and Park, M., 2006. Direct-write fabrication of colloidal photonic crystal microarrays by ink-jet printing. Journal of colloid and interface science, 298(2), pp.713-719.

44. Sowade, E., Blaudeck, T. and Baumann, R.R., 2016. Self-assembly of spherical colloidal photonic crystals inside inkjet-printed droplets. Crystal Growth & Design, 16(2), pp.1017-1026.

45. Ding, H., Zhu, C., Tian, L., Liu, C., Fu, G., Shang, L. and Gu, Z., 2017. Structural color patterns by electrohydrodynamic jet printed photonic crystals. ACS applied materials & interfaces, 9(13), pp.11933-11941.

46. Al-Milaji, K.N. and Zhao, H., 2019. Probing the colloidal particle dynamics in drying sessile droplets. Langmuir, 35(6), pp.2209-2220.

47. Hou, J., Zhang, H., Yang, Q., Li, M., Song, Y. and Jiang, L., 2014. Bio‐inspired photonic‐crystal microchip for fluorescent ultratrace detection. Angewandte Chemie International Edition, 53(23), pp.5791-5795.

48. Boyle, B.M., French, T.A., Pearson, R.M., McCarthy, B.G. and Miyake, G.M., 2017. Structural color for additive manufacturing: 3D-printed photonic crystals from block copolymers. ACS nano, 11(3), pp.3052-3058.

49. Xia, Y., Gates, B., Yin, Y. and Lu, Y.J.A.M., 2000. Monodispersed colloidal spheres: old materials with new applications. Advanced Materials, 12(10), pp.693-713.

50. Bhardwaj, R., Fang, X., Somasundaran, P. and Attinger, D., 2010. Self-assembly of colloidal particles from evaporating droplets: role of DLVO interactions and proposition of a phase diagram. Langmuir, 26(11), pp.7833-7842.

51. Anyfantakis, M., Geng, Z., Morel, M., Rudiuk, S. and Baigl, D., 2015. Modulation of the coffee-ring effect in particle/surfactant mixtures: the importance of particle–interface interactions. Langmuir, 31(14), pp.4113-4120.

52. Guo, Y., Li, L., Li, F., Zhou, H. and Song, Y., 2015. Inkjet print microchannels based on a liquid template. Lab on a Chip, 15(7), pp.1759-1764.

53. Chatterjee, S., Kumar, M., Murallidharan, J.S. and Bhardwaj, R., 2020. Evaporation of initially heated sessile droplets and the resultant dried colloidal deposits on substrates held at ambient temperature. Langmuir, 36(29), pp.8407-8421.

54. Yin, Y., Lu, Y., Gates, B. and Xia, Y., 2001. Template-assisted self-assembly: a practical route to complex aggregates of monodispersed colloids with well-defined sizes, shapes, and structures. Journal of the American Chemical Society, 123(36), pp.8718-8729.

55. Still, T., Yunker, P.J. and Yodh, A.G., 2012. Surfactant-induced Marangoni eddies alter the coffee-rings of evaporating colloidal drops. Langmuir, 28(11), pp.4984-4988.

56. Wang, J., Hu, Y., Deng, R., Liang, R., Li, W., Liu, S. and Zhu, J., 2013. Multiresponsive hydrogel photonic crystal microparticles with inverse-opal structure. Langmuir, 29(28), pp.8825-8834.

57. Park, J. and Moon, J., 2006. Control of colloidal particle deposit patterns within picoliter droplets ejected by ink-jet printing. Langmuir, 22(8), pp.3506-3513.

58. Gao, M., Li, L. and Song, Y., 2017. Inkjet printing wearable electronic devices. Journal of Materials Chemistry C, 5(12), pp.2971-2993.Bai, L., Xie, Z., Wang, W., Yuan, C., Zhao, Y., Mu, Z., Zhong, Q. and Gu, Z., 2014. Bio-inspired vapor-responsive colloidal photonic crystal patterns by inkjet printing. ACS nano, 8(11), pp.11094-11100.

59. Liu, M., Wang, J., He, M., Wang, L., Li, F., Jiang, L. and Song, Y., 2014. Inkjet printing controllable footprint lines by regulating the dynamic wettability of coalescing ink droplets. ACS applied materials & interfaces, 6(16), pp.13344-13348.

60. Whitesides, G.M., 2006. The origins and the future of microfluidics. nature, 442(7101), pp.368-373.

61. Nie, Z., Deiss, F., Liu, X., Akbulut, O. and Whitesides, G.M., 2010. Integration of paper-based microfluidic devices with commercial electrochemical readers. Lab on a Chip, 10(22), pp.3163-3169.

62. Guo, M.T., Rotem, A., Heyman, J.A. and Weitz, D.A., 2012. Droplet microfluidics for high-throughput biological assays. Lab on a Chip, 12(12), pp.2146-2155.

63. Nunes, J.K., Tsai, S.S.H., Wan, J. and Stone, H.A., 2013. Dripping and jetting in microfluidic multiphase flows applied to particle and fibre synthesis. Journal of physics D: Applied physics, 46(11), p.114002.

64. Zhang, D.F. and Stone, H.A., 1997. Drop formation in viscous flows at a vertical capillary tube. Physics of Fluids, 9(8), pp.2234-2242.

65. Taylor, G.I., 1934. The formation of emulsions in definable fields of flow. Proceedings of the Royal Society of London. Series A, containing papers of a mathematical and physical character, 146(858), pp.501-523.

66. Lide, D.R. ed., 2004. CRC handbook of chemistry and physics (Vol. 85). CRC press.

67. Larson, R.G., 2014. Transport and deposition patterns in drying sessile droplets. AIChE Journal, 60(5), pp.1538-1571.

68. Weon, B.M. and Je, J.H., 2013. Self-pinning by colloids confined at a contact line. Physical review letters, 110(2), p.028303.

69. Israelachvili, J.N., 2011. Intermolecular and surface forces. Academic press.

70. Johnson, K.L. and Johnson, K.L., 1987. Contact mechanics. Cambridge university press.

71. Kuang, M., Wang, J., Bao, B., Li, F., Wang, L., Jiang, L. and Song, Y., 2014. Inkjet printing patterned photonic crystal domes for wide viewing‐angle displays by controlling the sliding three phase contact line. Advanced Optical Materials, 2(1), pp.34-38.

72. Yang, Y.Y., Chung, T.S. and Ng, N.P., 2001. Morphology, drug distribution, and in vitro release profiles of biodegradable polymeric microspheres containing protein fabricated by double-emulsion solvent extraction/evaporation method. Biomaterials, 22(3), pp.231-241.

73. Christopher, G.F. and Anna, S.L., 2007. Microfluidic methods for generating continuous droplet streams. Journal of Physics D: Applied Physics, 40(19), p.R319.

74. Anna, S.L., Bontoux, N. and Stone, H.A., 2003. Formation of dispersions using “flow focusing” in microchannels. Applied physics letters, 82(3), pp.364-366.

75. Link, D.R., Grasland‐Mongrain, E., Duri, A., Sarrazin, F., Cheng, Z., Cristobal, G., Marquez, M. and Weitz, D.A., 2006. Electric control of droplets in microfluidic devices. Angewandte Chemie International Edition, 45(16), pp.2556-2560.

76. Lee, W., Walker, L.M. and Anna, S.L., 2011. Competition between viscoelasticity and surfactant dynamics in flow focusing microfluidics. Macromolecular Materials and Engineering, 296(3‐4), pp.203-213.

77. McDonald, J.C. and Whitesides, G.M., 2002. Poly (dimethylsiloxane) as a material for fabricating microfluidic devices. Accounts of chemical research, 35(7), pp.491-499.

78. Squires, T.M. and Quake, S.R., 2005. Microfluidics: Fluid physics at the nanoliter scale. Reviews of modern physics, 77(3), p.977.

79. Stone, H.A., Stroock, A.D. and Ajdari, A., 2004. Engineering flows in small devices: microfluidics toward a lab-on-a-chip. Annu. Rev. Fluid Mech., 36, pp.381-411.

80. Psaltis, D., Quake, S.R. and Yang, C., 2006. Developing optofluidic technology through the fusion of microfluidics and optics. nature, 442(7101), pp.381-386.

81. Teh, S.Y., Lin, R., Hung, L.H. and Lee, A.P., 2008. Droplet microfluidics. Lab on a Chip, 8(2), pp.198-220.

82. Nguyen, N.T., Wereley, S.T. and Shaegh, S.A.M., 2019. Fundamentals and applications of microfluidics. Artech house.

83. Nisisako, T., Okushima, S. and Torii, T., 2005. Controlled formulation of monodisperse double emulsions in a multiple-phase microfluidic system. Soft Matter, 1(1), pp.23-27.

84. Chen, C.H., Shah, R.K., Abate, A.R. and Weitz, D.A., 2009. Janus particles templated from double emulsion droplets generated using microfluidics. Langmuir, 25(8), pp.4320-4323.

85. Konishi, T., Yoshizaki, T., Saito, T., Einaga, Y. and Yamakawa, H., 1990. Mean-square radius of gyration of oligo-and polystyrenes in dilute solutions. Macromolecules, 23(1), pp.290-297.

86. Orwoll, R.A. and Arnold, P.A., 2007. Polymer–solvent interaction parameter χ. In Physical properties of polymers handbook (pp. 233-257). Springer, New York, NY.

87. Sheehan, C.J. and Bisio, A.L., 1966. Polymer/solvent interaction parameters. Rubber Chemistry and Technology, 39(1), pp.149-192.

88. Etxabarren, C., Iriarte, M., Uriarte, C., Etxeberrıa, A. and Iruin, J.J., 2002. Polymer–solvent interaction parameters in polymer solutions at high polymer concentrations. Journal of Chromatography A, 969(1-2), pp.245-254.

89. Schuld, N. and Wolf, B.A., 1999. Polymer-solvent interaction parameters. Polymer handbook, 4.

90. Hirotsu, S., 1987. Phase transition of a polymer gel in pure and mixed solvent media. Journal of the Physical Society of Japan, 56(1), pp.233-242.

91. Goodsaid-Zalduondo, F. and Engelman, D.M., 1981. Conformation of liquid N-alkanes. Biophysical journal, 35(3), pp.587-594.

92. Fixman, M., 1962. Radius of gyration of polymer chains. The Journal of Chemical Physics, 36(2), pp.306-310.

93. Streeter D J, Boyer R F., 1951, Solution Viscosity and Partial Specific Volume of Polystyrene. Effect of Solvent Type and Concentration[J]. Industrial & Engineering Chemistry, 43(8) , pp. 1790-1797.

94. Ahmadi G., 2005, London–Van der Waals force[J]. Fluid Mechanics of Aerosols. Clarkson University, 24.

95. Streeter, D.J. and Boyer, R.F., 1951. Solution Viscosity and Partial Specific Volume of Polystyrene. Effect of Solvent Type and Concentration. Industrial & Engineering Chemistry, 43(8), pp.1790-1797.

96. Petrishcheva, E. and Abart, R., 2009. Exsolution by spinodal decomposition I: Evolution equation for binary mineral solutions with anisotropic interfacial energy. American Journal of Science, 309(6), pp. 431–449.

97. Huang, L., Sui, W., Wang, Y. and Jiao, Q., 2010. Preparation of chitosan/chondroitin sulfate complex microcapsules and application in controlled release of 5-fluorouracil. Carbohydrate Polymers, 80(1), pp.168-173.

98. Yang, H., Liu, Y., Shen, Q., Chen, L., You, W., Wang, X. and Sheng, J., 2012. Mesoporous silica microcapsule-supported Ag nanoparticles fabricated via nano-assembly and its antibacterial properties. Journal of Materials Chemistry, 22(45), pp.24132-24138.

99. Yang,ct sizes for direct synthesis of isoparaffins. Applied Catalysis A: General, 329, pp.99-105.

100. Zhang, K., Wu, W., Guo, K., Chen, J.F. and Zhang, P.Y., 2009. Magnetic polymer enhanced hybrid capsules prepared from a novel Pickering emulsion polymerization and their application in controlled drug release. Colloids and Surfaces A: Physicochemical and Engineering Aspects, 349(1-3), pp.110-116.

101. Phienluphon, R., Pinkaew, K., Yang, G., Li, J., Wei, Q., Yoneyama, Y., Vitidsant, T. and Tsubaki, N., 2015. Designing core (Cu/ZnO/Al2O3)–shell (SAPO-11) zeolite capsule catalyst with a facile physical way for dimethyl ether direct synthesis from syngas. Chemical Engineering Journal, 270, pp.605-611.

102. Raj, C.R., Suresh, S., Bhavsar, R.R., Singh, V.K. and Reddy, S., 2019. Effect of nano-gallium capsules on thermal energy storage characteristics of manganese organometallic SS-PCM. Thermochimica Acta, 680, p.178341.

103. Aizenberg, J., Weaver, J.C., Thanawala, M.S., Sundar, V.C., Morse, D.E. and Fratzl, P., 2005. Skeleton of Euplectella sp.: structural hierarchy from the nanoscale to the macroscale. Science, 309(5732), pp.275-278.

104. Su, B.L., Sanchez, C. and Yang, X.Y. eds., 2012. Hierarchically structured porous materials: from nanoscience to catalysis, separation, optics, energy, and life science. John Wiley & Sons.

105. Sun, M.H., Huang, S.Z., Chen, L.H., Li, Y., Yang, X.Y., Yuan, Z.Y. and Su, B.L., 2016. Applications of hierarchically structured porous materials from energy storage and conversion, catalysis, photocatalysis, adsorption, separation, and sensing to biomedicine. Chemical society reviews, 45(12), pp.3479-3563.

106. Yang, X.Y., Léonard, A., Lemaire, A., Tian, G. and Su, B.L., 2011. Self-formation phenomenon to hierarchically structured porous materials: design, synthesis, formation mechanism and applications. Chemical Communications, 47(10), pp.2763-2786.

107. Yang, X.Y., Chen, L.H., Li, Y., Rooke, J.C., Sanchez, C. and Su, B.L., 2017. Hierarchically porous materials: synthesis strategies and structure design. Chemical Society Reviews, 46(2), pp.481-558.

108. Su, B.L., Sanchez, C. and Yang, X.Y., 2012. Insights into hierarchically structured porous materials: from nanoscience to catalysis, separation, optics, energy, and life science. Hierarchically Structured Porous Materials, pp.1-27.

109. Yang, X.Y., Tian, G., Chen, L.H., Li, Y., Rooke, J.C., Wei, Y.X., Liu, Z.M., Deng, Z., Van Tendeloo, G. and Su, B.L., 2011. Well‐Organized Zeolite Nanocrystal Aggregates with Interconnected Hierarchically Micro–Meso–Macropore Systems Showing Enhanced Catalytic Performance. Chemistry–A European Journal, 17(52), pp.14987-14995.

110. Lu, Y., Cheng, X., Tian, G., Zhao, H., He, L., Hu, J., Wu, S.M., Dong, Y., Chang, G.G., Lenaerts, S. and Siffert, S., 2018. Hierarchical CdS/m-TiO2/G ternary photocatalyst for highly active visible light-induced hydrogen production from water splitting with high stability. Nano Energy, 47, pp.8-17.

111. Sanchez, C., Arribart, H. and Guille, M.M.G., 2005. Biomimetism and bioinspiration as tools for the design of innovative materials and systems. Nature materials, 4(4), pp.277-288.

112. Naik, R.R. and Singamaneni, S., 2017. Introduction: Bioinspired and biomimetic materials. Chemical reviews, 117(20), pp.12581-12583.

113. Liu, K. and Jiang, L., 2011. Bio-inspired design of multiscale structures for function integration. Nano Today, 6(2), pp.155-175.

114. West, G.B., Brown, J.H. and Enquist, B.J., 1999. The fourth dimension of life: fractal geometry and allometric scaling of organisms. science, 284(5420), pp.1677-1679.

115. Bettencourt, L.M., 2013. The origins of scaling in cities. science, 340(6139), pp.1438-1441.

116. West, G.B., Brown, J.H. and Enquist, B.J., 1997. A general model for the origin of allometric scaling laws in biology. Science, 276(5309), pp.122-126.

117. Sherman, T.F., 1981. On connecting large vessels to small. The meaning of Murray's law. The Journal of general physiology, 78(4), pp.431-453.

118. Murray, C.D., 1926. The physiological principle of minimum work: I. The vascular system and the cost of blood volume. Proceedings of the National Academy of Sciences of the United States of America, 12(3), p.207.

119. Murray, C.D., 1926. The physiological principle of minimum work applied to the angle of branching of arteries. The Journal of general physiology, 9(6), pp.835-841.

120. Murray, C.D., 1926. The physiological principle of minimum work: II. Oxygen exchange in capillaries. Proceedings of the National Academy of Sciences of the United States of America, 12(5), p.299.

121. Shan, X.D., Wang, M. and Guo, Z.Y., 2011. Geometry optimization of self-similar transport network. Mathematical Problems in Engineering, 2011.

122. Bejan, A. and Lorente, S., 2013. Constructal law of design and evolution: Physics, biology, technology, and society. Journal of Applied Physics, 113(15), p.6.

123. Bejan, A. and Lorente, S., 2010. The constructal law of design and evolution in nature. Philosophical Transactions of the Royal Society B: Biological Sciences, 365(1545), pp.1335-1347.

124. Zheng, X., Shen, G., Li, Y., Duan, H., Yang, X., Huang, S., Wang, H., Wang, C., Deng, Z. and Su, B.L., 2013. Self-templated synthesis of microporous CoO nanoparticles with highly enhanced performance for both photocatalysis and lithium-ion batteries. Journal of Materials Chemistry A, 1(4), pp.1394-1400.

125. Zheng, X., Wang, H., Wang, C., Deng, Z., Chen, L., Li, Y., Hasan, T. and Su, B.L., 2016. 3D interconnected macro-mesoporous electrode with self-assembled NiO nanodots for high-performance supercapacitor-like Li-ion battery. Nano Energy, 22, pp.269-277.

126. Rabani, E., Reichman, D.R., Geissler, P.L. and Brus, L.E., 2003. Drying-mediated self-assembly of nanoparticles. Nature, 426(6964), pp.271-274.

127. Stannard, A., Martin, C.P., Pauliac-Vaujour, E., Moriarty, P. and Thiele, U., 2008. Dual-scale pattern formation in nanoparticle assemblies. The Journal of Physical Chemistry C, 112(39), pp.15195-15203.

128. Min, Y., Akbulut, M., Kristiansen, K., Golan, Y. and Israelachvili, J., 2010. The role of interparticle and external forces in nanoparticle assembly. Nanoscience And Technology: A collection of reviews from Nature journals, pp.38-49.

129. Xu, X., Zhuang, J. and Wang, X., 2008. SnO2 quantum dots and quantum wires: controllable synthesis, self-assembled 2D architectures, and gas-sensing properties. Journal of the American Chemical Society, 130(37), pp.12527-12535.

130. Wang, X., Liu, W., Liu, J., Wang, F., Kong, J., Qiu, S., He, C. and Luan, L., 2012. Synthesis of nestlike ZnO hierarchically porous structures and analysis of their gas sensing properties. ACS applied materials & interfaces, 4(2), pp.817-825.

131. Lee, J.H., 2009. Gas sensors using hierarchical and hollow oxide nanostructures: overview. Sensors and Actuators B: Chemical, 140(1), pp.319-336.

132. Duan, H., Zheng, X., Yuan, S., Li, Y., Tian, Z., Deng, Z. and Su, B., 2012. Sub-3 nm NiO nanoparticles: Controlled synthesis, and photocatalytic activity. Materials Letters, 81, pp.245-247.

133. Zhang, Y., Kang, Z., Yan, X. and Liao, Q., 2015. ZnO nanostructures in enzyme biosensors. Science China Materials, 58(1), pp.60-76.

134. Vargas, D.P., Giraldo, L. and Moreno-Piraján, J.C., 2016. Characterisation of granular activated carbon prepared by activation with CaCl 2 by means of gas adsorption and immersion calorimetry. Adsorption, 22(4-6), pp.717-723.

135. Du, J., Lai, X., Yang, N., Zhai, J., Kisailus, D., Su, F., Wang, D. and Jiang, L., 2011. Hierarchically ordered macro− mesoporous TiO2− graphene composite films: improved mass transfer, reduced charge recombination, and their enhanced photocatalytic activities. ACS nano, 5(1), pp.590-596.

136. Yao, K.X., Yin, X.M., Wang, T.H. and Zeng, H.C., 2010. Synthesis, self-assembly, disassembly, and reassembly of two types of Cu2O nanocrystals unifaceted with {001} or {110} planes. Journal of the American Chemical Society, 132(17), pp.6131-6144.

137. Ha, D.H., Islam, M.A. and Robinson, R.D., 2012. Binder-free and carbon-free nanoparticle batteries: a method for nanoparticle electrodes without polymeric binders or carbon black. Nano letters, 12(10), pp.5122-5130.

138. Patil, B., Ahn, S., Yu, S., Song, H., Jeong, Y., Kim, J.H. and Ahn, H., 2018. Electrochemical performance of a coaxial fiber-shaped asymmetric supercapacitor based on nanostructured MnO2/CNT-web paper and Fe2O3/carbon fiber electrodes. Carbon, 134, pp.366-375.

139. Yoon, S.B., Choi, B.S., Lee, K.W., Moon, J.K., Choi, Y.S., Kim, J.Y., Cho, H., Kim, J.H., Kim, M.S. and Yu, J.S., 2014. New mesoporous silica/carbon composites by in situ transformation of silica template in carbon/silica nanocomposite. Journal of Experimental Nanoscience, 9(3), pp.221-229.

140. Nie, Z., Petukhova, A. and Kumacheva, E., 2010. Properties and emerging applications of self-assembled structures made from inorganic nanoparticles. Nature nanotechnology, 5(1), pp.15-25.

141. Fan, H., Hartshorn, C., Buchheit, T., Tallant, D., Assink, R., Simpson, R., Kissel, D.J., Lacks, D.J., Torquato, S. and Brinker, C.J., 2007. Modulus–density scaling behaviour and framework architecture of nanoporous self-assembled silicas. Nature materials, 6(6), pp.418-423.

142. Tekin, E., Smith, P.J. and Schubert, U.S., 2008. Inkjet printing as a deposition and patterning tool for polymers and inorganic particles. Soft Matter, 4(4), pp.703-713.

143. Calvert, P., 2001. Inkjet printing for materials and devices. Chemistry of materials, 13(10), pp.3299-3305.

144. Minemawari, H., Yamada, T., Matsui, H., Tsutsumi, J.Y., Haas, S., Chiba, R., Kumai, R. and Hasegawa, T., 2011. Inkjet printing of single-crystal films. Nature, 475(7356), pp.364-367.

145. De Gans, B.J., Duineveld, P.C. and Schubert, U.S., 2004. Inkjet printing of polymers: state of the art and future developments. Advanced materials, 16(3), pp.203-213.

146. Boland, T., Xu, T., Damon, B. and Cui, X., 2006. Application of inkjet printing to tissue engineering. Biotechnology Journal: Healthcare Nutrition Technology, 1(9), pp.910-917.

147. Roth, E.A., Xu, T., Das, M., Gregory, C., Hickman, J.J. and Boland, T., 2004. Inkjet printing for high-throughput cell patterning. Biomaterials, 25(17), pp.3707-3715.

148. Sirringhaus, H. and Shimoda, T., 2003. Inkjet printing of functional materials. MRS bulletin, 28(11), pp.802-806.

149. Li, J., Ye, F., Vaziri, S., Muhammed, M., Lemme, M.C. and Östling, M., 2013. Efficient inkjet printing of graphene. Advanced materials, 25(29), pp.3985-3992.

150. Sirringhaus, H., Kawase, T., Friend, R.H., Shimoda, T., Inbasekaran, M., Wu, W. and Woo, E.P., 2000. High-resolution inkjet printing of all-polymer transistor circuits. Science, 290(5499), pp.2123-2126.

151. Cummins, G. and Desmulliez, M.P., 2012. Inkjet printing of conductive materials: a review. Circuit world.

152. Lee, H.H., Chou, K.S. and Huang, K.C., 2005. Inkjet printing of nanosized silver colloids. Nanotechnology, 16(10), p.2436.

153. Wang, Y., Deng, R., Yang, L. and Bain, C.D., 2019. Fabrication of monolayers of uniform polymeric particles by inkjet printing of monodisperse emulsions produced by microfluidics. Lab on a Chip, 19(18), pp.3077-3085.

154. Ciamarra M P, Coniglio A, de Candia A., 2010. Disordered jammed packings of frictionless spheres[J]. Soft Matter, 6(13) , pp. 2975-2981.

155. Vehring R., 2008, Pharmaceutical particle engineering via spray drying[J]. Pharmaceutical research, 25(5), pp. 999-1022.

156. Lopes, M.C., Bonaccurso, E., Gambaryan-Roisman, T. and Stephan, P., 2013. Influence of the substrate thermal properties on sessile droplet evaporation: Effect of transient heat transport. Colloids and Surfaces A: Physicochemical and Engineering Aspects, 432, pp.64-70.

157. Chen, X., Wang, X., Chen, P.G. and Liu, Q., 2017. Thermal effects of substrate on Marangoni flow in droplet evaporation: response surface and sensitivity analysis. International Journal of Heat and Mass Transfer, 113, pp.354-365.

158. Lim, T., Han, S., Chung, J., Chung, J.T., Ko, S. and Grigoropoulos, C.P., 2009. Experimental study on spreading and evaporation of inkjet printed pico-liter droplet on a heated substrate. International Journal of Heat and Mass Transfer, 52(1-2), pp.431-441.

159. Gelderblom, H., Marin, A.G., Nair, H., Van Houselt, A., Lefferts, L., Snoeijer, J.H. and Lohse, D., 2011. How water droplets evaporate on a superhydrophobic substrate. Physical Review E, 83(2), p.026306.

160. Stauber, J.M., Wilson, S.K., Duffy, B.R. and Sefiane, K., 2015. Evaporation of droplets on strongly hydrophobic substrates. Langmuir, 31(12), pp.3653-3660.

161. Dugas, V., Broutin, J. and Souteyrand, E., 2005. Droplet evaporation study applied to DNA chip manufacturing. Langmuir, 21(20), pp.9130-9136.

162. Stephenson R, Stuart J, Tabak M., 1984, Mutual solubility of water and aliphatic alcohols[J]. Journal of chemical and engineering data, 29(3) , pp. 287-290.

8. Appendix

8.1 in situ fabrication of polymeric microcapsules by inkjet printing of emulsions

Renhua Deng*, Yilin Wang, Lisong Yang and Colin D. Bain*

Department of Chemistry, Durham University, Stockton Road, Durham DH1 3LE, U.K.

KEYWORDS: ink-jet printing, microcapsules, polymer, emulsion, tebuconazole, phase separation

Abstract: Phase separation driven by solvent evaporation of emulsions can be used to create polymeric microcapsules. The combination of emulsion solvent evaporation with ink-jet printing allows the rapid fabrication of polymeric microcapsules at a target location on a surface. The ink is an oil-in-water emulsion containing in the dispersed phase a shell-forming polymer, a core-forming fluid that is a poor solvent for the polymer, and a low-boiling good solvent. After the emulsion is printed onto the substrate, the good solvent evaporates by diffusion through the aqueous phase, and the polymer and the poor solvent phase separate to form microcapsules. The continuous aqueous phase contains polyvinyl alcohol that serves as an emulsifier and a binder of the capsules to the substrate. This method is demonstrated for microcapsules with various shell-forming polymers (polystyrene, poly(methylmethacrylate) and poly(L-lactide)) and core-forming poor solvents (hexadecane and a 4-heptanone/sunflower oil mixture). Cargoes such as fluorescent dyes (Nile Red and tetracyanoquinodimethane) or active ingredients (e.g., the fungicide tebuconazole) can be encapsulated. Uniform microcapsules are obtained by printing emulsions containing monodisperse oil droplets produced in a microfluidic device. We discuss the physical parameters that need to be controlled for the successful fabrication of microcapsules in inkjet printing. The method for rapid, in situ encapsulation could be useful for controlled-release applications such as in agrochemical sprays, fragrances, functional coatings, and topical medicines.

Introduction

Polymeric microcapsules as containers/carriers can be used for self-healing coating [1-3], sensors [4,5], phase change materials [6], controlled release of drugs and pesticides [7-13], pressure-sensitive switches [14], displays or smart windows [15,16], optical materials [17], enzyme immobilization [18], and fragrances [19]. Microcapsules can protect active cargoes against environmental hazards (such as moisture, oxidation and bacteria), and thus increase

their shelf life. [20] Microcapsules allow the release of drugs in a controlled way [21-28], which can enhance their efficacy and decreases costs and side effects. Moreover, encapsulation allowing the safe handling of toxic chemicals (such as pesticides) and permits liquid droplets to be handled as solids or to be embedded in a solid matrix [5,16].

Various approaches for fabricating polymer microcapsules have been demonstrated [29,30], including coacervation of polymers or polymerization at the interface of emulsion droplets [31], absorption of polymers or polymerization on the surface of solid templates (particles) [8], evaporation of double emulsions [11,21], and inner phase separation in emulsion droplets. [32-34] Each method has limitations and different approaches are optimized for different applications. Interfacial coacervation or polymerization only works for a very limited range of polymers with specific solubility. Moreover, the microcapsules obtained by interfacial coacervation have thin shell, which are rather brittle. Interfacial polymerization gives more robust shells, but the reaction conditions, such as heating, may decompose the active material in the capsule, and the unreacted monomer may remain in the core as an impurity. The solid template-based methods involve removal of the templates, which represents an extra processing step and requires the separate production of the templates. Encapsulation is then achieved by swelling of the polymer shell and diffusion of cargoes into the pre-formed microcapsules, which can have low efficiency. The double-emulsion method needs a two-step emulsification process, and each double-emulsion droplet can encompass different numbers of small droplets with different size, resulting in ill-defined morphology and heterogeneous shell thickness. Uniform double emulsions can be achieved by microfluidics [11,19,21], however, the size of capsules has to date been limited to tens of microns. Many of these problems can be overcome by the phase separation method in which microcapsules are formed by evaporation of the solvent in the discrete phase of an emulsion, under ambient conditions [7,13,33,35]. In the approach we adopt here, an oil-in-water (o/w) single emulsion contains a mixture of a polymer and a non-volatile poor solvent dissolved in a volatile good solvent as the dispersed phase. Vincent and coworkers have shown that, as the good solvent evaporates, the polymer forms small polymer-rich droplets in which the polymer phase-separates from the poor solvent (which is less volatile than the good solvent).[26] If the spreading coefficient and Hamaker constant have the correct sign, these polymer droplets migrate to the oil–water interface where they form a wetting film. Further evaporation of the good solvent encourages more polymer to precipitate to form a shell at the interface. High encapsulation efficiency is achieved by pre-dissolving the cargo in the volatile solvent and choosing a co-solvent that is a good

solvent for the cargo but a poor solvent for the polymer. The size and shell thickness of the microcapsules is controlled by variation of the initial size of droplets and the polymer concentration.

Loss of cargo is unavoidable during storage and transport of pre-produced microcapsules, especially in the cases where the loading or release mechanism is via swelling of the polymer shell. In-situ formation of microcapsules at a targeted location avoids loss of cargo during transportation and storage. In principle, the evaporation-driven phase separation method permits the direct formation of microcapsules on surfaces, which is of interest for applications such as pesticides, fragrances, topical medicine, and functional patterns. Therefore, developing methods for combining evaporation-driven phase separation with printing, spraying or coating technology may provide new ways for encapsulation, delivery and release.

Here we demonstrate that in-situ rapid encapsulation on targeted sites is achievable by combining ink-jet printing with evaporation-driven phase separation. Ink-jet printing possesses attractive features as a manufacturing technology including efficient use of materials, scaleability, patterning and localised delivery to specific locations on a surface. We have recently introduced the method of combining ink-jet printing with emulsion-solvent evaporation to generate polymeric micro-spheres on a surface. [36] The challenge in producing microcapsules (rather than solid particles) lies in the short timescales of evaporation of droplets in water (the continuous phase) in the inkjet regime (~2 s). We show that phase-separation-induced microcapsule formation can indeed be achieved in inkjet printing and that a cargo initially dissolved in the oil phase does reside within the printed capsules.

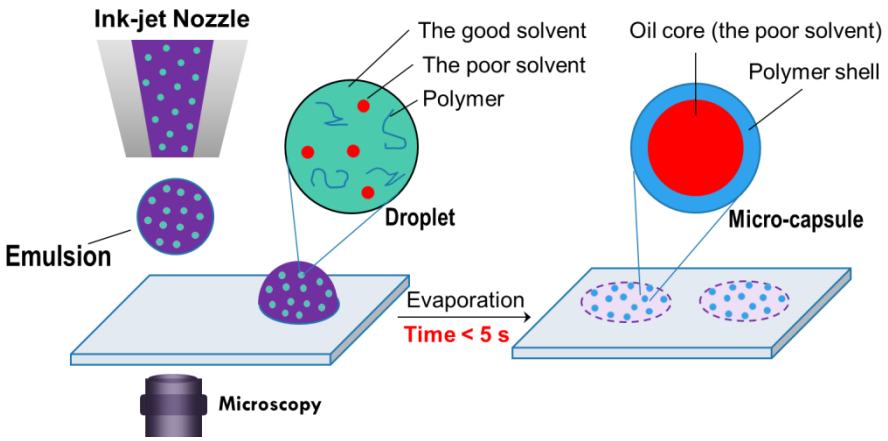

Scheme 1. Schematic diagram of the fabrication of polymer micro-capsules by ink-jet printing.

EXPERIMENTAL SECTION

Materials. Polystyrene (PS, M.W. ca. 35 kg mol^{-1}), poly(L-lactide) 2-hydroxyethyl methacrylate terminated (PLLA, M_n = 5.5 kg mol^{-1}, PDI $\leq$ 1.2), sodium dodecyl sulfate (SDS, > 99%), and hexamethyldisilazane (HMDS, 98%) were purchased from Sigma-Aldrich; poly(methylmethacrylate) (PMMA, M.W. ca. 35 kg mol^{-1}), poly(vinyl alcohol) (PVA, M.W. ca. 31–50 kg mol^{-1}, 87–89% hydrolysed), Nile Red (99%) and 7,7,8,8–tetracyanoquinodimethane (TCNQ, 98%) from Acros Organics; 4-heptanone (89%) from Alfa Aesar; dichloromethane (DCM, >99%) and ethyl acetate (EtOAc, >99.99%) from Fisher Scientific; hexadecane (>98%) from TCI; tebuconazole from LKT Laboratories. All chemicals were used as received.

Preparation of emulsion. DCM solution containing polymer (e.g., 10 mg mL^{-1} PS) and poor solvent (e.g. 1.0 v/v % hexadecane) was used as the oil phase. 0.3 wt.% PVA solution was used as the aqueous phase. The mixture of the oil phase (1.0 mL) and water phase (2.0 mL) in a 10-mL vial was then emulsified by high-speed shearing (25.9k rpm) for 30 s using a homogenizer (T10 Ultra Turrax, IKA). The emulsion obtained was sealed and kept at room temperature.

Microfluidics. Microfluidics. Oil and water solutions were filtered through 0.2 μm poly-(tetrafluoroethylene) filters and loaded into gas-tight borosilicate syringes. The solutions

were injected by using syringe pumps into a microfluidic chip (DolomiteDolomite) with a flow-focusing junction (5 µm etch depth and 8 µm junction width). The oil phase was injected into the central channel of the microfluidic chip and the water phase, into the two side channels of the microfluidic chip. The flow rate of the aqueous phase was 2 µL min−1, and the flow rate of the oil phase was 0.2 µL/min. The emulsion droplet diameter was 7 µm. The emulsion thus formed was transferred via FEP tubing to the inkjet printhead. For full experimental details, see ref [42].

Modification of substrates. Glass cover slips (22×22 mm) were first washed with ethanol, then placed in a bath sonicator in a 2 wt.% alkaline detergent solution (Decon90; Decon Laboratories) for 30 mins, rinsed with deionized water and dried under a nitrogen flow. The cover slips were then exposed to an air plasma for 15 mins, rinsed with deionized water, dried under a nitrogen flow and placed in an oven at 70 °C for 2 h. HMDS was deposited on the surface by vapor deposition in a vacuum desiccator for 2 h. The coated cover slips were rinsed with acetone and water, and dried under a nitrogen flow.

Ink-jet printing. The ink (emulsion) was shaken well before printing. Picolitre drops of the emulsion were ejected from a Microfab drop-on-demand device (MJ-ABP-01, Microfab Technologies; 50-µm diameter orifice) controlled by a Microfab driver unit (Microfab JetDrive III Controller CT-M3-02) onto the modified substrate. The waveform used for printing was adjusted between ± 30-40 V. The printed drops were allowed to dry freely under ambient conditions at a temperature of 20-22 °C and relative humidity of 24-50%. The evaporation process on the substrate was recorded with a high-speed camera (Photron APX RS).

Characterization. SEM images were recorded using a Hitachi SU70 SEM operated at an acceleration voltage of 5-10 kV. A conductive film of gold was coated onto the samples by sputtering before SEM imaging. The contact angles and interfacial tensions (by pendent drop method) were measured by a tensiometer (FTÅ200, First Ten Ångstroms) with built-in software (Fta32 v2.0). Rheological data were collected at 293 K using an AR 2000 rheometer (TA Instruments) with a cone (2° angle) and plate geometry for PVA and SDS aqueous solutions. The steady-state viscosity of each fluid was recorded over shear rates from 0.1 to 1000 s^{-1}. The viscosity data at shear rate 100 s^{-1} is selected because this shear rate is characteristic of the internal flows in drying droplets. Raman spectra and Raman images were recorded using a 532 nm laser (Opus 532, Laser Quantum, Manchester). Samples for Raman analysis were printed onto clean silicon substrates, and the Raman instrument was

calibrated using the silicon band at 520.7 cm^{-1}. Reference spectra of polymers, tebuconazole and PVA were collected from 600 to 4000 cm^{-1}. Raman images were acquired for 30 s per image through a tuneable band-pass filter, with a 30-s acquisition time and a central Stokes shift of 2900 cm^{-1}. Data at five different filter angles were collected and used to reconstruct maps of component distribution using in-house MATLAB software. Fluorescence microscopy images was recorded using a Leica SB5 II Confocal Microscopy with PhMoNa super resolution module [38] using 442 nm and 532 nm excitation for TCNQ and Nile Red, respectively.

Results and Discussion

The strategy for forming microcapsules requires an oil phase predominantly formed of a good solvent for the polymer with a small amount of a solvent that is miscible with the good solvent but that is a poor solvent for the polymer. The solubility of a polymer in a solvent can be predicted from the Flory−Huggins interaction parameters of solvent−polymer pairs (χ_{S-P}), [39]

$$\chi_{S-P} = \frac{V_S(\delta_S-\delta_P)^2}{RT} + 0.34 \quad [1]$$

where V_S is the molar volume of the solvent, δ_S and δ_P the solubility parameters of solvent and polymer, respectively (Table 5.1), R the ideal gas constant, and T the temperature. Complete solvent−polymer miscibility is expected when $\chi_{S-P} < 0.5$, so we chose DCM as the good solvent with hexadecane as the poor solvent. The good solvent, DCM, was chosen to be much more volatile than water in order to generate polymeric particles [36] rather than a continuous film [40] after evaporation. The poor solvent was chosen to be much less volatile than water so that it remained in the core of the microcapsules after the continuous phase of the droplet had dried.

Table 5.1. Properties of polymers and solvents.

Polymers/ Solvents	δ^a ($MPa^{1/2}$)	*S-P*	χ_{S-P}
PS	18.6	DCM-PS	0.38
PMMA	19.4	Hexadecane-PS	0.92
PLLA	21.7[b]	DCM-PMMA	0.34
DCM	19.8	Hexadecane-PMMA	1.43
EtOAc	18.6	DCM-PLLA	0.43
Hexadecane	16.4	Hexadecane-PLLA	3.73

[a] data from reference [39]; [b] data from reference [41]

Figure 1 shows the particles or capsules formed from an o/w emulsion as the ink, in which the oil droplets contained 10 mg mL^{-1} PS as the shell-forming polymer and varying amounts of the core-forming poor solvent (hexadecane). The continuous phase was an aqueous solution of the emulsifier PVA. The ink was jetted through a print nozzle with a 50-μm diameter orifice onto a transparent glass substrate modified by HMDS (water contact angle, θ_{H_2O} = 60 ± 3°) and allowed to evaporate under ambient conditions. The morphology of the particles formed in-situ was observed by SEM on the dry deposit. As previously reported [36], solid PS micro-spheres are generated in the absence of hexadecane (Figure 8.1a_3). In the presence of 1% v/v hexadecane in DCM, porous particles were observed (Figure 8.1b_3), which can be attributed to the formation of droplets of hexadecane and the subsequent evaporation of hexadecane in the high-vacuum environment during SEM imaging. The particle structure involving multiple small droplets of hexadecane embedded in a PS matrix is known as occluded morphology. [35] The occluded morphology results from incomplete phase separation between shell and core. Dowding et al. [42] constructed a phase diagram for PS(MW ca. 280 kg mol^{-1}) /hexadecane/DCM mixtures; while the polymer chain length is higher than that used here, it provides an approximate model for our experiments. For our initial composition of 0.58 wt% hexadecane, 0.75 wt% PS, 98.7 wt% DCM by weight, the phase boundary is reached at 80 wt% DCM, corresponding to a radius of

droplet that is 40% of its initial size. The phase boundary is at the polymer-rich side of the two phase-region so hexadecane-rich droplets will nucleate in a continuous PS-rich phase. The low viscosity of DCM (μ = 0.43 mPa s) and low molecular weight of the PS (35 kg mol^{-1}) result in a Peclet number, *Pe < 1* ($Pe = \frac{Ea}{D} \sim 0.2$, where the evaporation rate *E* ~ 3 μm s^{-1}, typical droplet radius *a* ~ 6 μm, and diffusion coefficient *D* ~ 10^{-10} m s^{-2}); Pe for hexadecane is an order of magnitude smaller. The Peclet number is a measure of the relative importance of convection and diffusion: a value of *Pe* < 1 implies that the polymer and hexadecane concentrations are approximately uniform throughout the droplets. Consequently, it is physically reasonable that nucleation of hexadecane droplets occurs within the body of the emulsion droplets, which has observed in bigger droplets. [43] Increasing the ratio of hexadecane/PS causes the phase separation to occur earlier during drying and the hexadecane droplets coalesce more easily at higher hexadecane concentration. Indeed, particles with fewer but larger caps or even complete capsules were observed when the content of hexadecane was increased to 1.16 wt.% (Figure 8.1c$_3$).

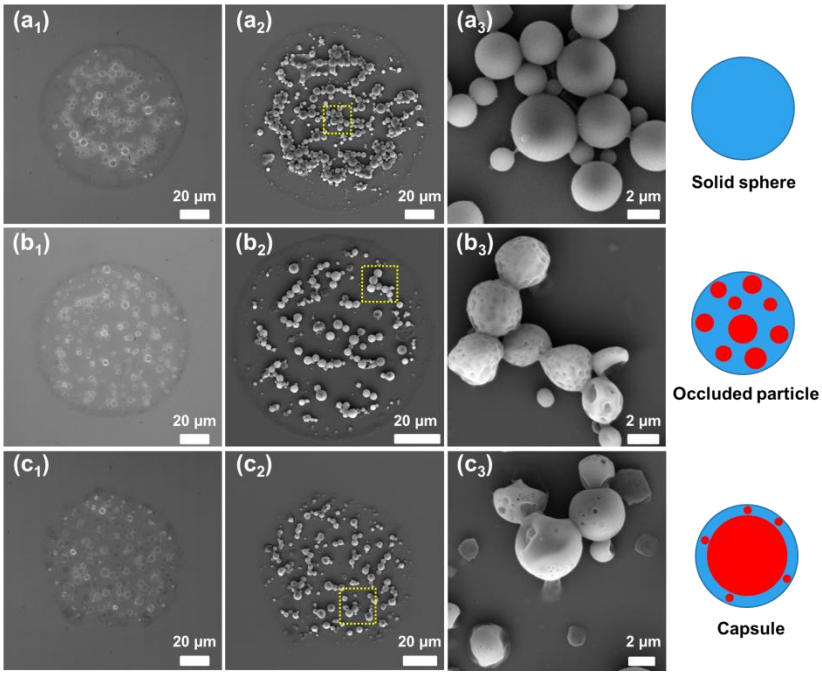

Figure 8.1. Morphology of PS/hexadecane particles. (a_1, b_1, and c_1) Micrographs and (a_2, b_2, and c_2) SEM images of the deposits from printed drops of emulsion containing 0.75 wt% PS and varied hexadecane: (a) without hexadecane, (b) 0.58 wt%, and (c) 1.16 wt%. (a_3, b_3, and c_3) SEM images at high magnification showing the morphologies of the particles and corresponding schematic diagrams on the right side, where blue represents PS and red represents hexadecane.

Complete phase separation of the polymer and poor solvent does not guarantee a core-shell structure: there are three equilibrium morphologies – core-shell, acorn-like and two separated spheres, depending on the interfacial tensions (σ) of the three phases (polymer, the poor solvent, and the aqueous phase). [13] Furthermore, either the poor solvent or the polymer could form the core. To ensure that the core contains the poor solvent, the interfacial tension of the poor solvent with the aqueous phase σ_{ow} (in the presence of emulsifier) should be higher than that between the polymer and the aqueous phase. The interfacial tension σ_{ow} depends on the emulsifier. The hexadecane/PS system can form core-shell structures with PVA (σ_{ow} = 16.4 mN m^{-1}) as the surfactant; however, a small molecular surfactant, such as SDS, yields coexisting acorns and even two separated spheres (Figure 8.S1). SDS at a concentration of 3 mg mL^{-1} reduces the interfacial tension too much (σ_{ow} = 6.7 mN m^{-1}), which drives hexadecane to the surface of droplets. Another advantage

of using PVA is that the particles were generally observed to be randomly distributed in the deposit without either a ring stain or a central aggregate. We surmise that the PVA acts to bind the capsules to the substrate. In comparison, the particles deposited from an SDS-stabilized emulsion were concentrated in the centre of the deposit (Figure 8.S1) due to inward capillary forces in the latter stages of drying. [36]

The Hamaker constant, A_H, determines the long-range interactions between the water and oil phases separated by the polymer shell. The free energy, *F(d)* per unit area of the water/core/shell structure is given by

$$F(d) = \sigma_{pw} + \sigma_{po} - A_H/12\pi d^2 \qquad [2]$$

where *d* is the thickness of the shell and σ_{pw} and σ_{po} are the polymer–water and polymer–oil interfacial tensions. If $A_H > 0$, it is favourable for the polymer shell to thin in one location and to thicken in another, giving an acorn structure with a low but finite contact angle: this situation is known as pseudo-partial wetting. [44] If $A_H < 0$, then a shell of uniform *d* is favoured. For non-polar oils, the dominant contribution to A_H arises from high-frequency fluctuations in the electron distribution and is related to the refractive index of material. Broadly, A_H will be positive if the shell has a refractive index greater than the core and negative if the refractive index is less than the core. Since PS has a refractive index higher than both DCM and hexadecane, it is likely that $A_H > 0$ and that a core-shell structure of uniform thickness is not thermodynamically stable. This argument may explain why some open structures are observed.

The method for in-situ production of microcapsules can be extended to other polymers and oils that have appropriate interaction parameters (Table 1) and interfacial properties (Table 2). Water-insoluble polymers with higher values of δ are predicted to form core-shell structures, because a higher δ results in poorer compatibility with hexadecane, which favors phase separation, and greater hydrophilicity, which preferentially localises the polymer at the oil/water interface. The experimental contact angles θ and interfacial tensions σ_{ow} between the three phases are shown in Table 2. The contact angle refers to the liquid drop (the poor solvents or the aqueous phase) on the polymer film in air. The polymer films were prepared by evaporation of 20 mg ml^{-1} DCM solutions containing corresponding polymers (PS, PMMA, or PLLA) on the substrate. Both PMMA and PLLA form microcapsules rather than occluded particles (Figure 8.S2), which can be explained by the compatibility of polymer and hexadecane judged by χ_{S-P} (PLLA > PMMA > PS) and σ_{op} (PLLA > PMMA > PS).

Table 2. Contact angles or interfacial tensions of the three phases.

Phase o	Phase w	Phase p	$\boldsymbol{\theta_{op}}$ (°)	$\boldsymbol{\theta_{pw}}$ (°)	$\boldsymbol{\sigma_{ow}}$ (mN m^{-1})
Hexadecane	3 mg ml^{-1} PVA	PS	6.35	69.7	16.4
Hexadecane	3 mg ml^{-1} PVA	PMMA	15.3	70.5	16.4
Hexadecane	3 mg ml^{-1} PVA	PLLA	28.4	60.9	16.4
4-heptanone & sunflower oil	3 mg ml^{-1} PVA	PS	21.8	69.7	11.0
4-heptanone & sunflower oil	3 mg ml^{-1} PVA	PMMA	12.6	70.5	11.0
4-heptanone & sunflower oil	3 mg ml^{-1} PVA	PLLA	24.2	60.9	11.0

DCM can be replaced by other volatile solvents. In laboratory studies, DCM is commonly employed because it is a good solvent for many polymers, is immiscible with water and evaporates readily (which requires both a high vapour pressure and sufficient solubility in water that diffusion through the continuous phase is not rate-limiting). However, exposure to DCM vapor at high levels is hazardous to the health and there are increasing restrictions on the release of DCM into the environment. Safer and more environmentally friendly solvents should share the favourable physical properties of DCM, in terms of solubility for polymers and cargoes, immiscibility with water, and volatility. Ethyl acetate (EtOAc) is a low-toxicity solvent that generally meets these conditions. Microcapsules of both PS and PMMA were obtained with EtOAc instead of DCM (Figure 8.2). The microcapsules prepared with EtOAc (diameter < 2.0 μm) were smaller than those produced with DCM, because the lower interfacial tension between the oil phase and the aqueous phase leads to smaller emulsion droplets (σ_{ow} = 3.2 mN m^{-1} with EtOAc compared to σ_{ow} = 8.0 mN m^{-1} with

DCM). EtOAc is not a good solvent for PLLA, as predicted from the value of $\chi_{EtOAc-PLLA}$ = 0.73.

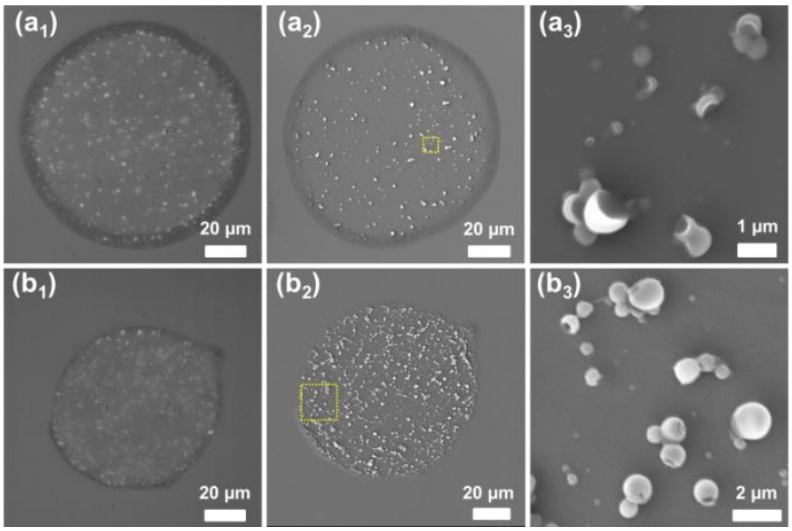

Figure 8.2. (a) PS and (b) PMMA microcapsules prepared with EtOAc as the good solvent. Micrographs (a_1 and b_1) and SEM images (a_2 and b_2) of the deposits from printed emulsion drops; (a_3 and b_3): SEM images at high magnification showing the morphologies of the microcapsules.

Hexadecane has two disadvantages as a core-forming solvent: (i) its high melting point (18 °C) can lead to freezing at low temperatures, reducing release rates and potentially rupturing capsules; (ii) it is a poor solvent for functional cargoes that are polar. An alternative core-forming solvent with higher polarity is 4-heptanone. [42] Heptanone still has appreciable volatility (normal boiling point is 144 °C), so we used a mixture of 4-heptanone with a polar oil (sunflower oil) to prevent collapse of the capsules as the heptanone diffuses through the shell and evaporates. The formation of well-defined PS, PMMA and PLLA microcapsules with 4-heptanone/sunflower oil core was confirmed by SEM (Figure 8.3).

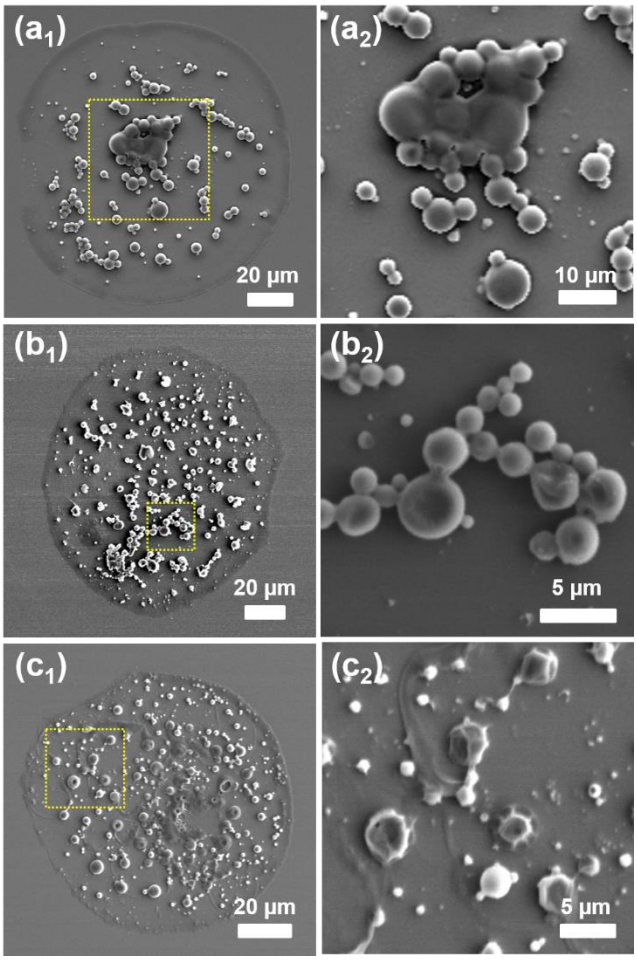

Figure 8.3. (a) PS, (b) PMMA, and (c) PLLA microcapsules prepared with 4-heptanone/sunflower oil mixture as the core-forming oil. (a_1, b_1 and c_1) SEM images of the deposits from printed emulsion drops. (a_2, b_2 and c_2) SEM images at high magnification showing the morphologies of the microcapsules.

To confirm that the oil is retained within the micro-capsules, we dissolved fluorescent dyes in the oil phase of the emulsions and imaged the dry deposits. Figure 8.4 shows examples of microcapsules with shells of PS or PMMA, hexadecane or heptanone/sunflower oil as the poor solvent, and Nile Red or TCNQ as the dye. In each case there is good overlap of the optical micrograph and confocal fluorescence micrograph, showing that dye molecules are confined in the oil core of the micro-capsules. No significant fluorescence was observed from the regions outside of the microcapsules indicating a high degree of encapsulation.

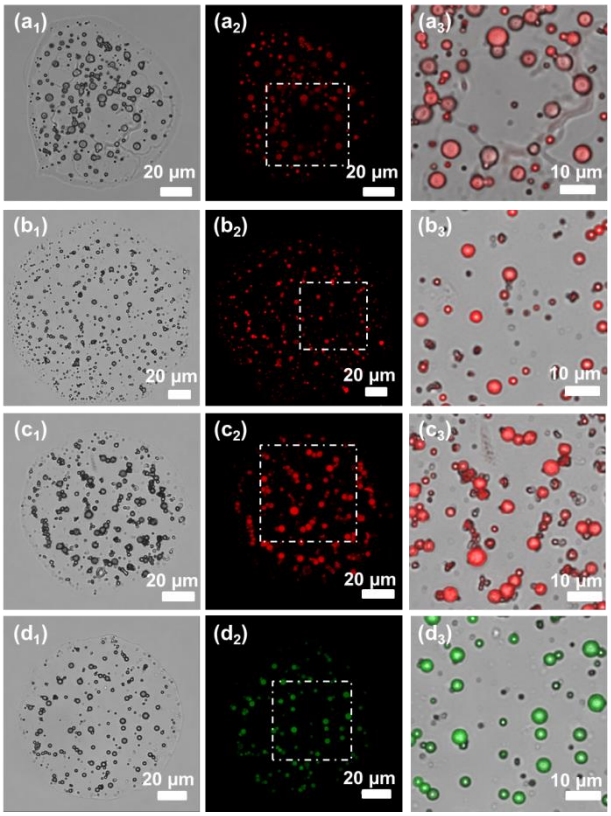

Figure 8.4. Encapsulation of dyes into polymeric micro-capsules: (a) PS shell + heptanone/sunflower oil core with Nile red, (b) PMMA shell + heptanone/sunflower oil core with Nile Red, (c) PMMA shell + hexadecane core with Nile Red, (d) PMMA shell + heptanone/sunflower oil core with TCNQ. Left column: bright-field images; middle column: confocal fluorescence microscopy images; right column overlaid optical and fluorescence images of selected regions.

The time for formation of microcapsules (< 5s) in printed droplets is much shorter than in microcapsules formed by bulk evaporation (tens of minutes or longer). [43] The evaporation of a representative drop is shown in Figure 8.5. Most oil droplets evaporated within 2s to give a particulate dispersion rather than an emulsion. At this point the level of the continuous phase is higher than the particles, which remain fully immersed in the fluid. After 3s, the level of the water dropped below the largest particles whose capsule structure is clearly seen as a bright ring in transmitted light. After 4s, the water has nearly fully evaporated. The evaporation of the solvent of the dispersed phase (DCM) before the continuous phase (water) prevents coalescence of the droplets and yields discrete particles/capsules rather than a continuous film.

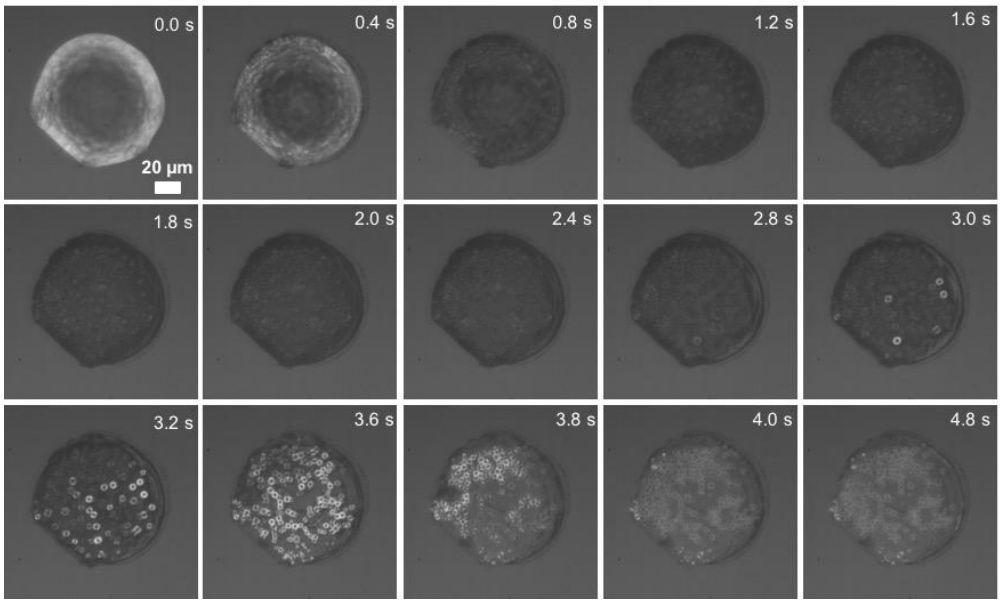

Figure 8.5. Micrographs of the evolution of a printed emulsion drop on the substrate during evaporation.

For practical applications we need to be able to load functional cargoes into polymer particles or microcapsules produced by printing or spraying of emulsions. As a demonstration system, we chose the fungicide tebuconazole, which inhibits the biosynthesis of ergosterols in fungi and which is used for treatment of seeds and spraying of commercial crops. Tebuconazole breaks down slowly in the environment and is toxic to aquatic life. Encapsulation of tebuconazole by polymer could be useful for delayed or triggered release on leaf surfaces and might also reduce animal toxicity because of slow release in vivo.

We initially explored the printing of solid polymer particles containing tebuconazole. The miscibility of polymers and small molecular cargoes can be predicted via the solubility parameter. The solubility parameter of tebuconazole (δ = 20.4 $MPa^{1/2}$) was calculated from group contributions (Equation 3): [45]

$$\delta = \sqrt{{\delta_d}^2 + {\delta_p}^2 + {\delta_h}^2} \qquad [3]$$

where δ_d, δ_p, and δ_h, represent contributions from dispersion forces, dipole–dipole interactions, and hydrogen bonding, respectively. Tebuconazole is predicted to mix well with PMMA or PLLA because the difference in solubility parameters $\Delta\delta$ < 2 $MPa^{1/2}$. Figure 8.6 shows particles of PMMA or PLLA with tebuconazole in a 1:1 mass ratio. No tebuconazole

crystals were observed under crossed polarizers indicating that the active ingredient remained dissolved within the polymer matrix.

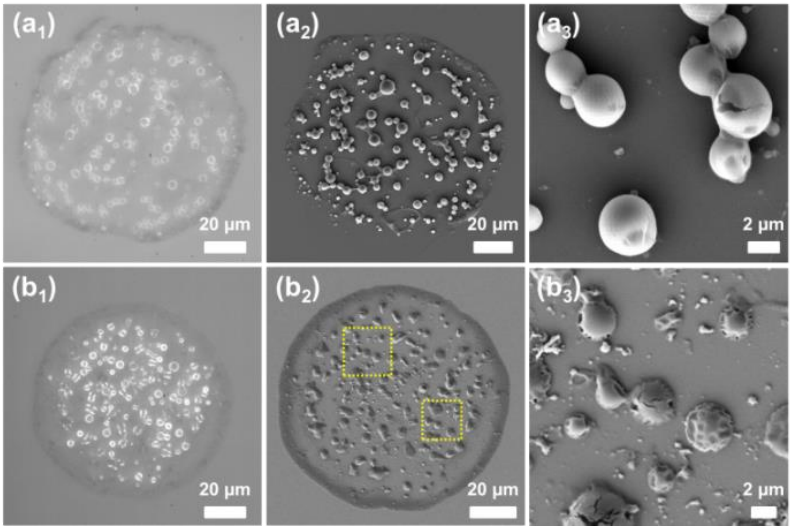

Figure 8.6. Encapsulation of tebuconazole into polymeric particles: (a) PMMA and (b) PLLA. (a_1 and b_1) Micrographs and (a_2 and b_2) SEM images of the deposits from printed drops of emulsion containing 1:1 tebuconazole and polymers. (a_3 and b_3) SEM images at high magnification showing the morphologies of the particles.

Raman imaging confirms that the tebuconazole is distributed within the polymer particles. The spatial resolution of the Raman images is $\sim$1 µm, which is sufficient to determine if phase separation has occurred. Figure 8.7 shows the Raman spectra of PLLA, tebuconazole, and PVA in the C–H stretching region (2800 to 3200 cm^{-1}). Images of the sample were acquired through a tuneable filter for different filter angles which cover the characteristic peaks of the three components in the dry deposits. Five filter angles are sufficient to deconvolute the overlapping features in the different spectral windows and to recover images of the three components, which are shown in Figure 8.8. The maps of PLLA and tebuconazole superimpose showing that tebuconazole is dispersed throughout PLLA matrix without phase separation. A weak signal from the PVA is observed around the particles, identifying the thin film covering the droplet footprint in optical micrographs as PVA. No tebuconazole is observed outside of the polymer particles as expected from its extremely low solubility in water (0.032 mg mL^{-1}) and high solubility in DCM (>200 mg mL^{-1}). A similar result was also obtained when PLLA was replaced by PS (Figure 8.S4) or PMMA (Figure 8.S5).

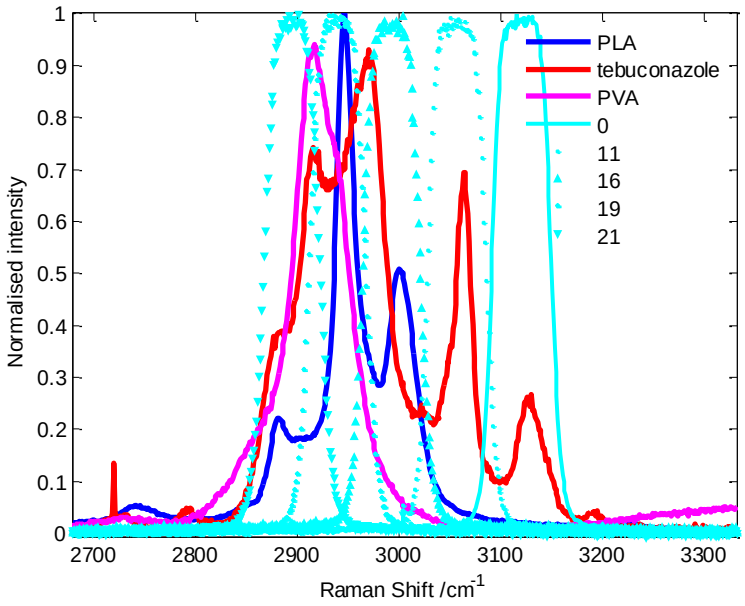

Figure 8.7. Raman spectra of PLLA, tebuconazole, PVA and transmission profiles normalised to the maximum transmission at the filter angles of 0°, 11°, 16°, 19° and 21° used in the fitting procedure.

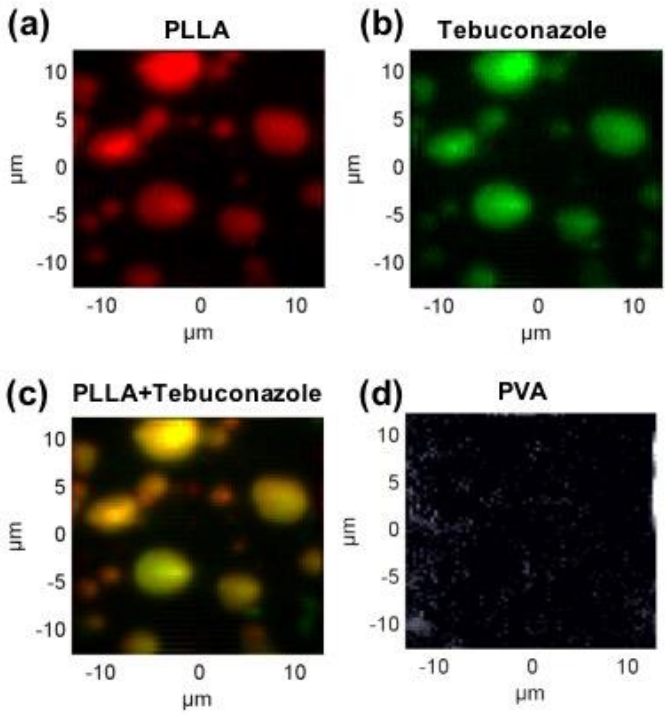

Figure 8.8. Reconstructed Raman images of components of particles containing 1/1 tebuconazole and PLLA from partial region of a printed deposit (a) PLLA, (b) tebuconazole, (c) PLLA + tebuconazole, and (d) PVA.

Cargoes dispersed throughout the polymer matrix of a solid particles have potential for sustained release (e.g. of biocides). For the purpose of controlled release, it is better to load the cargoes into the core of microcapsules, where the shell thickness can be used to vary the release rate and the shell permeability can be tuned to vary with environmental conditions. Additionally, for our agrochemical model system an oleophilic adjuvant is necessary to enhance transport across the cuticle of a leaf: this adjuvant could also be encapsulated in the core of the microcapsule. The core-forming oil should be a good solvent for cargoes so that the cargo remains dissolved in the core when the polymer shell phase-separates. For tebuconazole, we selected the 4-heptanone/sunflower oil mixture as the core-forming oil and the biodegradeable polymer PLLA for the shell. Microcapsules loaded with tebucanozole were obtained by the emulsion-solvent evaporation technique (Figure 8.9a). After 3 weeks, most microcapsules degraded under ambient conditions (Figure 8.9b), releasing puddles of sunflower oil and tebuconazole. In principle, the shell thickness of microcapsules can be controlled by varying the ratio of polymer/poor solvent [42], which in turn affects the degradation time and thus the release rate of cargoes.

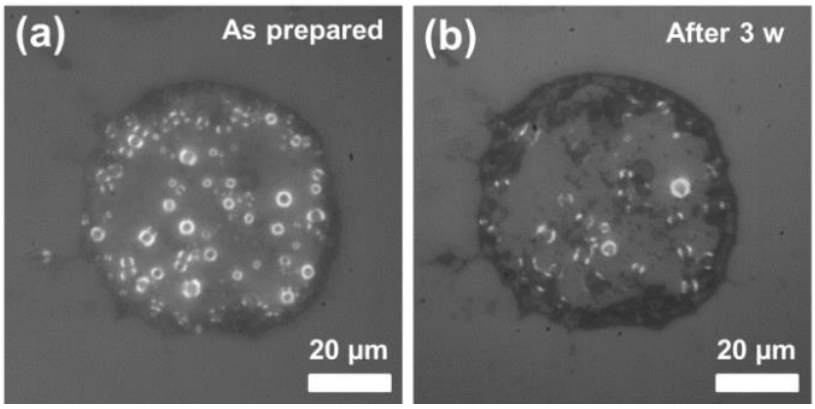

Figure 8.9. Encapsulation of tebuconazole into PLLA microcapsules: Micrographs of a deposit as prepared (a) and after 3 weeks (b).

To develop the experimental conditions for the successful production of microcapsules by inkjet printing, we used homogenized emulsions with a high degree of polydispersity and hence obtained capsules with a large range of sizes. Because the size of microcapsules is an important parameter that affects their properties, it is desirable to control the microcapsule size within a narrower size range. Uniform emulsion droplets can be produced by microfluidics or membrane emulsification. We have chosen the former approach and used a flow-focussing junction to produce monodisperse emulsion droplets with a diameter of 7 µm. The emulsion was then printed through an 80 µm nozzle to reduce

the shear rates that cause fission of emulsion droplets. Video S1 shows the drying of an emulsion droplet and the conversion of oil droplets to capsules. Figure 8.10a shows an SEM image of a dry deposit showing a single layer of capsules with a PMMA shell and a hexadecane core. The size distribution of the capsules (see high-resolution SEM image in Figure 8.10b) is much narrower from the homogenized emulsion, but broader than size distribution of the emulsion drops before printing because of some coalescence/break-up during the printing process.42

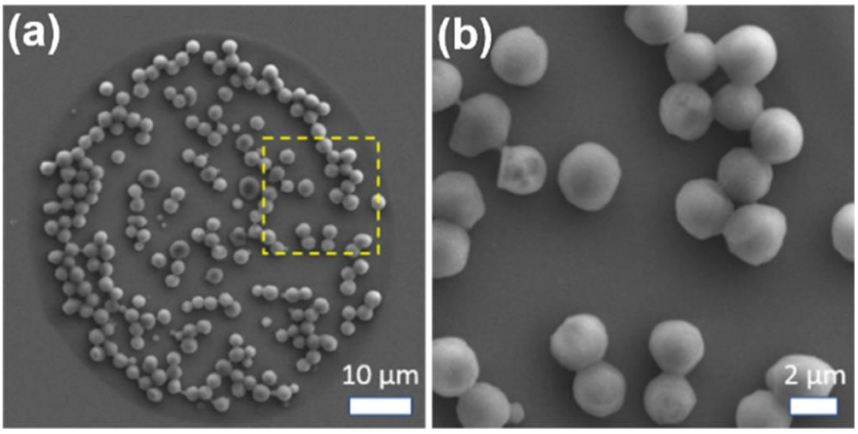

Figure 8.10. (a) SEM image of the deposit formed by inkjet printing of a monodisperse emulsion produced from a continuous phase of 0.3 wt% PVA in water and a discrete phase comprising 1.6 wt % PMMA and 0.9 wt % hexadecane in DCM onto a HDMS-treated glass slide. (b) High-magnification SEM showing the morphologies and size distribution of the microcapsules

Conclusion

We have demonstrated a method for rapid encapsulation of cargoes into polymeric microcapsules via ink-jet printing of emulsions. Evaporation of the good solvent induced phase separation between the polymer and the nonvolatile poor solvent within seconds, resulting in the formation of microcapsules with a polymer shell and a liquid core. The interactions between the good solvent, the poor solvent, the polymer, and the aqueous phase play key roles in the morphology of particles. Fluorescent dyes were used to show that the core-forming oil is retained within the capsules. Raman imaging showed that a model active ingredient (the fungicide tebuconazole) can be encapsulated within solid polymer spheres without phase separation. Microcapsules containing tebuconazole dissolved in 4-heptanone/sunflower oil were also produced. High loadings and encapsulation efficiencies can be achieved for cargoes that possess high miscibility with polymers or the oil core but poor solubility in the aqueous phase. The good solvent of the oil phase, DCM, can be replaced by low toxicity solvents such as ethylacetate for polymers and cargoes with appropriate solubility parameters. This versatile method for in situ and rapid encapsulation may be useful for applications in precision spraying of pesticides, dermatological treatment, fragrances, functional graphics, and coatings.

AUTHOR INFORMATION

Corresponding Authors

*E-mail: c.d.bain@durham.ac.uk; rhd.deng@gmail.com

Notes

The authors declare no competing financial interest.

ACKNOWLEDGMENT

The authors are grateful to M. Possiwan and A. Piñeiro Romero for Raman imaging and Dr. R. Pal for fluorescence microscopy imaging. The code to analyse Raman images was written by M. Possiwan and Dr. L. Yang. This work was funded by the EPSRC under Grant EP/N025245/1. YW thanks Durham University and the China Scholarship Council for studentship funding.

REFERENCES

1. White, S. R.; Sottos, N. R.; Geubelle, P. H.; Moore, J. S.; Kessler, M. R.; Sriram, S. R.; Brown, E. N.; Viswanathan, S., Autonomic healing of polymer composites. Nature **2001,** 409, 794.

2. Zhao, Y.; Fickert, J.; Landfester, K.; Crespy, D., Encapsulation of self-healing agents in polymer nanocapsules. Small **2012,** 8 (19), 2954-8.

3. Kim, S.-R.; Getachew, B. A.; Park, S.-J.; Kwon, O.-S.; Ryu, W.-H.; Taylor, A. D.; Bae, J.; Kim, J.-H., Toward Microcapsule-Embedded Self-Healing Membranes. Environmental Science & Technology Letters **2016,** 3 (5), 216-221.

4. Geng, J.; Li, W.; Smaga, L. P.; Sottos, N. R.; Chan, J., Damage-Responsive Microcapsules for Amplified Photoacoustic Detection of Microcracks in Polymers. Chem. Mater. **2018,** 30 (7), 2198-2202.

5. Li, W.; Matthews, C. C.; Yang, K.; Odarczenko, M. T.; White, S. R.; Sottos, N. R., Autonomous Indication of Mechanical Damage in Polymeric Coatings. Adv Mater **2016,** 28 (11), 2189-94.

6. Yoo, Y.; Martinez, C.; Youngblood, J. P., Synthesis and Characterization of Microencapsulated Phase Change Materials with Poly(urea-urethane) Shells Containing Cellulose Nanocrystals. ACS Appl Mater Interfaces **2017,** 9 (37), 31763-31776.

7. Xu, J.; Li, J.; Yang, Y.; Wang, K.; Xu, N.; Li, J.; Liang, R.; Shen, L.; Xie, X.; Tao, J.; Zhu, J., Block Copolymer Capsules with Structure-Dependent Release Behavior. Angewandte Chemie **2016,** 55 (47), 14633-14637.

8. Liu, J. W.; Zhang, Y.; Wang, C. Y.; Xu, R. Z.; Chen, Z. P.; Gu, N., Magnetically Sensitive Alginate-Templated Polyelectrolyte Multilayer Microcapsules for Controlled Release of Doxorubicin. J Phys Chem C **2010,** 114 (17), 7673-7679.

9. Xia, Y.; Wu, J.; Du, Y.; Miao, C.; Su, Z.; Ma, G., Bridging Systemic Immunity with Gastrointestinal Immune Responses via Oil-in-Polymer Capsules. Adv Mater **2018**, e1801067.

10. Fenton, O. S.; Olafson, K. N.; Pillai, P. S.; Mitchell, M. J.; Langer, R., Advances in Biomaterials for Drug Delivery. Adv Mater **2018**, e1705328.

11. Zhang, L.; Cai, L. H.; Lienemann, P. S.; Rossow, T.; Polenz, I.; Vallmajo-Martin, Q.; Ehrbar, M.; Na, H.; Mooney, D. J.; Weitz, D. A., One-Step Microfluidic Fabrication of Polyelectrolyte Microcapsules in Aqueous Conditions for Protein Release. Angewandte Chemie **2016,** 55 (43), 13470-13474.

12. Ravanfar, R.; Celli, G. B.; Abbaspourrad, A., Controlling the Release from Enzyme-Responsive Microcapsules with a Smart Natural Shell. ACS Appl Mater Interfaces **2018,** 10 (6), 6046-6053.

13. Pekarek, K. J.; Jacob, J. S.; Mathiowitz, E., Double-walled polymer microspheres for controlled drug release. Nature **1994,** 367 (6460), 258-60.

14. ten Cate, A. T.; Gaspar, C. H.; Virtanen, H. L. K.; Stevens, R. S. A.; Koldeweij, R. B. J.; Olkkonen, J. T.; Rentrop, C. H. A.; Smolander, M. H., Printed electronic switch on flexible substrates using printed microcapsules. J. Mater. Sci. **2014,** 49 (17), 5831-5837.

15. Rengarajan, G. T.; Walder, L.; Gorb, S. N.; Steinhart, M., High-throughput generation of micropatterns of dye-containing capsules embedded in transparent elastomeric monoliths by inkjet printing. ACS Appl Mater Interfaces **2012,** 4 (3), 1169-73.

16. Kim, M.; Park, K. J.; Seok, S.; Ok, J. M.; Jung, H. T.; Choe, J.; Kim, D. H., Fabrication of Microcapsules for Dye-Doped Polymer-Dispersed Liquid Crystal-Based Smart Windows. ACS Appl Mater Interfaces **2015,** 7 (32), 17904-9.

17. Guldin, S.; Kohn, P.; Stefik, M.; Song, J.; Divitini, G.; Ecarla, F.; Ducati, C.; Wiesner, U.; Steiner, U., Self-cleaning antireflective optical coatings. Nano letters **2013,** 13 (11), 5329-35.

18. Savolainen, A.; Zhang, Y.; Rochefort, D.; Holopainen, U.; Erho, T.; Virtanen, J.; Smolander, M., Printing of polymer microcapsules for enzyme immobilization on paper substrate. Biomacromolecules **2011,** 12 (6), 2008-15.

19. Lee, H.; Choi, C. H.; Abbaspourrad, A.; Wesner, C.; Caggioni, M.; Zhu, T.; Weitz, D. A., Encapsulation and Enhanced Retention of Fragrance in Polymer Microcapsules. ACS Appl Mater Interfaces **2016,** 8 (6), 4007-13.

20. Amstad, E., Capsules: Their Past and Opportunities for Their Future. ACS Macro Letters **2017,** 6 (8), 841-847.

21. Abbaspourrad, A.; Carroll, N. J.; Kim, S. H.; Weitz, D. A., Polymer microcapsules with programmable active release. J. Am. Chem. Soc. **2013,** 135 (20), 7744-50.

22. Tang, S.; Tang, L.; Lu, X.; Liu, H.; Moore, J. S., Programmable Payload Release from Transient Polymer Microcapsules Triggered by a Specific Ion Coactivation Effect. J. Am. Chem. Soc. **2018,** 140 (1), 94-97.

23. Gun, W. J.; Routh, A. F., Formation and characterization of pH-responsive liquid core microcapsules. Langmuir **2013,** 29 (40), 12541-8.

24. DiLauro, A. M.; Abbaspourrad, A.; Weitz, D. A.; Phillips, S. T., Stimuli-Responsive Core–Shell Microcapsules with Tunable Rates of Release by Using a Depolymerizable Poly(phthalaldehyde) Membrane. Macromolecules **2013,** 46 (9), 3309-3313.

25. Deng, R.; Derry, M. J.; Mable, C. J.; Ning, Y.; Armes, S. P., Using Dynamic Covalent Chemistry To Drive Morphological Transitions: Controlled Release of Encapsulated Nanoparticles from Block Copolymer Vesicles. J. Am. Chem. Soc. **2017,** 139 (22), 7616-7623.

26. Dowding, P. J.; Atkin, R.; Vincent, B.; Bouillot, P., Oil core/polymer shell microcapsules by internal phase separation from emulsion droplets. II: controlling the release profile of active molecules. Langmuir **2005,** 21 (12), 5278-84.

27. Wu, M.; Zhu, Y.; Jiang, W., Release Behavior of Polymeric Vesicles in Solution Controlled by External Electrostatic Field. ACS Macro Letters **2016,** 5 (11), 1212-1216.

28. Park, C. H.; Lee, S.; Pornnoppadol, G.; Nam, Y. S.; Kim, S.-H.; Kim, B. J., Microcapsules Containing pH-Responsive, Fluorescent Polymer-Integrated MoS2: An Effective Platform for in Situ pH Sensing and Photothermal Heating. ACS Applied Materials & Interfaces **2018,** 10 (10), 9023-9031.

29. Cui, J.; van Koeverden, M. P.; Mullner, M.; Kempe, K.; Caruso, F., Emerging methods for the fabrication of polymer capsules. Advances in colloid and interface science **2014,** 207, 14-31.

30. Yow, H. N.; Routh, A. F., Formation of liquid core–polymer shell microcapsules. Soft Matter **2006,** 2 (11), 940-949.

31. Bouchemal, K.; Briançon, S.; Perrier, E.; Fessi, H.; Bonnet, I.; Zydowicz, N., Synthesis and characterization of polyurethane and poly(ether urethane) nanocapsules using a new technique of interfacial polycondensation combined to spontaneous emulsification. International Journal of Pharmaceutics **2004,** 269 (1), 89-100.

32. van Zyl, A. J. P.; Sanderson, R. D.; de Wet-Roos, D.; Klumperman, B., Core/shell particles containing liquid cores: Morphology prediction, synthesis, and characterization. Macromolecules **2003,** 36 (23), 8621-8629.

33. Atkin, R.; Davies, P.; Hardy, J.; Vincent, B., Preparation of aqueous core/polymer shell microcapsules by internal phase separation. Macromolecules **2004,** 37 (21), 7979-7985.

34. Yu, X.; Zhao, Z.; Nie, W.; Deng, R.; Liu, S.; Liang, R.; Zhu, J.; Ji, X., Biodegradable polymer microcapsules fabrication through a template-free approach. Langmuir **2011,** 27 (16), 10265-73.

35. Loxley, A.; Vincent, B., Preparation of Poly(methylmethacrylate) Microcapsules with Liquid Cores. J Colloid Interface Sci **1998,** 208 (1), 49-62.

36. Deng, R.; Yang, L.; Bain, C. D., Combining Inkjet Printing with Emulsion Solvent Evaporation to Pattern Polymeric Particles. ACS Appl Mater Interfaces **2018,** 10 (15), 12317-12322.

37. Wang, Y.; Deng, R.; Yang, L.; Bain, C., Fabrication of Monolayers of Uniform Polymeric Particles by Inkjet Printing of Monodisperse Emulsions Produced by Microfluidics. Submitted.

38. Pal, R., Phase modulation nanoscopy: a simple approach to enhanced optical resolution. Faraday Discussions **2015,** 177 (0), 507-515.

39. Brandrup, J., Immergut, E. H., Grulke, E. A., Eds.; , Polymer Handbook; Wiley: New York, 1999; Section VII, pp 675-714.

40. Johns, A. S.; Bain, C. D., Ink-Jet Printing of High-Molecular-Weight Polymers in Oil-in-Water Emulsions. ACS Applied Materials & Interfaces **2017,** 9 (27), 22918-22926.

41. Agrawal, A.; Saran, A. D.; Rath, S. S.; Khanna, A., Constrained nonlinear optimization for solubility parameters of poly(lactic acid) and poly(glycolic acid)—validation and comparison. Polymer **2004,** 45 (25), 8603-8612.

42. Dowding, P. J.; Atkin, R.; Vincent, B.; Bouillot, P., Oil core-polymer shell microcapsules prepared by internal phase separation from emulsion droplets. I. Characterization and release rates for microcapsules with polystyrene shells. Langmuir **2004,** 20 (26), 11374-9.

43. Liu, S.; Cai, M.; Deng, R.; Wang, J.; Liang, R.; Zhu, J., Fabrication of porous polymer microparticles with tunable pore size and density through the combination of phase separation and emulsion-solvent evaporation approach. Korea-Australia Rheology Journal **2014,** 26 (1), 63-71.

44. Brochard-Wyart, F.; Di Meglio, J. M.; Quere, D.; De Gennes, P. G., Spreading of nonvolatile liquids in a continuum picture. Langmuir **1991,** 7 (2), 335-338.

45. Krevelen, D. W. v., Properties of Polymers: Their Estimation and Correlation with Chemical Structure. 2nd ed.; Elsevier: NewYork, 1976.

46. Shin, J. M.; Kim, M. P.; Yang, H.; Ku, K. H.; Jang, S. G.; Youm, K. H.; Yi, G.-R.; Kim, B. J., Monodipserse Nanostructured Spheres of Block Copolymers and Nanoparticles via Cross-Flow Membrane Emulsification. Chem. Mater. **2015,** 27 (18), 6314-6321.

Table of Contents

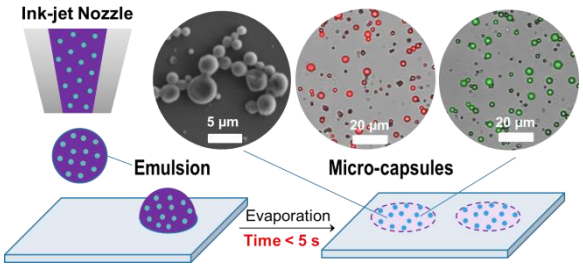

8.2 Matlab program

In this thesis, Individual polymer particles were detected in the SEM images using the built-in Matlab function for the circle Hough transform, from which I calculated the size distribution and the coefficient of variation CV.

8.2.1 Code for “Get Resolution From A Scalebar”

```
clear;

%% Image infor

folder='H:\M-Matlab codes\ParticleRegonization';

filetitle='Yilin2';

fileformat ='tif';

oldFolder=cd(folder);

scalebarLength=30; % give the known length of scale bar, micro

%% read the image

filename = [filetitle,'.',fileformat];

I=imread(filename);

I=I(:,:,1);


 %% Get Resolution

cla;

figure(1);

imshow (I);

hold on;


text(1,20,'Select two end points of scalebar','color','yellow','Fontsize',10);
```

```
selection=ginput(2);

leftx_min=floor(selection(1,1));

lefty_min=floor(selection(1,2));

rightx_max=floor(selection(2,1));

righty_max=floor(selection(2,2));


barPixel=rightx_max-leftx_min;

Resolution=scalebarLength/barPixel;

close all;

Resolution

%%

Resolution

%%

cd (oldFolder);
```

8.2.2 Code for “Particle Regonization”

```
%%%%%%%%%%%%%%%%%%%%%%%%%%%%%%%%%%%%


%%    Provide video/frame-series information here

% initiating parameters and variables
```

```
clear all;

%folder='H:\A-Project\A-Experiments\JingEXP\20170609-Et0.5-Si0.5Per-PS0.01Per@@\VideoFrames_II-4-side-withBg';

folder='H:\M-Matlab codes\ParticleRegonization';

% provide your images name (the part before numbers) and format

filetitle='Yilin2';

fileformat ='tif';

Resolution=0.0661; % pixel/um

filename = strcat(filetitle,'.',fileformat);

oldFolder=cd(folder);


%% Crop image to leave ROI


        I=imread(filename);

        I=I(:,:,1);

        cla;

        figure(1);

        imagesc(I);

        size_I=size(I);

        colormap gray;

        axis equal;

        axis([0 size_I(2) 0 size_I(1)]);
```

```
 xlabel('x /pixel');

 ylabel('y /pixel');


hold on;


text(1,20,'ROI select: top-left and bottom-right','color','yellow','Fontsize',10);

selection=ginput(2);

leftx_min=floor(selection(1,1));

lefty_min=floor(selection(1,2));

rightx_max=floor(selection(2,1));

righty_max=floor(selection(2,2));


corner=[leftx_min lefty_min; rightx_max lefty_min; rightx_max righty_max;...

leftx_min righty_max; leftx_min lefty_min];

line(corner(:,1),corner(:,2),'Color','y');


I=I(lefty_min:righty_max,leftx_min:rightx_max); %%% cropping the image

size_I=size(I); % size of the primary ROI


imagesc(I);


%% find circular objects

% Adjust the EdgeThreshold value when needed
```

```
cla;

figure (2)

imshow (I);

[centers, radii, metric] = imfindcircles(I,[10 20],'EdgeThreshold',0.1,'Method','TwoStage' );

viscircles(centers, radii,'Color','b', 'linewidth',1);


fig = gcf;

fig.Color = 'white'; % set the background figure color

fig.InvertHardcopy = 'off';

iptsetpref('ImshowBorder','tight'); % Figures without any borders


print(fig,'_particleRegonised','-dtiff','-r100','-r0' );

   %% Output diamters

   Diameter=2*radii*Resolution;

   MeanD=mean(Diameter);

   [N,column]=size(Diameter);

   Sum2=sum((Diameter-MeanD).^2);

   CoeffVari=sqrt(Sum2/(N-1));

   fileSavename = ['_Diamter','.','csv'];

   csvwrite(fileSavename,Diameter);

   CoeffVari

%%
```

8.3 Video links for emulsion droplets drying process

https://pubs.rsc.org/en/content/articlelanding/2019/lc/c9lc00588a/unauth